

Three-dimensional optical metamaterials

Von der Fakultät für Mathematik und Physik der Universität Stuttgart
zur Erlangung der Würde eines Doktors
der Naturwissenschaften (Dr. rer. nat.) genehmigte Abhandlung

vorgelegt von

Na Liu

aus Liaoning, V. R. China

Hauptberichter: Prof. Dr. Harald Giessen

Mitberichter: Prof. Dr. Martin Dressel

Tag der mündlichen Prüfung: 27. July 2009

4. Physikalisches Institut der Universität Stuttgart

2009

Zusammenfassung

Metamaterialien haben aufgrund ihrer faszinierenden Eigenschaften viel Aufsehen erregt. Es wurden zahlreiche optische Anwendungen vorgeschlagen, wie zum Beispiel Materialien mit negativem Brechungsindex, Perfekte Linsen und Tarnkappen. Um reale Metamaterialien herzustellen, braucht man dreidimensionale Strukturen. Es ist eine anspruchsvolle Aufgabe, diese Strukturen herzustellen und ihre optischen Eigenschaften, im Besonderen die Kopplungsmechanismen zwischen benachbarten Strukturen und Ebenen zu verstehen. In dieser Arbeit, stellen wir die Vorteile und Probleme vor, die mit verschiedenen Herstellungsmethoden einhergehen. Wir diskutieren die Kopplung zwischen einzelnen Elementen und berücksichtigen elektrische und magnetische Dipole sowie höhere Ordnungen der Multipolentwicklung. Es werden longitudinale und transversale Wechselwirkungen sowie deren Zusammenspiel untersucht.

Abstract

Metamaterials have attracted a lot of attention due to their fascinating properties. Many practical applications have been suggested such as negative refraction, perfect lens, and invisibility cloak. In order to create real materials, we need three-dimensional structures. These structures pose some challenges in fabrication as well as with regards to understanding their optical properties, especially the relevant coupling mechanisms between neighboring elements and layers. In this thesis, we are going to present the advantages and problems associated with different fabrication methods. We will discuss coupling between the elements, taking electric and magnetic dipoles as well as higher order multipoles into account. Longitudinal and transverse interactions as well as their interplay will be examined.

Publications

Parts of this thesis have been published in scientific journals:

- N. Liu, T. Weiss, M. Mesch, L. Langguth, U. Eigenthaler, M. Hirschner, C. Sönnichsen, and H. Giessen, *Planar metamaterial analog of electromagnetically induced transparency for plasmonic sensing*, submitted to Nano Letters (2009).
- N. Liu and H. Giessen, *Three-dimensional optical metamaterials*, invited paper, *Angewandte Chemie International Edition*, in preparation (2009).
- N. Liu, L. Langguth, T. Weiss, J. Kästel, M. Fleischhauer, T. Pfau, and H. Giessen, *Plasmonic electromagnetically induced transparency in metamaterials*, Nature Materials, in press, doi:10.1038/nmat2495 (2009).
- N. Liu, H. Liu, S. Zhu, and H. Giessen, *Stereometamaterials*, Nature Photonics **3**, 157 (2009).
- N. Liu and H. Giessen, *Three-dimensional optical metamaterials as model systems for longitudinal and transverse magnetic coupling*, Optics Express **16**, 21233 (2008).
- N. Liu, S. Kaiser, and H. Giessen, *Magnetoinductive and Electroinductive Coupling in Plasmonic Metamaterial Molecules*, Advanced Materials **20**, 4521 (2008).
- N. Liu, L. Fu, S. Kaiser, H. Schweizer, and H. Giessen, *Plasmonic building blocks for magnetic molecules in three-dimensional metamaterials*, Advanced Materials **20**, 3859 (2008).
- N. Liu, H. Guo, L. Fu, S. Kaiser, H. Schweizer, and H. Giessen, *Three-dimensional photonic metamaterials at optical frequencies*, Nature Materials **7**, 31 (2008).
- N. Liu, H. Guo, L. Fu, H. Schweizer, S. Kaiser, and H. Giessen, *Plasmon hybridization in stacked cut-wire metamaterials*, Advanced Materials **19**, 3628 (2007).

- N. Liu, H. Guo, L. Fu, H. Schweizer, S. Kaiser, and Harald Giessen, *Electromagnetic resonances in single and double split-ring resonator metamaterials in the near infrared*, Phys. stat. sol. (b) **244**, 1251 (2007).

Additional scientific publications which are not presented in this thesis:

- H. Guo, T.P. Meyrath, T. Zentgraf, N. Liu, L. Fu, H. Schweizer, and H. Giessen, *Optical resonances of bowtie slot antennas and their geometry and material dependence*, Opt. Express **16**, 7756-7766 (2008).
- L. Fu, H. Schweizer, H. Guo, N. Liu, and H. Giessen, *Synthesis of transmission line models for metamaterial slabs at optical frequencies*, Phys. Rev. B **78**, 115110 (2008).
- H. Guo, N. Liu, L. Fu, T. P. Meyrath, T. Zentgraf, H. Schweizer, and H. Giessen, *Resonance hybridization in double split-ring resonator metamaterials*, Opt. Express **15**, 12095 (2007).
- H. Schweizer, L. Fu, H. Gräbeldinger, H. Guo, N. Liu, S. Kaiser, and H. Giessen, *Negative permeability around 630 nm in nanofabricated meander metamaterials*, Phys. stat. sol. (a) **204**, 3886 (2007).
- H. Schweizer, L. Fu, H. Gräbeldinger, H. Guo, N. Liu, S. Kaiser, and H. Giessen, *Longitudinal Capacitance Design for Optical Left-Handed Metamaterials*, Phys. stat. sol. (b) **244**, 1243 (2007).
- H. Guo, N. Liu, L. Fu, H. Schweizer, S. Kaiser, and H. Giessen, *Thickness dependence of the optical properties of split-ring resonator metamaterials*, Phys. stat. sol. (b) **244**, 1256 (2007).
- L. Fu, H. Schweizer, H. Guo, N. Liu, and H. Giessen, *Analysis of Metamaterials using Transmission Line Models*, Appl. Phys. B **86**, 425 (2007).
- C. Rockstuhl, T. Zentgraf, H. Guo, N. Liu, C. Etrich, I. Loa, K. Syassen, J. Kuhl, F. Lederer, and H. Giessen, *Resonances of split-ring resonator metamaterials in the near infrared*, Appl. Phys. B **84**, 219 (2006).

At international conferences (only own presentations):

- N. Liu and H. Giessen, *Plasmonic analog of EIT and metamaterial sensors*, Invited talk, SPIE 2009 Optics and Photonics Meeting, Metallic Nanostructures and Their Optical Properties VII, San Diego, USA (2009)
- N. Liu and H. Giessen, *3D metamaterials: coupling matters!*, Invited talk, 5th Workshop on Numerical Methods for Optical Nano Structures, ETH Zurich, CH (2009).
- N. Liu, L. Langguth, T. Weiss, J. Kästel, M. Fleischhauer, T. Pfau, and H. Giessen, *Plasmonic electromagnetically induced transparency in metamaterials*, Talk, 3rd International Congress on Advanced Electromagnetic Materials in Microwaves and Optics, London, UK (2009).
- N. Liu and H. Giessen, *Stereometamaterials*, Poster, Surface Plasmon Photonics 4, Amsterdam, The Netherlands (2009).
- N. Liu and H. Giessen, *Three-dimensional optical metamaterials as model systems for longitudinal and transverse magnetic coupling*, Invited talk, MORIS, Awaji-island, Hyogo, Japan (2009).
- N. Liu, H. Liu, S. Zhu, and H. Giessen, *Stereometamaterials*, Talk, CLEO/QELS Baltimore, USA (2009).
- N. Liu, H. Liu, S. Zhu, and H. Giessen, *Plasmonic electromagnetically induced transparency in metamaterials*, Postdeadline talk, CLEO/QELS Baltimore, USA (2009).
- N. Liu, H. Liu, S. Zhu, and H. Giessen, *Stereometamaterials*, Talk, PECS VIII, Sydney, Australia (2009).
- N. Liu, H. Liu, S. Zhu, and H. Giessen, *Stereometamaterials*, Talk, Hongkong University of Science and Technology, Department of Physics (2009).
- N. Liu and H. Giessen, *Three-dimensional optical metamaterials*, Invited talk, IFW, University of Dresden, Germany (2009)
- N. Liu, H. Liu, S. Zhu, and H. Giessen, *Stereometamaterials*, Talk, Nanometa, Seefeld, Austria (2009).

- N. Liu and H. Giessen, *Stereometamaterials*, Poster, 2nd SSLS Workshop, National University at Singapore (2008).
- N. Liu and H. Giessen, *Stereometamaterials*, Invited talk, Nanjing University, Nanjing, China (2008).
- N. Liu and H. Giessen, *Stereometamaterials*, Talk, Dept. of Electrical Engineering, University of Pennsylvania, Philadelphia, USA (2008).
- N. Liu, H. Liu, S. Zhu, and H. Giessen, *Stereometamaterials*, Postdeadline talk, OSA Annual meeting, Rochester, NY, USA (2008).
- N. Liu, S. Kaiser, and H. Giessen, *Magnetoinductive and Electroinductive Coupling in Plasmonic Metamaterial Molecules*, Talk, 2nd International Congress on Advanced Electromagnetic Materials in Microwaves and Optics, Pamplona, Spain (2008).
- N. Liu and H. Giessen, *Electromagnetically induced transparency in Optical Metamaterials*, Postdeadline Talk, CLEO/QELS San Jose, USA (2008).
- N. Liu and H. Giessen, *Three-dimensional optical metamaterials*. Invited talk, CLEO/QELS San Jose, USA (2008).
- N. Liu and H. Giessen, *Three-dimensional optical metamaterials*. Talk, SPIE, Strasbourg, France (2008).
- N. Liu and H. Giessen, *Three-dimensional optical metamaterials*. Talk, PIERS, Hangzhou, China (2008).
- N. Liu, H. Guo, L. Fu, S. Kaiser, H. Schweizer, and H. Giessen, *Three-dimensional photonic metamaterials at optical frequencies*, Talk, 1st International Congress on Advanced Electromagnetic Materials in Microwaves and Optics, Rome, Italy (2007).
- N. Liu, H. Guo, L. Fu, H. Schweizer, S. Kaiser, and H. Giessen, *Plasmon hybridization in stacked cut-wire metamaterials*, Poster, Nanometa, Seefeld, Austria (2007).

Contents

Zusammenfassung	i
Abstract	ii
Publications	v
Contents	ix
1. Introduction	1
2. Theoretical background	5
2.1 Electrostatic dipole-dipole interaction	5
2.1.1 Multipole expansion	5
2.1.2 The electric field of a dipole.....	7
2.1.3 The energy of a charge distribution in an external field	8
2.2 Electric dipole radiation	9
2.2.1 Fields of a localized oscillating source.....	9
2.2.2 Radiation of an electric dipole	11
2.3 Lagrangian formalism	12
2.4 Plasmon hybridization	13
3. Fabrication, characterization, and simulation	17
3.1 Structure fabrication	17
3.1.1 Planar fabrication	17
3.1.2 Three-dimensional fabrication	18
3.2 Optical characterization	19
3.3 Numerical simulation	20
4. Plasmon hybridization in three-dimensional optical metamaterials	23
4.1 Electric plasmon hybridization in stacked cut-wire metamaterials.....	23
4.1.1 Introduction	23
4.1.2 Experimental results	23
4.1.3 Summary	29

4.2 Magnetic plasmon hybridization in stacked fishnet metamaterials.....	29
4.2.1 Introduction	29
4.2.2 Experimental results	30
4.2.3 Summary	39
5. Coupling effects in split-ring resonator metamaterials	41
5.1 Planar split-ring resonators.....	41
5.1.1 Introduction	41
5.1.2 Experimental results	41
5.1.3 Summary	49
5.2 Three-dimensional split-ring resonators.....	49
5.2.1 Introduction	49
5.2.2 Experimental results	50
5.2.3 Summary	59
5.3 Optical magnetism	59
5.3.1 Introduction	59
5.3.2 Design and characterization of metamaterial structures.....	60
5.3.3 Summary	64
6. Novel three-dimensional metamaterials	67
6.1 Stereometamaterials	67
6.1.1 Introduction	67
6.1.2 Experimental results	67
6.1.3 Summary	77
6.2 Plasmon electromagnetically induced transparency in metamaterials.....	77
6.2.1 Introduction	77
6.2.2 Experimental results	79
6.2.3 Summary	86
7. Conclusions	87
Bibliography	89
Acknowledgements	93
Resume	95

1. Introduction

Metamaterials have gained a lot of attention due to their novel electromagnetic properties [1-4]. They consist of artificial structures which are much smaller than the operating wavelength of light. Their main potential is in the area of tailoring permittivity, permeability, and the refractive index of materials [1-4]. A medium with simultaneous negative permittivity and negative permeability can exhibit negative refraction and unique reversed electromagnetic properties, as discussed by Veselago [5] long before such materials were fabricated. A negative refractive index material, which does not exist in nature, can be realized by a specifically designed metamaterial when its negative permeability and negative permittivity are tuned to the same frequency band. In the GHz frequency range, negative permeability was achieved using split-ring resonators (SRRs) [6]. In combination with thin continuous wires, which are responsible for negative permittivity [7], a negative refractive index material was first demonstrated by Smith *et al.* in 2000 [8]. Because metamaterial building block dimensions in the GHz frequency range are on the order of millimeters, it is easy to stack them together to three-dimensional (3D) electromagnetic elements for practical applications such as perfect lenses [9, 10] and cloaking devices [11, 12]. In the optical regime, the most common designs for metamaterials include SRRs, cut-wires, and fishnets [3, 13-16]. These structures are entirely based on two-dimensional (2D) systems, which cannot be used as bulk optical elements.

Stacking of 2D metamaterials is assumed to be the pathway towards the third dimension in the optical regime. Nevertheless, stacking of metamaterials in general confronts a fundamental problem: vertical electromagnetic coupling of neighboring metamaterial layers. Subsequently, coupling effects in stacked metamaterials open up an avenue to intriguing physical and optical phenomena. Therefore, a comprehensive understanding of the different coupling mechanisms is essential for unravelling the optical properties of metamaterials. In this thesis, we present a detailed study on the coupling effects in stacked metamaterials in the

optical frequency regime. In Chapter 2, we show the basic mathematics for dipole-dipole interactions both in the electrostatic regime and the far field regime. We also show a simple and intuitive method, namely, plasmon hybridization for understanding the optical properties of coupled plasmonic nanostructures. In Chapter 3, we present a general recipe to manufacture 3D optical metamaterials using a layer-by-layer technique [17-19]. Specifically, we introduce a fabrication process by means of planarization, lateral alignment, and stacking. We also present the simulation techniques, which were used to predict the resonant behavior of our metamaterial structures.

After the experimental methods and simulation techniques, in Chapter 4 we investigate the electric and magnetic plasmon hybridizations in stacked metamaterials [20, 21]. We demonstrate theoretically and experimentally the formation of artificial ‘molecules’ from coupled ‘electric or magnetic atoms’ in stacked cut-wire and fishnet metamaterials, respectively. We develop the concept of ‘electric molecules’ as well as ‘magnetic molecules’, generalizing the plasmon hybridization scheme to N artificial ‘atoms’ that form an ‘electric or magnetic solid’. We explain the complex optical spectra as well as selection rules and introduce a new model to classify their symmetries.

In Chapter 5, different coupling games in SRR metamaterials are demonstrated. We first introduce the lateral inductive coupling mechanism [22] in planar rotated SRR dimers. The key for this scheme is to use structural asymmetry in SRR dimers so that phase retardation can be introduced between two constituent SRRs with convenient normal light incidence. Subsequently, the vertical coupling effect in stacked multilayer SRR metamaterials is demonstrated. We investigate the interaction between adjacent stacked layers, and analyze the optical properties of stacked metamaterials with respect to an increasing number of layers. Next we demonstrate that metamaterials represent model systems for longitudinal and transverse magnetic coupling in the optical domain. In particular, such coupling can lead to fully parallel or antiparallel alignment of the magnetic dipoles at the lowest frequency resonance. Also, we present the design scheme for constructing 3D metamaterials with solely magnetic interaction.

In Chapter 6, we introduce two novel designs for stacked metamaterials, which might be suitable for practical applications in the future. We study a set of stereometamaterials and

demonstrate that the optical properties of stereo-SRR dimers can be substantially modified by altering the twist angles between two SRR ‘atoms’, arising from the variation of electric and magnetic interactions between them. Furthermore, we show that the inclusion of the higher-order electric multipolar interactions is essential to understand the physical implications of the twisting dispersion. A theoretical model based on a Lagrangian formalism is utilized to interpret the evolution of the coupling effects in dependence of twist angles. Finally, we provide the first experimental demonstration of plasmonic electromagnetically induced transparency (EIT) [23] in optical metamaterials. We experimentally show that the EIT-like spectra can be modified by varying the coupling strength between a dipole and a quadrupole antenna via accurate structural tuning. The agreement between experiment and a simple EIT model is nearly perfect. Moreover, we demonstrate that our experimental transmittance linewidth is only limited by Drude damping. The resulting narrow, yet fully modulated EIT-like features, render our nanoplasmonic system ideal for slow light and novel sensors with high sensitivity.

2. Theoretical background

2.1 Electrostatic dipole-dipole interaction

We are going to deal in this Chapter with different arrangements of metallic nanostructures that interact. As a first approximation, one can assume simple static charge distributions that interact with each other. The basic theory derived in this Chapter can be utilized to understand and calculate the interaction in coupled metamaterials. Examples include metallic cut-wires, split-ring resonators (SRRs) as well as fishnets (see Fig. 2.1).

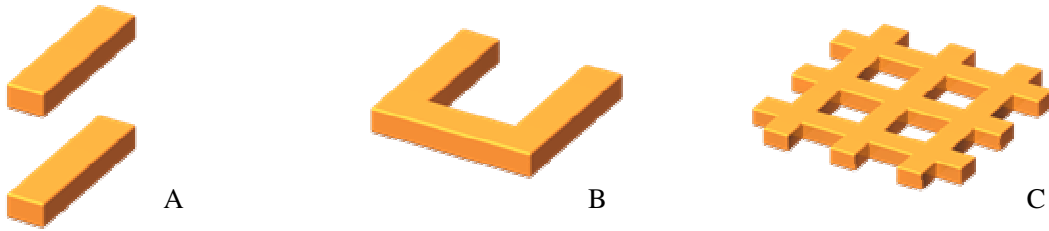


Figure 2.1: Fundamental metamaterial designs. (A) cut-wires (B) split-ring resonator (C) fishnet.

2.1.1 Multipole expansion

In order to calculate the electrostatic interaction between charges, one has to make use of the multipole expansion of the charge distribution. A localized distribution of charges is described by the charge density $\rho(\vec{x}')$, which is nonvanishing only inside a sphere of radius R around some origin [24]. The potential outside the sphere can be written as an expansion in spherical harmonics (see Fig. 2.2):

$$\Phi(\vec{x}) = \sum_{l=0}^{\infty} \sum_{m=-l}^l \frac{4\pi}{2l+1} q_{lm} \frac{Y_{lm}(\theta, \phi)}{r^{l+1}} \quad (2.1)$$

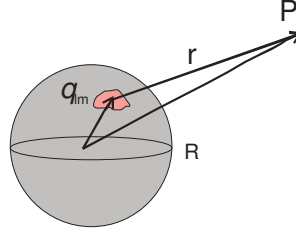


Figure 2.2: Multipole expansion of the potential.

Equation (2.1) is called a multipole expansion; the $l = 0$ term is called the monopole term, $l = 1$ is the dipole term, and so on. The problem to be solved is the determination of the constant q_{lm} in terms of the properties of the charge density $\rho(\vec{x}')$. The solution is

$$\Phi(\vec{x}) = \int \frac{\rho(\vec{x}')}{|\vec{x} - \vec{x}'|} d^3x'$$

Then we find:

$$\Phi(\vec{x}) = 4\pi \sum_{l,m} \frac{1}{2l+1} \left[\int Y_{lm}^*(\theta', \phi') r'^l \rho(\vec{x}') d^3x' \right] \frac{Y_{lm}(\theta, \phi)}{r^{l+1}} \quad (2.2)$$

Consequently the coefficients in (2.1) are

$$q_{lm} = \int Y_{lm}^*(\theta', \phi') r'^l \rho(\vec{x}') d^3x' \quad (2.3)$$

These coefficients are called multipole moments. \vec{p} is the electric dipole moment:

$$\vec{p} = \int \vec{x}' \rho(\vec{x}') d^3x' \quad (2.4)$$

and Q_{ij} is the quadrupole moment tensor:

$$Q_{ij} = \int (3x_i' x_j' - r'^2 \delta_{ij}) \rho(\vec{x}') d^3x' \quad (2.5)$$

The expansion of $\Phi(\vec{x})$ in rectangular coordinates reads:

$$\Phi(\vec{x}) = \frac{q}{r} + \frac{\vec{p} \cdot \vec{x}}{r^3} + \frac{1}{2} \sum_{i,j} Q_{ij} \frac{x_i x_j}{r^5} + \dots \quad (2.6)$$

The quadrupole moment tensor is a 3×3 matrix [25],

$$Q = \begin{pmatrix} Q_{xx} & Q_{xy} & Q_{xz} \\ Q_{yx} & Q_{yy} & Q_{yz} \\ Q_{zx} & Q_{zy} & Q_{zz} \end{pmatrix} \quad (2.7)$$

$$\begin{aligned}
Q_{xx} &= \sum_i Q_i (3x_i^2 - r_i^2) \\
Q_{yy} &= \sum_i Q_i (3y_i^2 - r_i^2) \\
Q_{zz} &= \sum_i Q_i (3z_i^2 - r_i^2) \\
\text{where} \quad Q_{xy} &= Q_{yx} = 3 \sum_i Q_i x_i y_i \\
Q_{xz} &= Q_{zx} = 3 \sum_i Q_i x_i z_i \\
Q_{yz} &= Q_{zy} = 3 \sum_i Q_i y_i z_i
\end{aligned} \tag{2.8}$$

Therefore, the quadrupole potential in equation (2.6) can be written as

$$\frac{1}{r^5} \sum_i \frac{Q_i}{2} [(3x_i^2 - r_i^2) \bar{x}\bar{x} + (3y_i^2 - r_i^2) \bar{y}\bar{y} + (3z_i^2 - r_i^2) \bar{z}\bar{z} + 2(3x_i y_i \bar{x}\bar{y} + 3x_i z_i \bar{x}\bar{z} + y_i z_i \bar{y}\bar{z})] \tag{2.9}$$

As an example, the potential for the quadrupole with charges $+Q$ and $-Q$ at horizontal distance a and vertical distance d (see Fig. 2.3) can be derived according to equation (2.9).

$$\begin{aligned}
Q_{xx} &= Q_{yy} = Q_{zz} = Q_{xz} = Q_{yz} = 0 \\
Q_{xy} &= 3adQ
\end{aligned}$$

Therefore, the quadrupole potential in Fig. 2.3 is $\Phi_{quad} = 3adQ/2R^5$.

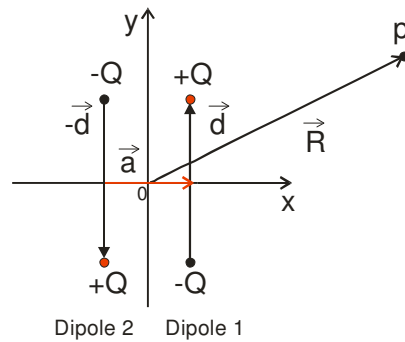


Figure 2.3: The potential of an electric quadrupole.

2.1.2 The electric field of a dipole

The electric field of a dipole can be written in vector form by taking the gradient on the dipole term in (2.6).

$$\vec{E}(\vec{x}) = -\nabla\Phi(\vec{x}) = \frac{3\vec{n}(\vec{p} \cdot \vec{n}) - \vec{p}}{|\vec{x} - \vec{x}_0|^3} \tag{2.10}$$

where \vec{n} is a unit vector directed from \vec{x}_0 to \vec{x} . As a result, the interaction energy between two dipoles \vec{p}_1 and \vec{p}_2 (see Fig. 2.4) can be obtained directly by using the dipole field (2.10). The mutual potential energy is

$$W_{12} = \frac{\vec{p}_1 \cdot \vec{p}_2 - 3(\vec{n} \cdot \vec{p}_1)(\vec{n} \cdot \vec{p}_2)}{|\vec{x}_1 - \vec{x}_2|^3} \quad (2.11)$$

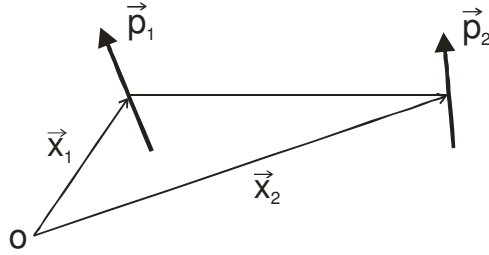


Figure 2.4: The interaction between two dipoles \vec{p}_1 and \vec{p}_2 .

Notice that the dipole field goes as the inverse cube of r . It falls off more rapidly than the monopole field which goes as the inverse square of r . Also the dipole-dipole interaction is repulsive or attractive, depending on the orientation of the dipoles. Especially, if the two dipoles are aligned side-by-side (transverse coupling), the potential energy is

$$W_T = p^2 / r^3 \quad (2.12)$$

while if the two dipoles are aligned end-to-end (longitudinal coupling), the potential energy is

$$W_L = -2 p^2 / r^3 \quad (2.13)$$

More discussions on transverse and longitudinal coupling in three-dimensional metamaterials can be found in Chapter 5.3.

2.1.3 The energy of a charge distribution in an external field

If a localized charge distribution described by $\rho(\vec{x})$ is placed in an external potential $\Phi(\vec{x})$, the electrostatic energy of the system is:

$$W = \int \rho(\vec{x})\Phi(\vec{x})d^3x \quad (2.14)$$

If the potential is slowly varying over the region where $\rho(\vec{x})$ is nonnegligible, then it can be

expanded in a Taylor series around a suitably chosen origin:

$$\Phi(\vec{x}) = \Phi(0) + \vec{x} \cdot \nabla \Phi(0) + \frac{1}{2} \sum_i \sum_j x_i x_j \frac{\partial^2 \Phi}{\partial x_i \partial x_j}(0) + \dots \quad (2.15)$$

Utilizing the definition of the electric field $\vec{E} = -\nabla \Phi$, the last two terms can be rewritten.

Then (2.15) becomes:

$$\Phi(\vec{x}) = \Phi(0) - \vec{x} \cdot \vec{E}(0) - \frac{1}{2} \sum_i \sum_j x_i x_j \frac{\partial E_j}{\partial x_i}(0) + \dots$$

Since $\nabla \cdot \vec{E} = 0$ for the external field, we can subtract $\frac{1}{6} r^2 \nabla \cdot \vec{E}(0)$ from the last term to obtain finally the expansion:

$$\Phi(\vec{x}) = \Phi(0) - \vec{x} \cdot \vec{E}(0) - \frac{1}{6} \sum_i \sum_j (3x_i x_j - r^2 \delta_{ij}) \frac{\partial E_j}{\partial x_i}(0) + \dots \quad (2.16)$$

When this is inserted into (2.14) and the definitions of total charge, dipole moment (2.4) and quadrupole moment (2.5) are employed, the energy takes the form:

$$W = q\Phi(0) - \vec{p} \cdot \vec{E}(0) - \frac{1}{6} \sum_i \sum_j Q_{ij} \frac{\partial E_j}{\partial x_i}(0) + \dots \quad (2.17)$$

The first term is the monopole term, the second is the dipole term, and the third is the quadrupole term.

2.2 Electric dipole radiation

2.2.1 Fields of a localized oscillating source

For the multipole expansion of a localized oscillating source, we can make a Fourier analysis of the time dependence and handle each Fourier component separately. Consider a localized system of charges and currents which vary sinusoidally in time:

$$\rho(\vec{x}, t) = \rho(\vec{x}) e^{-i\omega t} \quad (2.18)$$

$$\vec{J}(\vec{x}, t) = \vec{J}(\vec{x}) e^{-i\omega t} \quad (2.19)$$

the solution for the vector potential is

$$A(\vec{x}, t) = \frac{1}{c} \int d^3 x' \int dt' \frac{\vec{J}(\vec{x}', t')}{|\vec{x} - \vec{x}'|} \delta(t' + \frac{|\vec{x} - \vec{x}'|}{c} - t) \quad (2.20)$$

The Dirac delta function assures the causal behavior of the fields. With the sinusoidal time dependence (2.18 and 2.19), the solution for $A(\vec{x}, t)$ becomes

$$A(\vec{x}, t) = \frac{1}{c} \int d^3 x' \vec{J}(\vec{x}') \frac{e^{ik|\vec{x} - \vec{x}'|}}{|\vec{x} - \vec{x}'|} \quad (2.21)$$

where $k = \omega/c$ is the wave number.

For the near zone where $r \ll \lambda$ the exponential in (2.21) can be replaced by unity. The inverse distance can be expanded, leading to

$$\lim_{kr \rightarrow 0} \vec{A}(\vec{x}) = \sum_{l,m} \frac{4\pi}{2l+1} \frac{Y_{lm}(\theta, \phi)}{r^{l+1}} \int \vec{J}(\vec{x}') r'^l Y_{lm}^*(\theta', \phi') d^3 x' \quad (2.22)$$

This shows that the near fields are quasi-stationary, oscillating harmonically as $e^{-i\omega t}$, but otherwise static in character. This justifies our initial quasistatic assumption.

For the far zone ($r \gg \lambda$) the exponential in (2.21) oscillates rapidly and determines the behavior of the vector potential. In this region it is sufficient to approximate

$$|\vec{x} - \vec{x}'| \approx r - \vec{n} \cdot \vec{x}' \quad (2.23)$$

where \vec{n} is a unit vector in the direction of \vec{x} . Then the vector potential is

$$\lim_{kr \rightarrow \infty} \vec{A}(\vec{x}) = \frac{e^{ikr}}{cr} \int \vec{J}(\vec{x}') e^{-ik\vec{n} \cdot \vec{x}'} d^3 x' \quad (2.24)$$

This demonstrates that in the far zone the vector potential behaves as an outgoing spherical wave with an angular dependent coefficient. If the source dimensions are small compared to a wavelength it is appropriate to expand the integral in (2.24) in powers of k :

$$\lim_{kr \rightarrow \infty} \vec{A}(\vec{x}) = \frac{e^{ikr}}{cr} \sum_n \frac{(-ik)^n}{n!} \int \vec{J}(\vec{x}') (\vec{n} \cdot \vec{x}')^n d^3 x' \quad (2.25)$$

The magnitude of the n^{th} term is given by

$$\frac{1}{n!} \int \vec{J}(\vec{x}') (k\vec{n} \cdot \vec{x}')^n d^3 x' \quad (2.26)$$

Since the order of magnitude of \vec{x} is the source dimension d and kd is small compared to unity by assumption, the successive terms in the expansion of $\vec{A}(\vec{x})$ evidently fall off rapidly with n .

Consequently the radiation emitted from the source will come mainly from the first nonvanishing term in the expansion.

In the intermediate zone ($r \sim \lambda$) the two alternative approximations leading to (2.22) and (2.24) cannot be made; all powers of kr must be retained.

2.2.2 Radiation of an electric dipole

If only the first term in (2.25) is kept, the vector potential is

$$\vec{A}(\vec{x}) = \frac{e^{ikr}}{cr} \int \vec{J}(\vec{x}') d^3x' \quad (2.27)$$

This is the $l = 0$ part of the series and it is valid everywhere outside the source, not just in the far zone. The integral can be put in more familiar terms by an integration by parts:

$$\int \vec{J}(\vec{x}') d^3x' = -\int \vec{x}' (\vec{\nabla}' \cdot \vec{J}) d^3x' = -i\omega \int \vec{x}' \rho(\vec{x}') d^3x' \quad (2.28)$$

since from the continuity equation,

$$i\omega\rho = \vec{\nabla} \cdot \vec{J} \quad (2.29)$$

Thus the vector potential is

$$\vec{A}(\vec{x}) = -ik\vec{p} \frac{e^{ikr}}{r} \quad (2.30)$$

where $\vec{p} = \int \vec{x}' \rho(\vec{x}') d^3x'$ is the electric dipole moment.

The electric dipole fields are

$$\vec{B} = \vec{\nabla} \times \vec{A} = k^2 (\vec{n} \times \vec{p}) \frac{e^{ikr}}{r} \left(1 - \frac{1}{ikr}\right) \quad (2.31)$$

$$\vec{E} = \frac{i}{k} \vec{\nabla} \times \vec{B} = k^2 (\vec{n} \times \vec{p}) \times \vec{n} \frac{e^{ikr}}{r} + [3\vec{n}(\vec{n} \cdot \vec{p}) - \vec{p}] \left(\frac{1}{r^3} - \frac{ik}{r^2}\right) e^{ikr} \quad (2.32)$$

We note that the magnetic induction is transverse to the radius vector at all distances, but that the electric field has component parallel and perpendicular to \vec{n} .

In the near zone, the fields approaches

$$\vec{B} = ik(\vec{n} \times \vec{p}) \frac{1}{r^2} \quad (2.33)$$

$$\vec{E} = [3\vec{n}(\vec{n} \cdot \vec{p}) - \vec{p}] \frac{1}{r^3} \quad (2.34)$$

The electric field, apart from its oscillations in time, is just the static electric dipole field (2.7). The magnetic induction vanishes in the static limit $k \rightarrow 0$. Then the near zone extends to infinity.

In the radiation zone the fields take on the limiting forms,

$$\vec{B} = k^2 (\vec{n} \times \vec{p}) e^{ikr} / r \quad (2.35)$$

$$\vec{E} = \vec{B} \times \vec{n} \quad (2.36)$$

showing the typical behavior of radiation fields, namely the fields are transverse to the radius vector and fall off as r^{-1} .

2.3 Lagrangian formalism

In principle, if we knew the exact charge distributions as well as the phase retardation in metamaterials, we could calculate the dipolar and multipolar interactions directly according to the equations presented in Chapter 2.1 and 2.2. Unfortunately, the ab initio calculations are nontrivial as we would have to take the correct spatial charge and current distributions into account.

In order to understand the physics of the coupling effects in metamaterials, we simplify by introducing a Lagrangian formalism [36]. Generally, metamaterial elements such as an SRR can be modelled by an equivalent LC circuit [3] with a resonance frequency $\omega_f = 1/(LC)^{1/2}$. It consists of a magnetic coil (the metal ring) with inductance L and a capacitor (the slit of the ring) with capacitance C . If we define the total charge Q accumulated in the slit as a generalized coordinate, the Lagrangian of an SRR can be written as $\Gamma = L\dot{Q}^2/2 - Q^2/2C$. Here $L\dot{Q}^2/2$ refers to the kinetic energy of the oscillations, and $Q^2/2C$ is the electrostatic energy stored in the slit. Consequently, the Lagrangian of the coupled SRR dimer systems is a combination of two individual SRRs with the additional electric and magnetic interaction terms (we neglect losses):

$$\Gamma = \frac{L}{2}(\dot{Q}_1^2 - \omega_f^2 Q_1^2) + \frac{L}{2}(\dot{Q}_2^2 - \omega_f^2 Q_2^2) + M_H \dot{Q}_1 \dot{Q}_2 - M_E \omega_f^2 Q_1 Q_2 \cdot (\cos \varphi - \alpha \cdot (\cos \varphi)^2 + \beta \cdot (\cos \varphi)^3) \quad (2.37)$$

Here, Q_1 and Q_2 are oscillating charges in the respective SRRs, and M_H and M_E are the mutual inductances for magnetic and electric interactions, respectively. Apart from the electric dipole-dipole interaction, the contributions from the higher-order electric multipolar interactions are also included. α and β are heuristic coefficients of the quadrupolar and octupolar plamon interactions, respectively. They serve as correction terms to the electric dipolar interaction. In principle, it should be possible to calculate them from the equations given in Chapter 2.1 and 2.2 if one knows the exact charge and current distributions. Subsequently, by solving the Euler-Lagrange equations

$$\frac{d}{dt} \left(\frac{\partial \Gamma}{\partial \dot{Q}_i} \right) - \frac{\partial \Gamma}{\partial Q_i} = 0, \quad (i=1,2), \quad (2.38)$$

the eigenfrequencies of the coupled system can be obtained as

$$\omega_{\pm} = \omega_0 \cdot \sqrt{\frac{1 \mp \kappa_E \cdot (\cos \varphi - \alpha \cdot (\cos \varphi)^2 + \beta \cdot (\cos \varphi)^3)}{1 \mp \kappa_H}}, \quad (2.39)$$

where $\kappa_E = M_E / L$ and $\kappa_H = M_H / L$ are the coefficients of the overall electric and magnetic interactions, respectively. By fitting the twisting dispersion curves, the corresponding coefficients can be estimated. Detailed discussions on the utilization of the Lagrangian formalism to stereometamaterials will be presented in Chapter 6.

2.4 Plasmon hybridization

The optical properties of metallic nanostructures are determined by the collective oscillations of their conduction electrons with respect to the positive ion background, known as plasmons. It has been shown by the pioneering work of Peter Nordlander [20, 21] that the plasmons of metallic nanostructures, while described by classical electromagnetic theory, exhibit certain characteristics that are analogous to electrons in quantum systems. This is seen mostly in

complex nanostructures, where plasmons on neighboring structures interact and the plasmons hybridize just like the electron wave functions of simple atomic and molecular orbitals. This property which is termed plasmon hybridization governs the optical properties of metallic nanostructures of increasingly complex geometries, providing a powerful and general design principle that can be applied to guide the design of metallic nanostructures and to predict their resonant properties.

Schematic illustrations of the plasmon hybridization in metallic dimers are shown in Fig. 2.5. When two degenerate states interact with each other, the coupling generally leads to a lifting of the degeneracy of the bare modes and hence results in the formation of the so-called normal modes of the system. For the side-by-side configuration (transverse coupling) as shown in Fig. 2.5A, the symmetric (antisymmetric) normal mode is characterized by a parallel (antiparallel) oscillation of the interaction dipoles. The symmetric charge distributions leads to repelling forces between the charges at the ends of the wires. This gives rise to an increased restoring force of the charge oscillation for the symmetric mode, compared to a single wire. For the antisymmetric mode, the opposite charges attract each other, thus reducing the restoring force. Therefore, the arising antisymmetric mode is lowered in frequency while the resonance frequency of the symmetric mode is increased. For the end-to-end configuration (longitudinal coupling) as shown in Fig. 2.5B, due to the orientation of the two wires, the antisymmetric (symmetric) mode has a higher (lower) resonance frequency. Specifically, the frequency level splitting for the longitudinal coupling is bigger than that of the transverse coupling. This is due to the fact that the interaction index of the longitudinal coupling is two times bigger than that of the transverse coupling as discussed in 2.1.2.

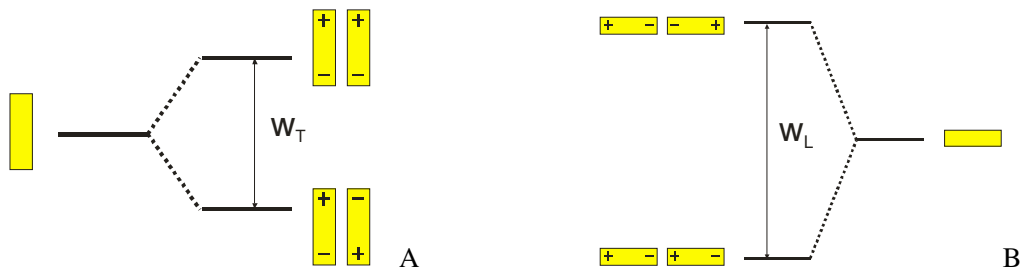


Figure 2.5: Schematic of the plasmon hybridization in two coupled metallic wires. (A) Transverse coupling. (B) Longitudinal coupling.

The concept of plasmon hybridization can be widely utilized to understand the coupling effects in metamaterials. Examples include stacked cut-wires and fishnets (see Chapter 4), planar and stacked split-ring resonators (see Chapter 5), as well as multipolar interactions in stereometamaterials and plasmonic electromagnetically induced transparency metamaterials (see Chapter 6).

3. Fabrication, characterization, and simulation

3.1 Structure fabrication

3.1.1 Planar fabrication

Electron-beam lithography is the practice of scanning a beam of electrons in a patterned fashion across a surface covered with a resist and of selectively removing either exposed or non-exposed regions of the resist. Generally, electron-beam lithography is a widely spread tool for lateral structuring below the resolution limit of standard photolithography. In order to transfer the resist pattern into a metal film, dry-etching or lift-off process is used after the electron-beam writing. Figs. 3.1 depicts the schematic diagram of the fabrication process using negative resist (AR-N). A gold film is deposited onto a glass substrate by electron-gun evaporation. In order to enhance the adhesion between the gold film and the glass substrate, a thin chromium film is first deposited. AR-N resist is spin-coated and subsequently exposed by the electron-beam. For negative resist, polymer chains cross-link together after the exposure, which renders them soluble in the developer. The exposed areas will stay on the substrate after the development. Finally, the resist mask is removed by oxygen plasma etching.

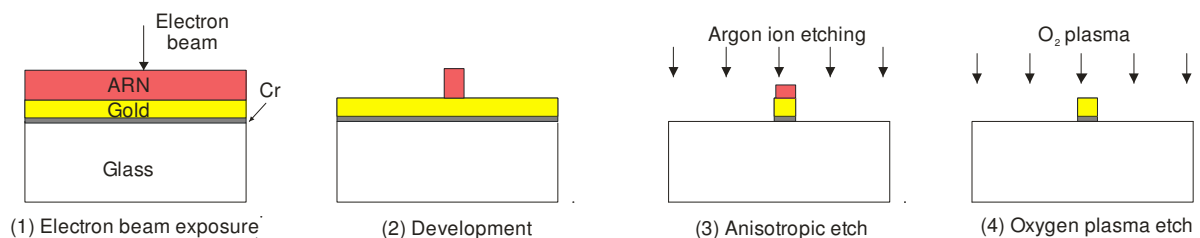


Figure 3.1: Schematic of electron-beam lithography using negative resist (AR-N). (1) Deposition of chromium and gold by electron gun evaporation. Spin-coating of AR-N resist and electron-beam exposure. (2) Resist development. (3) Argon ion-beam etching. (4) Oxygen plasma etching to remove the residual resist.

Figs. 3.2 depicts the schematic diagram of the fabrication process using positive resist (PMMA). PMMA is spin-coated on a glass substrate. A chromium layer is deposited in order to increase the conductivity of the PMMA surface. For positive resist, bonds in the long polymer chains are broken by electrons and this increases the solubility of these areas in a developer. After development, the exposed areas will be washed away in the developer. Next, chromium and gold films are evaporated on the resist pattern. Gold structures are generated by a following lift-off procedure.

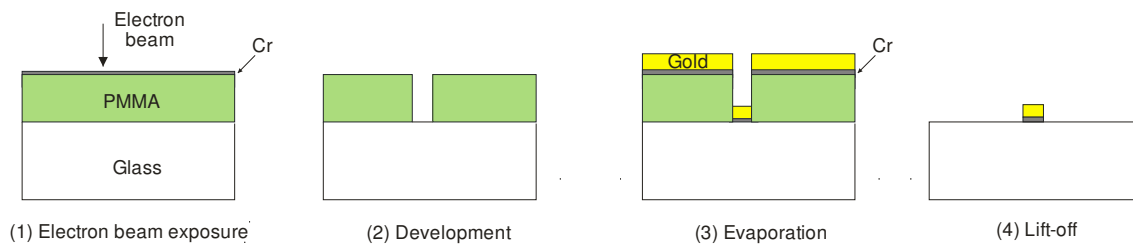


Figure 3.2: Schematic of electron-beam lithography using positive resist (PMMA). (1) Spin-coating of AR-N resist and electron-beam exposure. (2) Resist development. (3) Deposition of chromium and gold by electron gun evaporation. (4) Lift-off.

3.1.2 Three-dimensional fabrication

Figs. 3.3 depicts the schematic diagram of the fabrication process for three-dimensional structures [26]. Three (or more) gold alignment marks (size $4 \mu\text{m} \times 100 \mu\text{m}$) with a gold thickness of 250 nm are first fabricated by lift-off on a quartz substrate. The substrate is then covered with a thin gold film using electron-beam evaporation. Next, nanostructures are defined in negative resist (AR-N) by electron-beam lithography. Ion beam etching (Ar^+ ions) of the gold layer is then performed to generate the gold nanostructures. Subsequently, a spacer layer is applied on the first layer by spin-coating. A solidifiable photo polymer, PC403 (JCR, Japan) is used as the planarized spacer layer. A pre-baking process by continuously increasing the baking temperature from 90°C to 130°C is first performed to remove the solvent from the polymer. A sufficiently long bake at a higher temperature (30 min in a 180°C oven) further hardens the layer. A second gold film and a spin-coated AR-N resist layer are subsequently deposited on the sample. Next, the stacking alignment using the gold alignment marks is

applied to ensure the accurate stacking of the following structure layers. For further structure layer fabrication, the procedures of in-plane fabrication, planarization, and alignment are repeated. In order to stack a large number of layers, a renovation of the marks is appropriate. This procedure includes removing the PC403 resist on the alignment marks using oxygen plasma etching through a shadow mask, which is applied to protect the structure areas. Therefore, only the mark areas are exposed to the oxygen plasma. Another effective solution for stacking more layers is to fabricate in-plane gold marks simultaneously with each structure layer and apply them as alignment marks for the subsequent layer. This method ensures observable alignment marks during the fabrication of thicker or even bulk stacked metamaterials, since these in-plane gold marks are not exposed to multiple anisotropic etching and planarization processes.

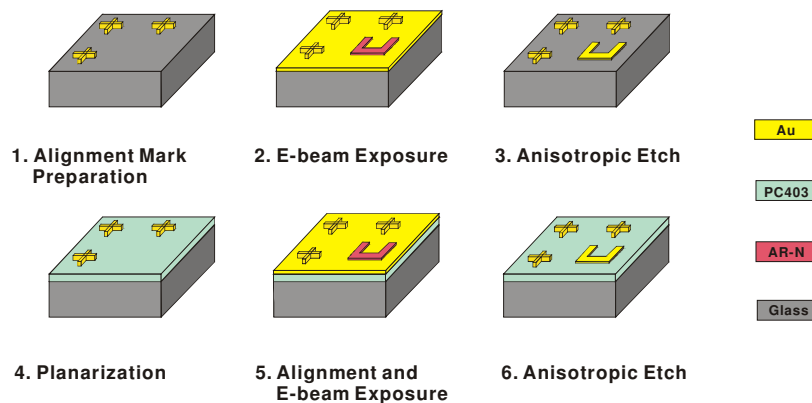


Figure 3.3: Schematic of electron-beam lithography for fabricating three-dimensional structures. (1) Alignment mark preparation by lift-off. (2) Spin-coating of AR-N resist and electron-beam exposure. (3) Argon ion-beam etching to generate gold structures. (4) Planarization by PC403. (5) Alignment and electron-beam exposure for the second layer. (6) Argon ion-beam etching to generate gold structures on the second layer.

3.2 Optical characterization

The instrument used for optical characterization has been a commercial Fourier-transformed infrared spectrometer (Bruker IFS 66v/S). This spectrometer is combined with an optical microscope ($15\times$ Cassegrain objective, numerical aperture $NA = 0.4$, liquid N_2 -cooled MCT 77K detector, infrared polarizer), which allows to measure transmittance and reflectance in very small areas. With different apertures in the light path, the diameter of this area can range

from 20 μm up to 250 μm and is chosen according to the sample size. The light source is a tungsten halogen lamp, which can be used from the visible to the near-infrared. For the shorter wavelength range (400 nm-1.2 μm) a calcium-fluoride beam splitter and a silicon diode detector are used; for the longer wavelength regime (900 nm – 5 μm) one has to switch to a calcium-fluoride beam splitter and a liquid-nitrogen-cooled mercury cadmium tellurium (MCT) detector. A thallium bromo-iodide polarizer is used to obtain linearly polarized light in both spectral regions.

3.3 Numerical simulation

In order to compare our experimental results with theoretical expectations, we have used the commercial software package CST Microwave Studio. CST Microwave Studio is a general purpose electromagnetic simulator based on Finite-Integration Technique (FIT). This numerical method provides a universal spatial discrimination scheme, applicable to various electromagnetic problems ranging from static field calculations to high frequency applications in the time or frequency domain. Different from most numerical methods, FIT discretizes the integral forms of Maxwell's equations, rather than the differential forms [27]. Maxwell's equations are numerically solved by defining a finite calculation domain, which is split up into several small grid cells by creating a suitable mesh system. Generally, the simulations are done in Cartesian grids. In order to increase the accuracy in modelling of complex boundaries, a PBA (Perfect Boundary Approximation) technique is applied to the FITD algorithm, which maintains all the advantages of structured Cartesian grids and allows an accurate modelling of curved structures. The FIT model together with the PBA theory combines the advantages of the Finite Element Method (FEM) model and the FDTD/TLM model. It offers both an excellent geometric approximation and a high simulation speed, but without the segmentation of FE models or staircase approximation of FDTD codes. Three different types of solvers are available concerning high frequency electromagnetic field problems: transient, frequency domain, and eigenmode solver.

In this work, the numerical simulations are done with transient solver, which allows for the simulation of the behavior of a structure in a wide frequency range in just a single

computational run. In order to calculate the reflectance and transmittance of metallic nanostructures with the transient solver, we apply the ‘waveguide’ boundary condition, under which the tangential component of either the E-field or the H-field are set to zero at opposite boundaries, and additionally the polarization is defined. The single element of the metallic nanostructures is placed into this rectangular waveguide. In the propagation direction the waveguide has open boundary conditions and is terminated with input and output ports. The waveguide is excited with an eigenmode at the position of one port, and the amplitude and the phase of the transmitted and reflected part of the eigenmode are calculated after propagation through the waveguide. The permittivities of the composed materials of the nanostructure and the substrate are given individually. The results are the S-parameter amplitude and phase for transmittance and reflectance. Field distributions for E and H at fixed frequencies can be recorded during the S-parameter simulation process. The simulations with the waveguide boundary condition show good agreement with the experimental measurements for periodically arranged nanostructures. In order to obtain the optical properties of individual elements, the interaction between the neighbor units has to be considered. Moreover, for structures with periods comparable to the resonance wavelength, the waveguide boundary condition may introduce some artificial features.

We also performed simulations with periodic boundary conditions (PBC). Here, instead of a port eigenmode, a plane wave is used as excitation source. The field can only be detected with probes, which record one field component over frequency at a certain spatial position. Therefore, only the transmittance can be deduced, because incoming and reflected field amplitudes superimpose in front of the structure. The simulation volume has to be much larger in propagation direction, so that evanescent modes decay before the field is measured. This increases the simulation time by a factor between two and four. Compared to the waveguide geometry, deviations of the resonance positions are hardly visible.

In order to calculate the optical properties of metallic nanostructures by the numerical simulation tools, physical models have to be applied to the dielectric constants of metals. In our simulations by the FITD algorithm, the frequency dependent dielectric functions of metals in the near infrared range are described by the Drude model:

$$\varepsilon(\omega) = 1 - \frac{\omega_{pl}^2}{\omega^2 + i\omega_c\omega} \quad (3.1)$$

It offers a good correspondence to the measured data over a broad spectral range. For gold we use: $\omega_{pl} = 2\pi \times 2.175 \times 10^{15} \text{ s}^{-1}$ and the damping constant $\omega_c = 2\pi \times 6.5 \times 10^{12} \text{ s}^{-1}$ and for silver we use $\omega_{pl} = 2\pi \times 2.175 \times 10^{15} \text{ s}^{-1}$ and the damping constant $\omega_c = 2\pi \times 4.35 \times 10^{12} \text{ s}^{-1}$, which are obtained by fitting the Drude model to the experimental obtained data of Ref. [28].

4. Plasmon hybridization in three-dimensional optical metamaterials

4.1 Electric plasmon hybridization in stacked cut-wire metamaterials

4.1.1 Introduction

Stacking of 2D metamaterials is assumed to be the pathway towards the third dimension in the optical regime. However, this is a difficult task due to the limitations of current nanofabrication technology. To overcome these difficulties, here we suggest a simple and practical approach to increase the effective number of metamaterial layers, namely introducing a metal mirror. We would like to concentrate on the cut-wire design for 2D metamaterial stacking due to its ease of nanofabrication. In addition, stacking of metamaterials in general confronts another fundamental problem: vertical electromagnetic coupling of neighboring metamaterial layers has to be addressed. In this section, we also investigate the interaction of neighboring cut-wire layers and solve it elegantly with the method of plasmon hybridization [20-21].

4.1.2 Experimental results

Our samples were fabricated using standard electron beam lithography and thermal evaporation of the constitute materials followed by a lift-off procedure. Figs. 4.1A and 4.1B schematically illustrate the samples, which consist of gold cut-wires (sample I) and gold cut-wire pairs (sample II) separated from a thick continuous gold film by a MgF_2 dielectric layer. The sample parameters are given in the caption of Fig. 4.1. In sample II, the wire length and width of the upper gold cut-wire is smaller than that of the lower one as a result of the lift-off procedure. Figs. 4.1C and 4.1D show the images of sample I and II obtained by a

scanning electron microscopy (SEM), respectively.

The near-infrared reflectance spectra of the samples at normal incidence were measured by a Fourier-transform infrared spectrometer with the polarization as illustrated in Fig. 4.1. Measured reflectance spectra for samples I and II are characterized by black solid curves in electron microscopy (SEM), respectively.

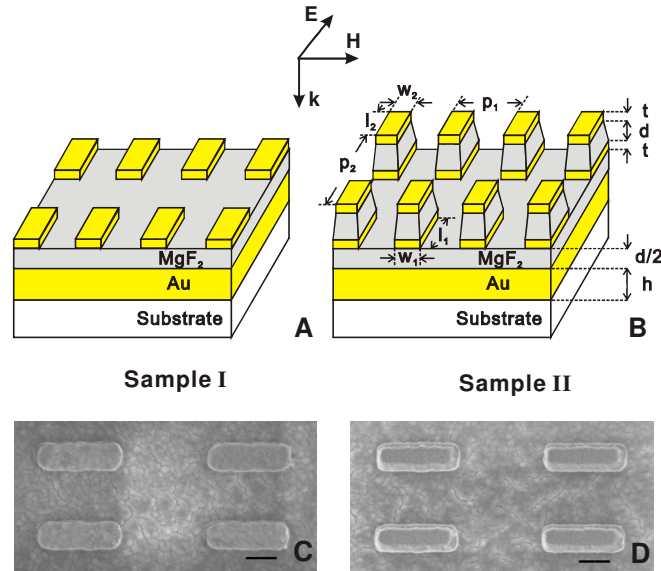


Figure 4.1: Schematic of the polarization configuration and the structure designs for sample I (A) and sample II (B). The geometry parameters are given as: $l_1 = 500$ nm, $w_1 = 170$ nm, $l_2 = 480$ nm, $w_2 = 150$ nm, $t = 20$ nm, $d = 80$ nm, $h = 200$ nm, $p_1 = 500$ nm, and $p_2 = 1050$ nm. Top-view SEM images of sample I (C) and sample II (D) as illustrated in (A) and (B), respectively. The scale bar in the pictures is 200 nm.

Figs. 4.2A and 4.2B, respectively. One resonance (I_a) is observed for sample I, whereas two resonances (II_a and II_b) are clearly visible in case of sample II for the entire observed spectral region. To theoretically investigate the observed experimental phenomena, a set of numerical simulations were performed using a Finite Integration Time Domain algorithm. For bulk gold, the permittivity in the infrared spectral regime is described by the Drude model with the plasma frequency $\omega_{p1} = 2\pi \times 2.175 \times 10^{15} \text{ s}^{-1}$ and the damping constant $\omega_c = 2\pi \times 6.5 \times 10^{12} \text{ s}^{-1}$ [28]. Owing to the surface scattering and grain boundary effects in the thin film, the simulation results are obtained using a higher damping constant which is three times as large as that in bulk. The permittivity of the glass substrate is taken as 2.25 and that of the MgF_2 spacer layer as 1.90. The simulated spectra for samples I and II are presented by grey dashed curves in Figs. 4.2A and 4.2B, respectively, which can be directly compared with the

experiment. The overall qualitative agreement between experimental and simulated results is very good, and the remaining discrepancies are likely due to fabrication tolerances in the experiment. This agreement proves that the simulations accurately describe the properties of the structures.

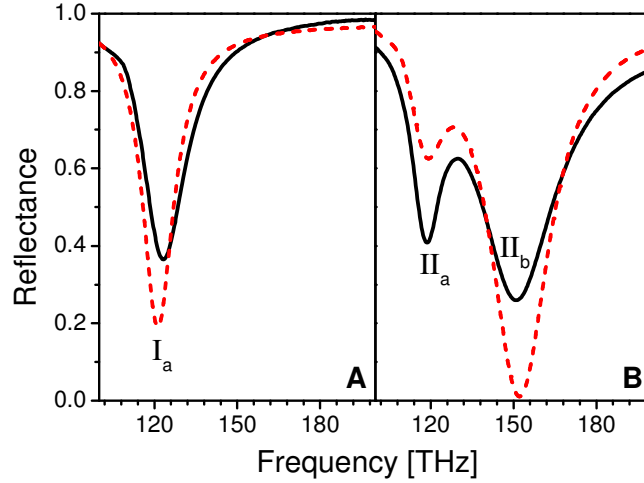


Figure 4.2: Experimental (black curves) and simulated (red dashed curves) reflectance spectra for sample I (A) and sample II (B).

Due to the presence of the thick gold film, there is nearly no transmittance in the optical regime; light can only be reflected or absorbed by the structures. For the analysis, however, it is easier to investigate the two samples in transmission geometry as cut-wires together with their images mirrored in the metal film [29, 30], as illustrated in Figs. 4.3A and 4.3B, respectively. To further elucidate the optical response of the cut-wire and metal film composites, it is very instructive to start by analyzing slightly different structures, namely directly stacked cut-wires and cut-wire pairs as shown in Figs. 4.3C and 4.3D, respectively. The optical response of a cut-wire excited by the external electromagnetic field can be characterized by a particle plasmon resonance. We therefore study the resonant behavior of stacked cut-wires based on the interaction of particle plasmons supported by the individual cut-wires. Actually, the concept of plasmon interaction and hybridization has been successfully used to describe plasmon resonances in complex nanostructures, for example in metallic nanoshells [20], nanoparticle dimers [31], and nanorice [21]. In the following, we first apply the plasmon hybridization method to investigate the resonant behavior of directly

stacked cut-wires, and subsequently use the analytic results to understand the optical response of cut-wires and cut-wire pairs above a metal surface.

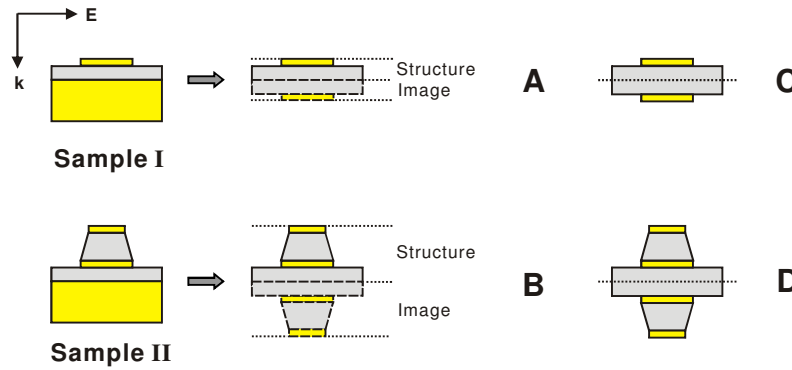


Figure 4.3: The schematic geometries for the equivalent structures of sample I (A) and sample II (B). Two stacked cut-wires (C). Four stacked cut-wires (D).

Numerical simulations were first carried out for the structure of two stacked cut-wires as shown in Fig. 4.3C. The transmittance spectrum is represented by the black solid curve in Fig. 4.4A, in which two plasmon resonances are clearly observable. The grey dashed curve in the same figure corresponds to a similar structure but with only the top gold cut-wire. Instead of two transmission minima, only one plasmon resonance is observed in this case. The above phenomena can be well interpreted using the method of plasmon hybridization [20, 21, 31]. When two identical gold cut-wires are brought in close proximity, the coupling leads to the lifting of the degeneracy of the bare plasmon modes and results in the formation of two new plasmon modes: the symmetric plasmon mode $|\omega_+\rangle$ and the antisymmetric plasmon mode $|\omega_-\rangle$. The symmetric and antisymmetric configurations correspond to the charge oscillations inside the two wires, moving in phase and out of phase, respectively. The frequency difference of the two modes can be understood as follows: for the symmetric (antisymmetric) mode, the charges at the ends of both wires repel (attract) each other. It leads to an increased (reduced) restoring force of the charge oscillation inside the wire when compared with that inside a single cut-wire and hence to a higher (lower) resonant frequency or energy. In the quasistatic limit, the $|\omega_-\rangle$ mode would be dark since the net dipole moment of the plasmons is zero for identical cut-wires [31]. Nevertheless, it can be excited in a real system because of phase-retardation effects. An energy diagram describing the plasmon hybridization resulting

from the two cut-wire interaction is illustrated in Fig. 4.4B. It is worth mentioning that the antisymmetric or magnetic mode, $|\omega_{-}\rangle$, is associated with a strong magnetic dipole moment and can reach negative permeability in a specific frequency range [15].

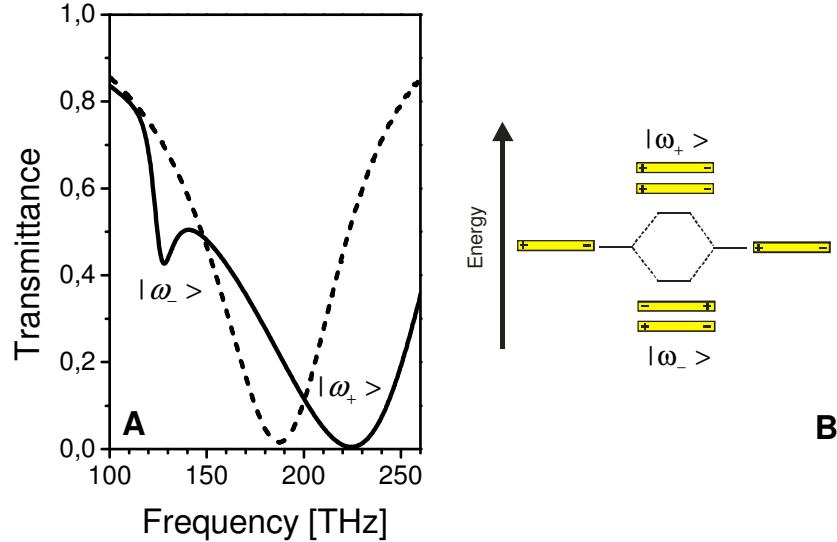


Figure 4.4: (A) Simulated transmittance spectra. The solid curve is the spectrum from two stacked cut-wires as illustrated in Fig. 4.3C. The dashed curve is the spectrum from a similar structure but with only the top cut-wire. (B) Schematic illustration of the plasmon hybridization in two coupled cut-wires. For the structure of a cut-wire above a metal mirror, only the antisymmetric mode $|\omega_{-}\rangle$ exists due to the parity of image interaction.

The plasmon hybridization method can also be applied to interpret plasmon responses of more complex metallic structures, such as four stacked cut-wires or two cut-wire pairs as illustrated in Fig. 4.3D. The corresponding spectrum is shown in Fig. 4.5A, where four plasmon resonances at different frequencies are observed. The hybridization of plasmons of the two coupled cut-wire pairs leads to four hybridized plasmon modes as schematically depicted in Fig. 4.5B. The $|\omega_{+}^{+}\rangle$ and $|\omega_{+}^{-}\rangle$ modes result from the interaction of the symmetric plasmons of the two cut-wire pairs. In case of the $|\omega_{+}^{+}\rangle$ mode, the charge oscillations inside the four cut-wires are all in phase, and thus the restoring forces between neighboring cut-wires are all repulsive. This leads to the $|\omega_{+}^{+}\rangle$ mode having the highest resonant energy among the four plasmon modes. Similar to the $|\omega_{-}\rangle$ mode in the two coupled cut-wire case, the $|\omega_{+}^{-}\rangle$ mode can be interpreted in terms of a magnetic resonance and can achieve negative values for the permeability (not shown here). Simultaneously, the formation of the $|\omega_{-}^{-}\rangle$ and $|\omega_{-}^{+}\rangle$ modes result from the coupling of the antisymmetric plasmons of the

two cut-wire pairs. The $|\omega^- \rangle$ mode has the lowest energy because the charge oscillation inside each cut-wire in this case is out of phase with respect to its neighboring cut-wire(s) and therefore the restoring forces between neighboring cut-wires are all attractive. Similarly, the $|\omega^- \rangle$ and $|\omega_+^- \rangle$ modes, which would be dark in the quasistatic limit, can be excited by light in a real system due to phase retardation. The $|\omega^+ \rangle$ mode would be bright even in the non-retarded limit because the top cut-wire is smaller than the bottom one. In principle, a coupling also exists between the symmetric and antisymmetric plasmons of the two cut-wire pairs but is ignored due to the larger energy separation [20].

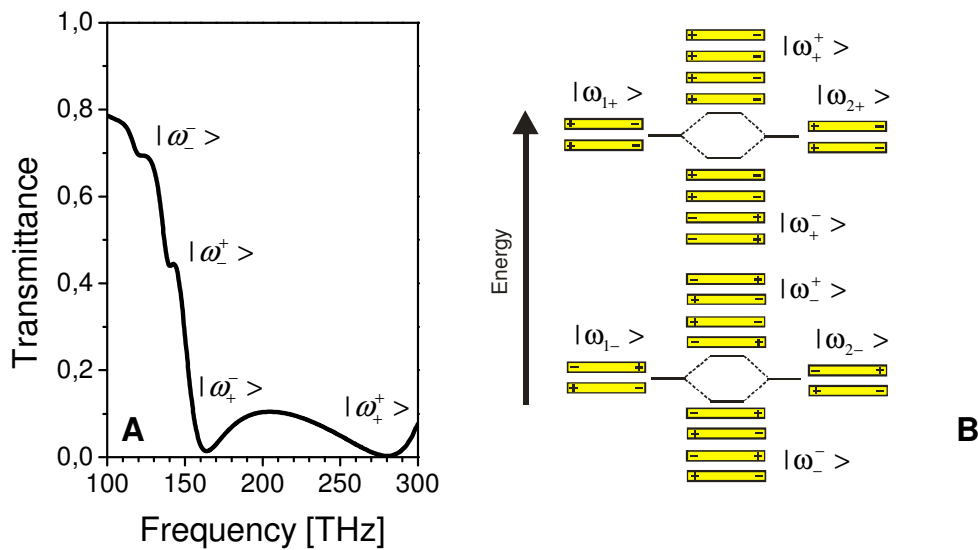


Figure 4.5: (A) Simulated transmittance spectrum from two coupled cut-wire pairs as illustrated in Fig. 4.3D. (B) Schematic illustration of the plasmon hybridization in two coupled cut-wire pairs. For the structure of a cut-wire pair above a metal mirror, only the antisymmetric-type modes $|\omega^- \rangle$ and $|\omega_+^- \rangle$ exist due to the parity of image interaction.

Compared to the coupling of directly stacked cut-wires, the plasmon hybridization method has to be slightly modified when considering the interaction of cut-wires and their mirror images. In the image model of the metal mirror, the charge distribution of the particle plasmon of a cut-wire induces its image in the metal mirror which is characterized by an inverted charge distribution [29]. Thus, for the structures of the cut-wire and cut-wire pair above metal mirrors, only the antisymmetric-type modes $|\omega^- \rangle$ (resonance I_a in Fig. 4.2A), $|\omega_+^- \rangle$ (resonance II_a in Fig. 4.2B), and $|\omega_+^- \rangle$ (resonance II_b in Fig. 4.2B) exist. Although only half the number of plasmon modes remains in case of image coupling, the characteristics of

stacked cut-wires are preserved by the cut-wire and metal film composites. In particular, the magnetic plasmon modes of directly stacked cut-wires can be mimicked by the interaction of cut-wires and their own images in the metal mirrors.

4.1.3 Summary

In conclusion, a simple, convenient, and practical method for stacking cut-wires in the third dimension using an additional metal mirror has been introduced [32]. The resonant behavior of cut-wires and cut-wire pairs above the mirror was investigated both experimentally and numerically. Our numerical simulations reveal good agreement with the experiment. The resonant properties of the cut-wire and metal film composites as well as directly stacked cut-wire structures are nicely visualized using the method of plasmon hybridization. The coupling analysis shows that only antisymmetric-type plasmon modes exist in the mirror case due to the parity of image interaction. Cut-wire systems in combination with a metal mirror display important resonance properties, especially the magnetic resonances of directly stacked cut-wires. Actually, the plasmon modes of the individual cut-wires hybridize to form composite plasmon modes of stacked cut-wires in a manner analogous to molecule formation from single atom wavefunctions [33]. Certainly, our method can be extended to three or more cut-wire layers above a mirror in order to construct thicker metamaterials. In principle, it might also be extended to more than one mirror layer, given the absorption to be small enough and the mirror layers to be thin enough. Our symmetry considerations with respect to the nodes of the wavefunctions [33] can be applied to these extensions as well. Furthermore, our analysis of the interaction of cut-wires based on plasmon hybridization provides further insight into the design of 3D metamaterials in the optical regime, where the coupling of thin basic metamaterial slabs is a key issue and cannot be ignored.

4.2 Magnetic plasmon hybridization in stacked fishnet metamaterials

4.2.1 Introduction

Coupling effects open up an avenue to intriguing physical and optical phenomena in metamaterials. A comprehensive understanding of the different coupling mechanisms is essential for unravelling the optical properties of metamaterials. In this section, we present a detailed study on the coupling effects in stacked magnetic metamaterials in the optical frequency regime. We demonstrate theoretically and experimentally the formation of ‘magnetic molecules’ from coupled ‘magnetic atoms’ in stacked fishnet metamaterials. We develop the concept of ‘magnetic molecules’ as well as ‘magnetic solids’, generalizing the plasmon hybridization scheme to N ‘magnetic atoms’ that form a ‘magnetic solid’. We explain the complex optical spectra as well as selection rules and introduce a new model to classify their symmetries. We show the evolution of effective material parameters with increasing layer numbers and point out limitations with respect to the applicability as negative refractive index materials.

4.2.2 Experimental results

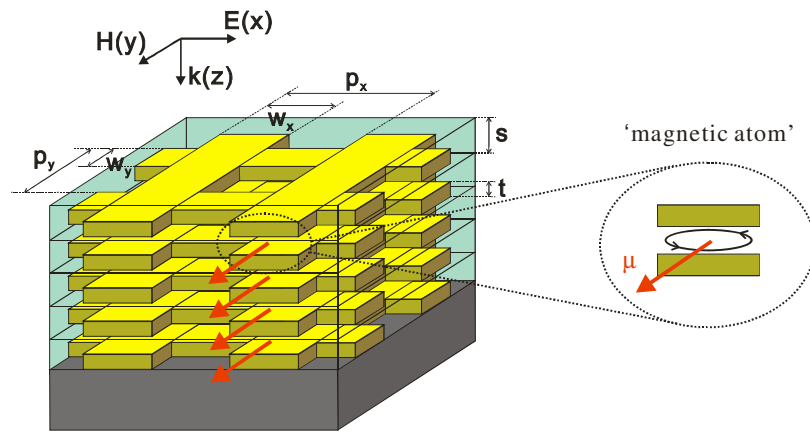


Figure 4.6: Schematic of the polarization configuration and the structure design for a 5-layer fishnet metamaterial. The geometry parameters are given as: $w_x = w_y = 350$ nm, $p_x = p_y = 600$ nm, $t = 30$ nm, and $s = 70$ nm. Right: The definition of a ‘magnetic atom’ is highlighted. The solid black circle represents the circular current excited between a double-wire pair. The red arrows in the figure denote the magnetic moments associated with the ‘magnetic atoms’. Here, we plot the specific mode with all magnetic moments aligned in parallel.

Fig. 4.6 shows the schematic of a stacked fishnet structure, which is constructed from five alternating layers of silver fishnets and dielectric spacers. In the structure, the wire widths, w_x and w_y are designed to be equal for the consideration of an improved polarization behavior,

i.e., polarization independence in x and y directions. In order to investigate the resonant behavior with the number of stacked layers, 2-, 3-, and 4-layer structures with the same geometry have been studied for comparative analysis. All numerical simulations were performed by employing a Finite Integration Time Domain algorithm. The permittivity of silver is described by the Drude model with the plasma frequency $\omega_{p1} = 1.37 \times 10^{16} \text{ s}^{-1}$ and the damping constant $\omega_c = 8.5 \times 10^{13} \text{ s}^{-1}$ [34]. A solidifiable photopolymer (PC403) is the choice for the dielectric spacers with the permittivity of 2.4, and that of the glass substrate is taken as 2.25. The simulated reflectance and transmittance spectra for different layers of structures are presented in Fig. 4.7A and 4.7B, respectively. The character of the resonances manifests itself in the reflectance spectra. As shown in Fig. 4.7A, one resonance (I_a) is observed for the 2-layer structure, whereas two resonances (II_a and II_b) are clearly visible in the case of the 3-layer structure. There are three (III_a , III_b , and III_c) and four (IV_a , IV_b , IV_c , and IV_d) resonances emerging in the case of 4- and 5-layer structures, respectively, for the entire observed spectral region.

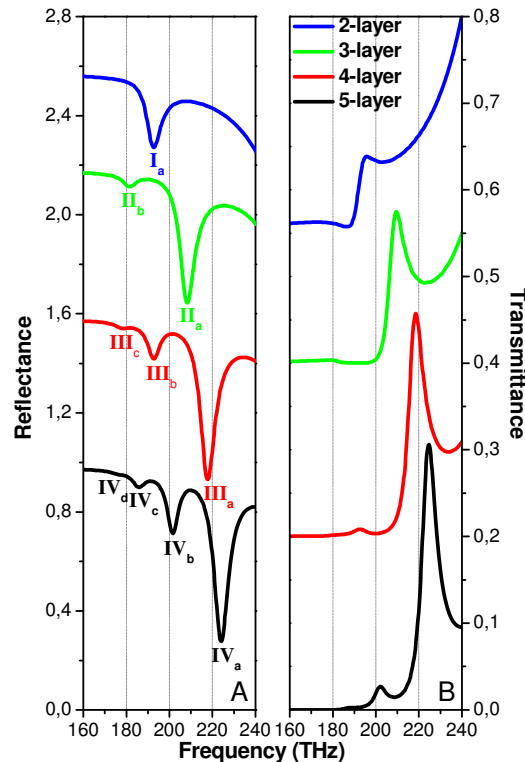


Figure 4.7: Simulated (A) reflectance and (B) transmittance spectra of 2-, 3-, 4-, and 5-layer fishnet metamaterials. Curves are shifted upwards for clarity.

To understand the origin of the spectral characteristics, the distributions of magnetic field H_y at the resonances for different layers of structures are depicted in Fig. 4.8. For clarity, the positions of the dielectric spacers between fishnet layers are marked by numbers in the corresponding figures. The magnetic field distribution at resonance I_a is illustrated in Fig. 4.8A. As has been intensively studied for the 2-layer fishnet structures [4, 16], the incident light field can induce an electric resonance (not shown) and a magnetic resonance at higher and lower frequencies, respectively. In the following, we would like to concentrate on the studies of the evolution of magnetic resonances with increasing fishnet layer numbers. Actually, for the 2-layer fishnet structures, the magnetic resonance is associated with the excitation of a circular current loop between the double-wire pair. This corresponds to an induced magnetic dipole moment inside the spacer layer, giving rise to a magnetic response to the incident electromagnetic field. In analogy to electric plasmons excited in metallic nanostructures, we define the magnetic dipole oscillation inside the spacer layer to be a magnetic plasmon. For the 3-layer structure, two circulating current loops are induced in the three-wire system, with the central metallic wire acting as the common layer for the flowing currents. It leads to the excitation of two localized magnetic dipole moments inside the neighboring spacer layers as depicted in Fig. 4.8B, oscillating in-phase and anti-phase with respect to one another at resonances II_a and II_b , respectively. The above phenomenon can be well interpreted using the hybridization of magnetic plasmons [35, 36]. The close proximity results in the coupling between the magnetic plasmons inside the two neighboring spacer layers and gives rise to the formation of two new hybridized modes: the symmetric mode and the antisymmetric mode. The resulting two magnetic resonances II_a and II_b blue-shift and red-shift, respectively, in comparison to resonance I_a , which corresponds to the bare mode of an individual magnetic plasmon. This is a clear signature of the interaction between the two plasmons. Taking this one step further, the 4-layer structure forms three hybridized modes as presented in Fig. 4.8C. One mode is fully symmetric (resonance III_a), one mode is fully antisymmetric (resonance III_c), and the intermediate mode is nonsymmetric between neighbors (resonance III_b). As demonstrated by the reflectance spectra of Fig. 4.7A, resonances III_a and III_c show a further blue-shift and red-shift compared to resonance I_a , respectively, whereas resonance III_b is situated nearly at the same spectral position of

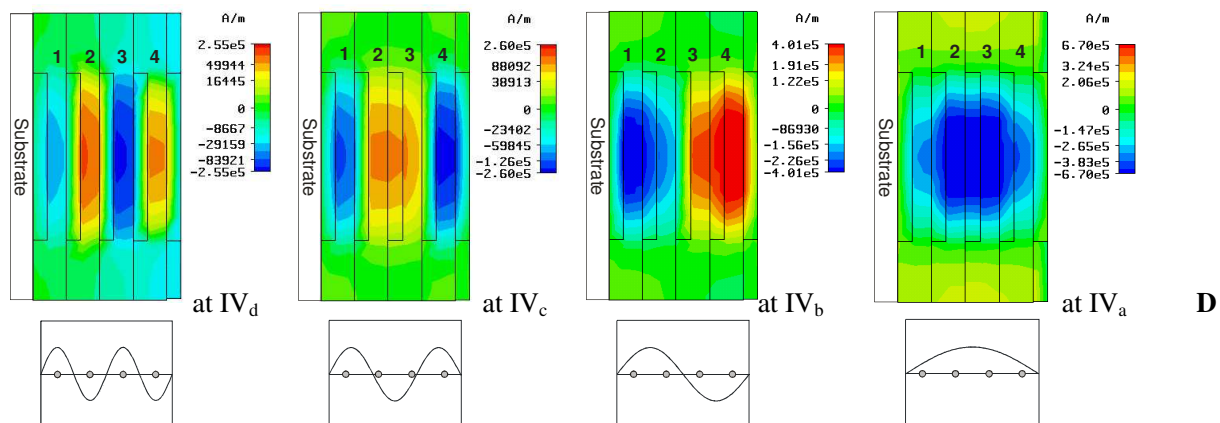
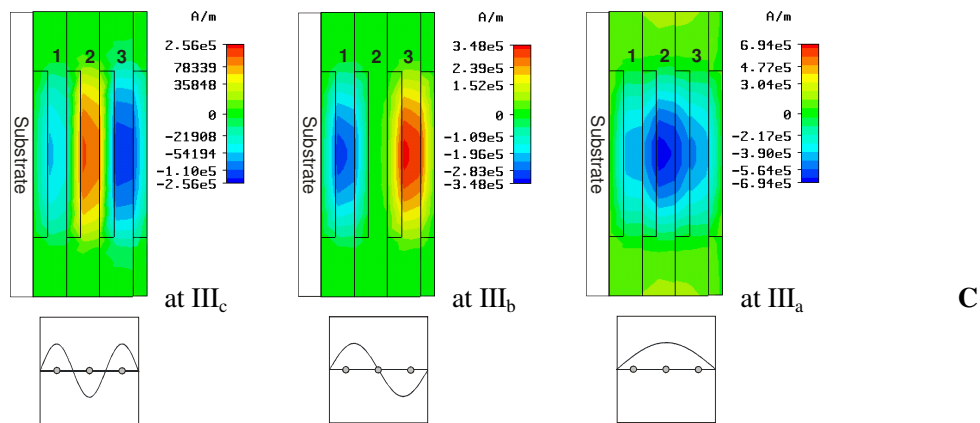
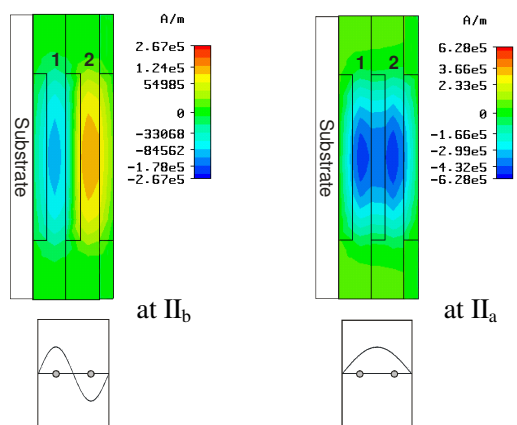
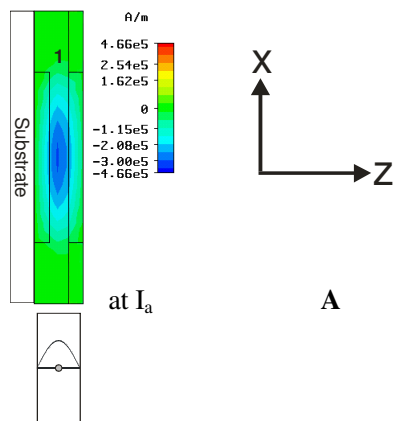


Figure 4.8: Simulated magnetic field distributions of H_y in the plane $y = 0$ at the corresponding resonant frequencies together with the schematic wavefunctions for (A) 2-, (B) 3-, (C) 4-, and (D) 5-layer fishnet metamaterials. The grey circles in the schematic drawings represent the ‘magnetic atoms’. The node number decreases with rising resonant frequency due to the transverse magnetic dipole-dipole coupling.

resonance I_a . Subsequently, as evident from the magnetic field distributions in Fig. 4.8D, the introduction of the fifth layer leads to the formation of four hybridized modes. The modes having the highest (resonance IV_a) and lowest (resonance IV_d) resonant energies correspond to fully symmetric and antisymmetric magnetic plasmon modes, respectively. The configurations of the intermediate modes are incomplete antisymmetric combinations of magnetic plasmons as illustrated in Fig. 4.8D. Consequently, the general effect of adding successive fishnet stacked layers is to introduce additional hybridized modes as well as to spread the range of resonant energies.

In fact, the whole picture discussed above is a compelling analogy to the formation of linear molecules from single atom wavefunctions [37]. In our case, each magnetic plasmon excited inside a double-wire pair can be regarded as an excitation of a ‘magnetic atom’ (see Fig. 4.6). When a second ‘magnetic atom’ is added, the interaction of the two ‘magnetic atoms’ leads to the energy splitting and the formation of symmetric and antisymmetric ‘molecular orbitals’. Subsequently, when further ‘atoms’ are added, the interaction of the ‘magnetic atoms’ with their nearest neighbors will result in additional energy levels and lead to the formation of complex artificial ‘magnetic molecules’. A schematic which describes the ‘molecule formation’ is illustrated in Fig. 4.9. The energy levels are constructed with the fully antisymmetric mode having the lowest and the fully symmetric mode having the highest energy, consistent with the picture of transverse dipole-dipole interaction. In addition, as illustrated in Fig. 4.8, counting the node number of the magnetic field component H_y lets us easily arrange the intermediate levels. The oscillator strength of the individual magnetic modes can also be deduced from the dipole arrangements: Neighboring antiparallel dipoles cancel each other, while neighboring parallel dipoles add up. As a consequence, the fully antisymmetric mode has very little oscillator strength, whereas the fully symmetric mode has the largest oscillator strength and therefore strongly couples to the light field. This

interpretation is confirmed by the simulated and experimental spectra in Figs. 4.7 and 4.11D, respectively. Intuitively, when N ‘magnetic atoms’ have been included, an energy band consisting of N different energy levels will be formed [37] as depicted in Fig. 4.9 and this constitutes a ‘magnetic solid’.

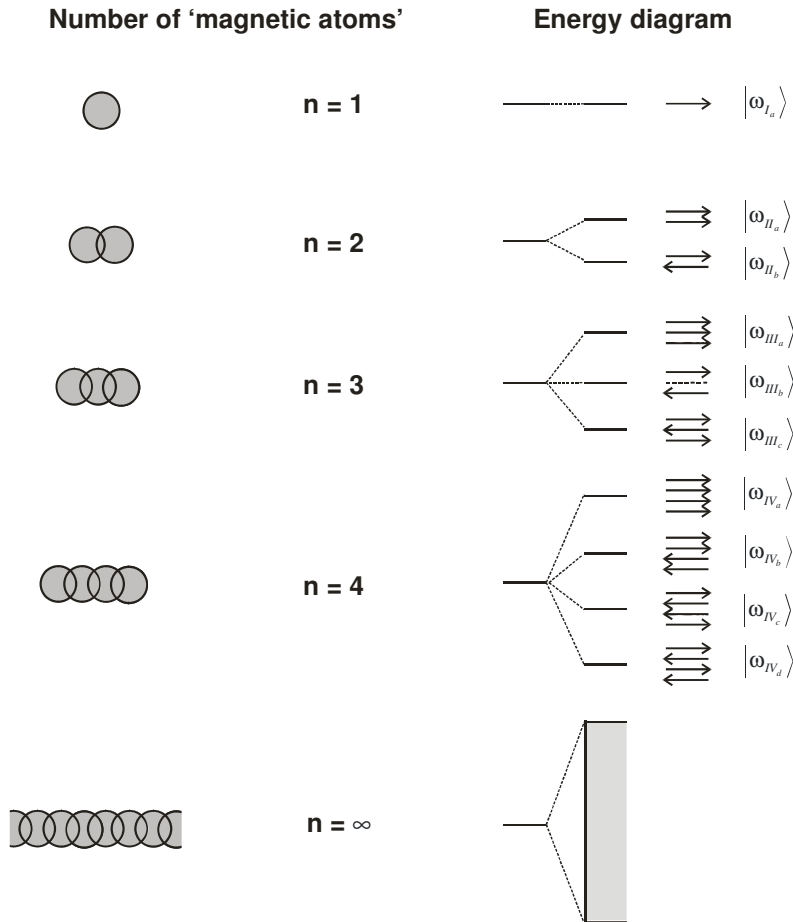


Figure 4.9: Energy diagrams describing the hybridization principle resulting from the interactions of magnetic plasmons in stacked fishnet metamaterials.

The effective metamaterial parameters of multilayer fishnet structures can be strongly influenced by the number of stacked layers. Fig. 4.10 shows the spectral behavior of permittivity (ϵ), permeability (μ), and refractive index (n), which were retrieved from numerical transmittance and reflectance data [38] for a different number of stacked layers. It is apparent that for the 2-layer structure, although μ does not become negative, n can still reach negative values in some frequency range near resonance I_a . This is due to the fact that n is described by the square root of $(Re(\epsilon)Re(\mu)-Im(\epsilon)Im(\mu))+i(Re(\epsilon)Im(\mu)+Im(\epsilon)Re(\mu))$ and the

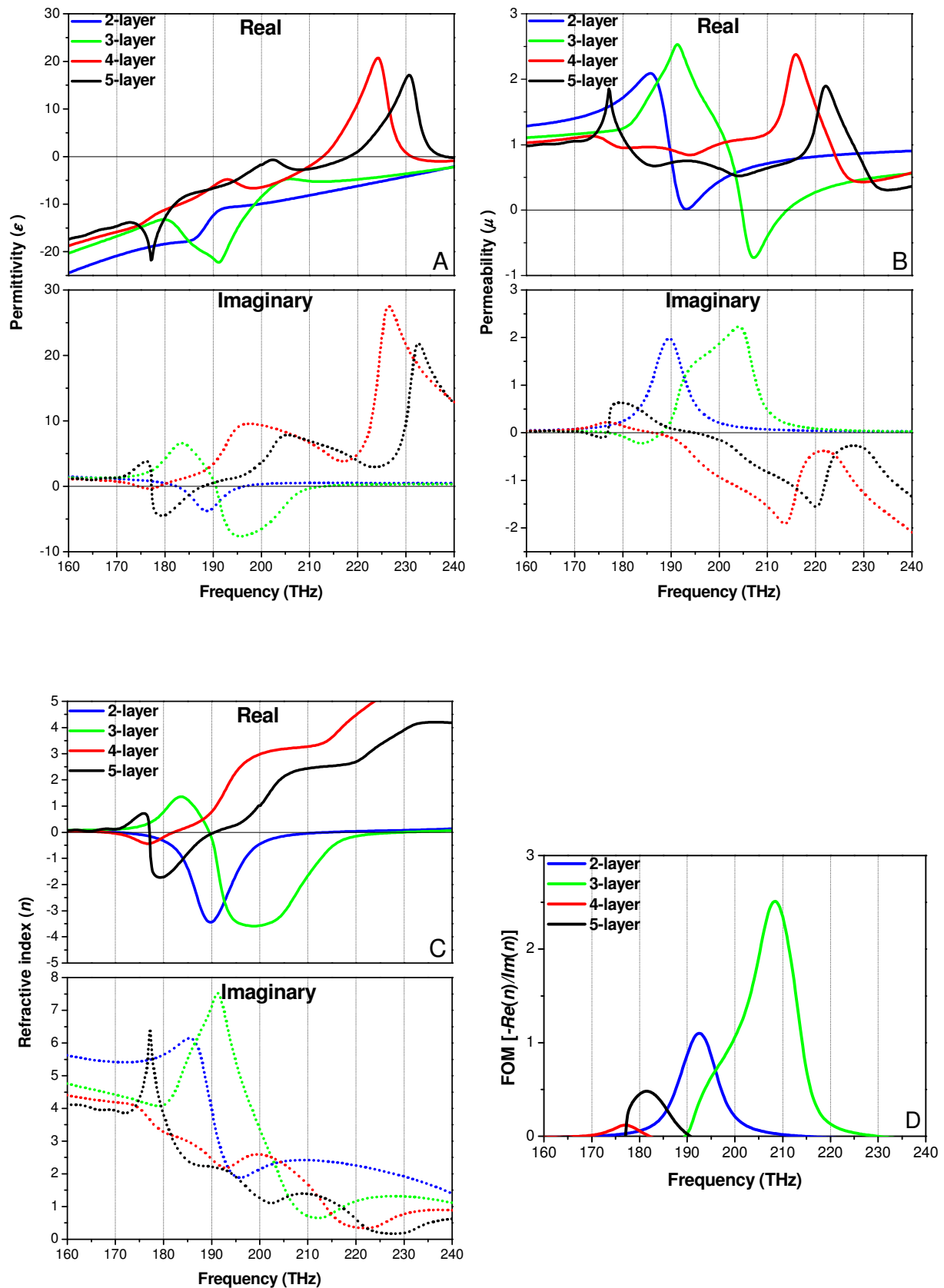


Figure 4.10: Retrieved effective material parameters (A) ϵ , (B) μ , (C) n , and (D) FOMs of 2-, 3-, 4-, and 5-layer fishnet metamaterials.

sign of $Re(n)$ is determined by the expression of $Re(\epsilon)Im(\mu)+Im(\epsilon)Re(\mu)$ [16]. Therefore, the occurrence of the negative refractive index for the 2-layer system is mainly attributed to the strong negative $Re(\epsilon)$ and the positive $Im(\mu)$ [16]. For the 3-layer structure, both $Re(\epsilon)$ and $Re(\mu)$ reach negative values near resonance II_a . This leads to the realization of a doubly negative material with a higher figure of merit [16] ($FOM = [-Re(n)/Im(n)]$) in comparison to the 2-layer structure (see Fig. 4.10D). For the 4- and 5-layer structures, one might have intuitively expected that negative values of $Re(n)$ should occur near resonances III_a and IV_a , respectively. The reason is that these two resonances are correlated with the excitation of fully symmetric magnetic plasmons, which can strongly counteract the external electromagnetic field and therefore lead to stronger negative magnetic responses. Nevertheless, the curves of $Re(n)$ in Fig. 4.10C for these two structures show that this intuitively expected behavior does not occur. $Re(n)$ becomes negative near resonances III_c and IV_c for the 4- and 5-layer structures, respectively. The negative $Re(n)$ arises from negative values of the expression $Re(\epsilon)Im(\mu)+Im(\epsilon)Re(\mu)$ at these frequencies, however, at the cost of dramatically lower FOMs when compared with the doubly negative refraction at resonance III_c (see Fig. 4.10D). The nonconvergence of the refractive index n with increasing layer numbers is resulting from the electromagnetic coupling of adjacent layers. This coupling mediates the excitation of higher-order Bloch modes, whose amplitudes may exceed those of the zeroth order Bloch mode, leading the dispersion of n to change strongly [39]. As a consequence, the material properties can be significantly altered by vertical metamaterial stacking due to the coupling of neighboring metamaterial slabs. This coupling effect is therefore a crucial issue which should be carefully considered for the design of three-dimensional optical metamaterials.

Finally, we manufactured the 5-layer fishnet structure by stacking nanofabrication technique. The electron micrographs of the sample were obtained by field-emission scanning electron microscopy. Fig. 4.11A presents an overview, indicating the high quality of the sample over a large area. Fig. 4.11B shows the image of an oblique view from another perspective. An enlarged oblique view is presented in Fig. 4.11C, in which the underlying fishnet layers are clearly observable. The inset of Fig. 4.11C depicts a focused-ion-beam cut of the sample, giving evidence that a 5-layer fishnet structure has been successfully fabricated. The near-infrared reflectance spectrum of the 5-layer metamaterial at normal incidence was

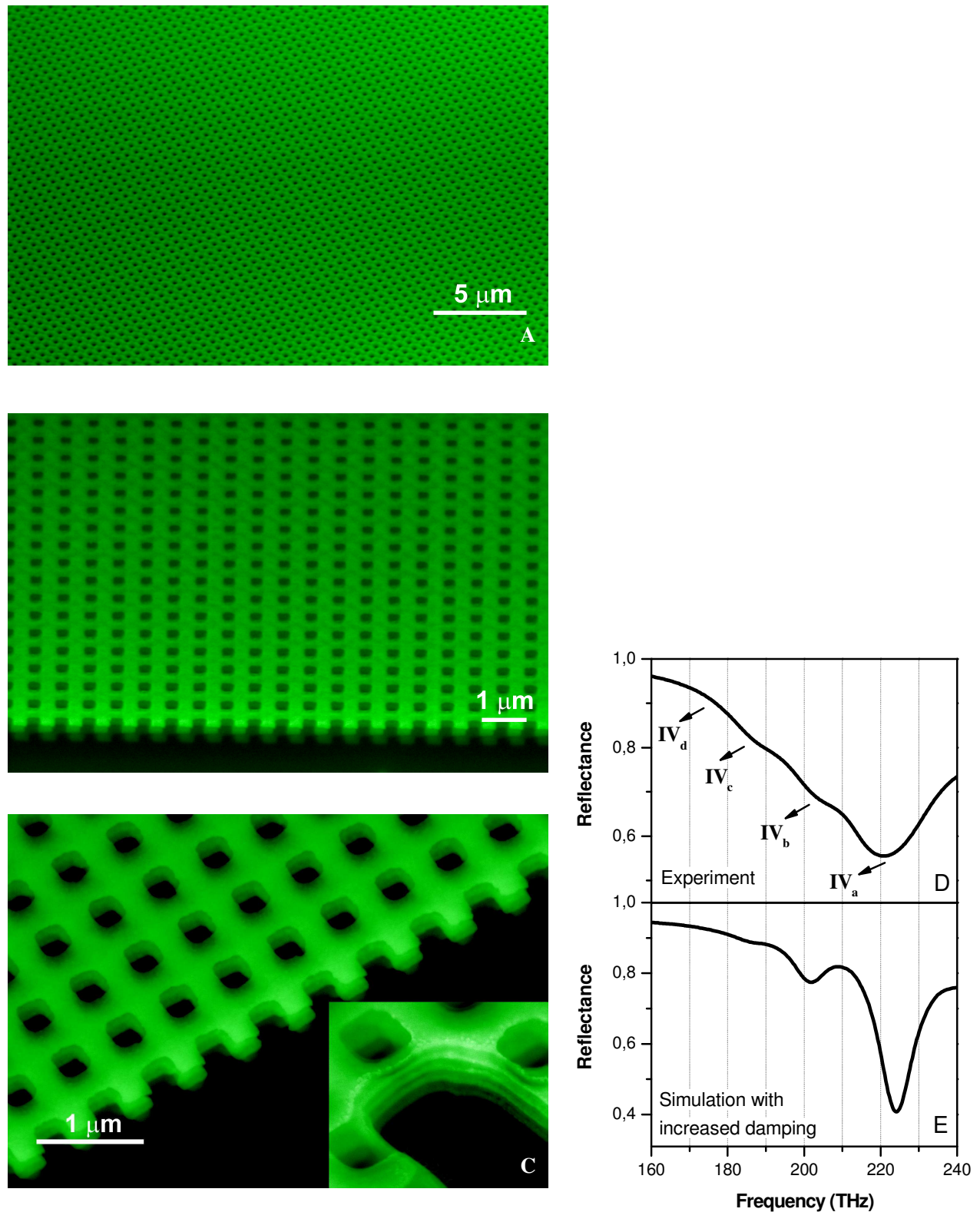


Figure 4.11: (A)-(C) SEM images of the fabricated 5-layer fishnet metamaterial. Inset of (C): A focused-ion-beam cut of the sample, demonstrating the layer number of the fabricated structure. (D) Experimental reflectance spectrum of this structure. (E) Simulated reflectance spectrum with a damping constant of silver which is two times larger than that used in Fig. 4.7, taking into account the surface scattering and grain boundary effects in the thin films.

measured by a Fourier-transform infrared spectrometer with electric field polarization as illustrated in Fig. 4.6. The measured reflectance spectrum is presented in Fig. 4.11D, in which four magnetic modes are visible. To our knowledge, this is the first experimental evidence of hybridization of magnetic plasmons in metamaterials. When comparing it with the corresponding simulated reflectance spectrum as given by the black curve in Fig. 4.7A, we find that the experimental result has an overall qualitative agreement with the numerical prediction but a less prominent resonant response. To obtain further insight regarding the resonant response, Fig. 4.11E presents the simulated reflectance spectrum with a damping constant of silver which is two times larger than that used in Fig. 4.7, taking into account the surface scattering and grain boundary effects in the thin films. The experimental result agrees well with the simulated result, and the discrepancies between them are also due to the fabrication tolerances in the experiment.

4.2.3 Summary

In conclusion, we have demonstrated that plasmonic building blocks can be utilized for the construction of ‘magnetic molecules’ in metamaterials [40]. In particular, we correlated the magnetic plasmons excited in stacked fishnet metamaterials with artificial ‘magnetic atoms’. We investigated in detail the evolution of the magnetic response with respect to increasing layer number. We demonstrated that the plasmon hybridization method, which is generally applied to describe electric interactions in complex metallic nanostructures, can also be used for understanding the magnetic interactions in stacked fishnet metamaterials. More specifically, the interaction of the magnetic plasmons or namely ‘magnetic atoms’ leads to the formation of artificial ‘magnetic molecules’, following the same hybridization mechanism of simple atoms bonded into linear molecules. An easy scheme for evaluating the oscillator strength of different coupled modes was proven to be applicable. Experiment and theory have agreed well. Furthermore, we have demonstrated that the material properties of stacked fishnet metamaterials are substantially modified as a consequence of vertical metamaterial stacking. This is a crucial issue that needs to be carefully taken into account, especially when considering the specific applications of metamaterials.

5. Coupling effects in split-ring resonator metamaterials

5.1 Planar split-ring resonators

5.1.1 Introduction

In this section, we demonstrate inductive coupling in planar metamaterials at optical frequencies. The key for this scheme is to use structural asymmetry in ‘metamaterial molecules’ so that phase retardation can be introduced between two constituent ‘atoms’ with convenient normal light incidence. Magnetoinductive (MI) coupling [22, 41, 42] is demonstrated in an SRR pair with internal 90° rotation asymmetry. The dual counterpart of MI coupling, namely electroinductive (EI) coupling [43] is shown in a complementary split-ring resonator (CSRR) pair with internal 90° rotation asymmetry. In each case, only one of the two ‘atomic’ constituents is excited by the external light field, and it interacts with its neighbor solely via inductive coupling. Babinet’s principle is applied to the ‘metamaterial molecule’, resulting in both a complementary spectral response and field distribution of the respective resonant modes [44, 45]. Finally, increasing the electromagnetic coupling strength between two ‘molecular’ constituents by introducing the mechanism of conductive coupling is presented as well [46].

5.1.2 Experimental results

Fig. 5.1 illustrates the geometries of SRR and CSRR pairs with the respective polarization configurations of the external light. Each resonator pair consists of two identical SRR or CSRR elements with internal 90° rotation asymmetry and resides on a glass substrate. In

order to explore theoretically the optical properties of the structures, numerical simulations were carried out using a Finite Integration Time Domain algorithm. The permittivity of the glass substrate is taken as 2.25. The optical constants of gold in the infrared spectral regime [28] are described by the Drude model with plasma frequency $\omega_{pl} = 1.37 \times 10^{16} \text{ s}^{-1}$ and damping constant $\omega_c = 4.08 \times 10^{13} \text{ s}^{-1}$. For excitation of the SRR pair, normally incident light is applied with polarization (E -field) along the x -direction as shown in Fig. 5.1A.

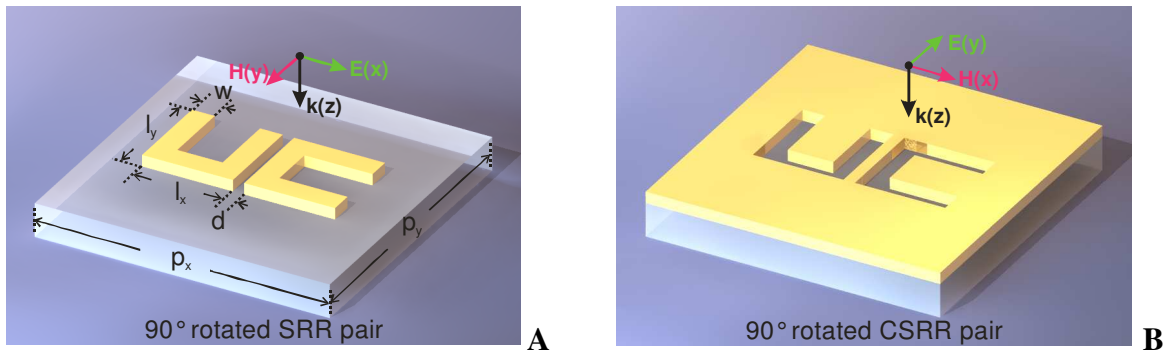


Figure 5.1: Schematic of the structure designs and the polarization configurations. (A) 90° rotated split-ring resonator (SRR) pair. (B) 90° rotated complimentary split-ring resonator (CSRR) pair. The geometry parameters are $l_x = 400 \text{ nm}$, $l_y = 400 \text{ nm}$, $w = 100 \text{ nm}$, $d = 50 \text{ nm}$, $p_x = p_y = 1300 \text{ nm}$, and the gold thickness $t = 50 \text{ nm}$.

The simulated transmittance and reflectance spectra are presented in Fig. 5.2A, in which two resonances (ω_1 and ω_2) are clearly observed. To clarify the origin of the spectral characteristics, current and field distributions at the relevant resonances are calculated and shown in Figs. 5.2C and 5.2D. It is evident that the circular currents excited in each of the two SRRs oscillate out-of-phase and in-phase at resonances ω_1 and ω_2 , respectively. Consequently, the two excited magnetic dipole moments are aligned antiparallel and parallel, accordingly. The magnetic dipole moment in the right SRR cannot be directly excited by the incident light due to its orientation with respect to the incident polarization. In a sense, the right SRR can be regarded as a ‘dark atom’ at the resonance frequency of the ring. Hence, the question arises as to how its magnetic dipole moment can be excited. In fact, it owes its excitation to MI coupling between the two SRR elements. More specifically, the external x -polarized light couples to the left SRR, which can be considered analogous to a ‘bright atom’. On resonance, excitation from the left resonator is transferred to the right one by inductive coupling, owing

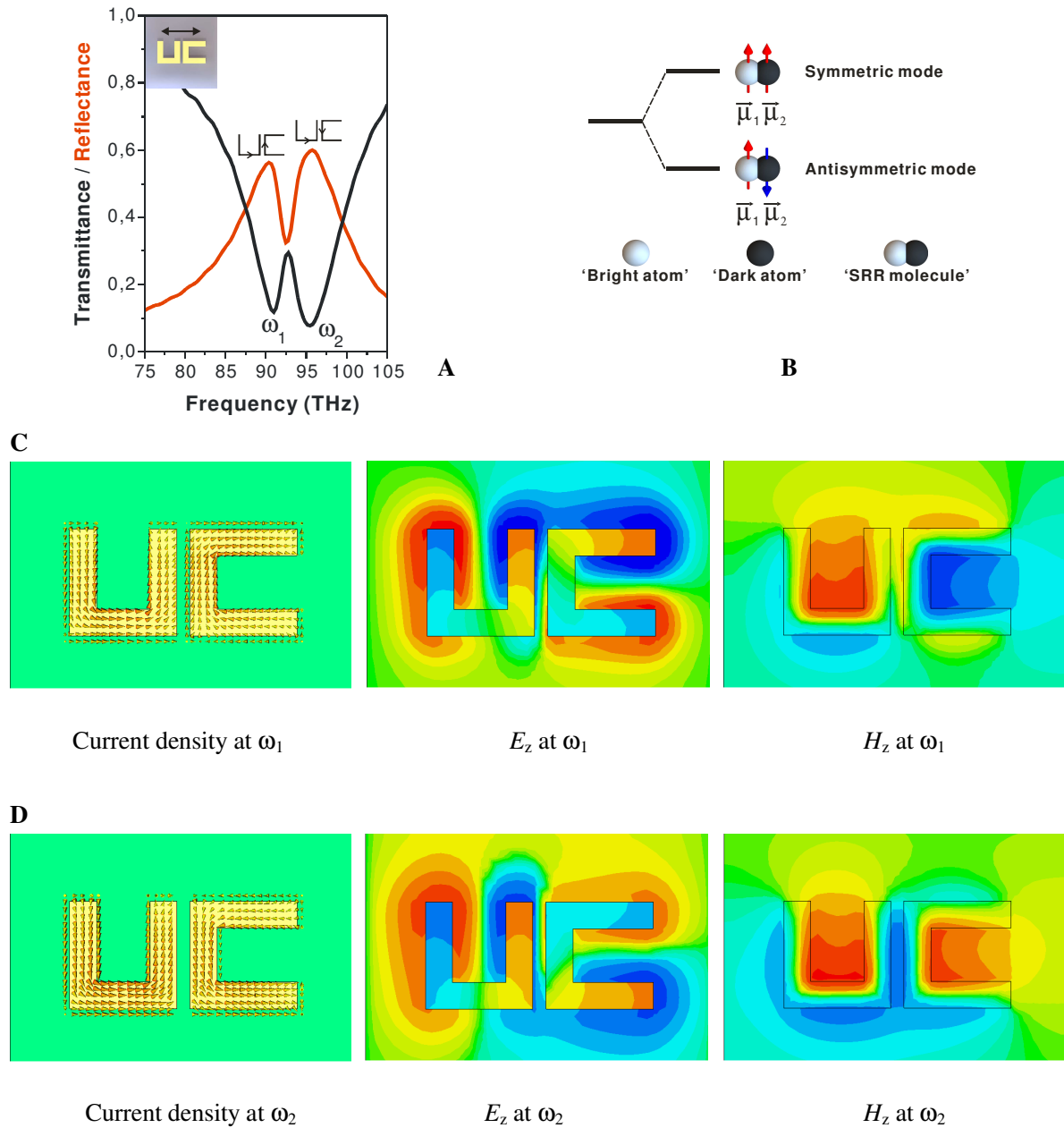


Figure 5.2: (A) Simulated transmittance and reflectance spectra of the 90° rotated SRR pair. The polarization of the electric field is horizontal as indicated in the inset. The symbols represent the currents in the SRRs at the respective resonances. (B) Schematic illustration of the formation of an 'SRR molecule'. Current and electric/magnetic field distributions at resonances ω_1 (C) and ω_2 (D) of the 90° rotated SRR pair.

to the mutual inductance between the two elements. The transverse interaction between the pair of SRRs leads to the formation of two new modes, namely, the antisymmetric and symmetric modes at ω_1 and ω_2 . In analogy to the states of two simple atoms hybridized into molecular orbitals, we term the resulting coupled system as '*SRR molecule*', in which the

‘bright and dark atoms’ are magnetoinductively coupled. An energy diagram depicting the formation of this ‘SRR molecule’ is illustrated in Fig. 5.2B.

Babinet’s principle is valid for SRR and CSRR metamaterials, even at optical frequencies [45]. Applying this concept to the optical response of CSRR pairs allows the observation of the complimentary effect to MI coupling, namely EI coupling, and it also elucidates the validity of Babinet’s principle for metamaterials consisting of coupled ‘metamaterial atoms’. As shown in Fig. 5.1B, the CSRR pair is illuminated by an incident wave polarized along the y -direction, which is complementary with respect to the excitation configuration of the SRR pair. The simulated transmittance and reflectance spectra are presented in Fig. 5.3A, in which two resonances (ω_{1c} and ω_{2c}) are noticeable. Apparently, the behavior of the transmittance/reflectance of the CSRR pair is interchanged with the reflectance/transmittance of the corresponding SRR pair as shown in Fig. 5.2A. This is in accordance with the predictions based on Babinet’s principle [44, 45]. The characteristic snapshots of current and field distributions at the relevant resonances are presented in Figs. 5.3C and 5.3D, respectively. From the electric field distributions, we find that in the CSRR pair, each CSRR element behaves like a point *electric* dipole normal to the CSRR plane [44]. This is a clear signature of duality between SRR and CSRR structures. More specifically, the electric dipole moments excited in the two CSRRs are antiparallel for resonance ω_{1c} , while they are parallel for resonance ω_{2c} . We interpret this behavior in terms of transverse interaction between the pair of CSRRs, which leads to the formation of two new modes, namely the antisymmetric and symmetric modes at ω_{1c} and ω_{2c} . The electric dipole in the right CSRR, which cannot be excited by the external light field, is induced by inductive coupling, resulting from the mutual inductance between the two CSRR elements. For parallelism, we term the resulting coupled system as ‘*CSRR molecule*’, in which the ‘bright and dark atoms’ are electroinductively coupled. An energy diagram depicting the formation of the ‘CSRR molecule’ is illustrated in Fig. 5.3B.

The electromagnetic coupling strength between two resonators can be altered by changing their relative distance. Due to the horizontal side-by-side arrangement, the distance between the centers of the two resonators cannot be significantly decreased. Stronger coupling strength

is expected for vertically stacked resonators, which are longitudinally coupled and can be very closely spaced. In order to effectively improve the coupling strength in *planar* SRR and CSRR pairs, the elements are being physically connected [46] as illustrated in Fig. 5.4A (4B). This can be termed *conductive* coupling. The simulated spectra are presented in Figs. 5.4C and 5.4D. For the sake of a direct comparison, the spectra of Fig. 5.2A and Fig. 5.3A are

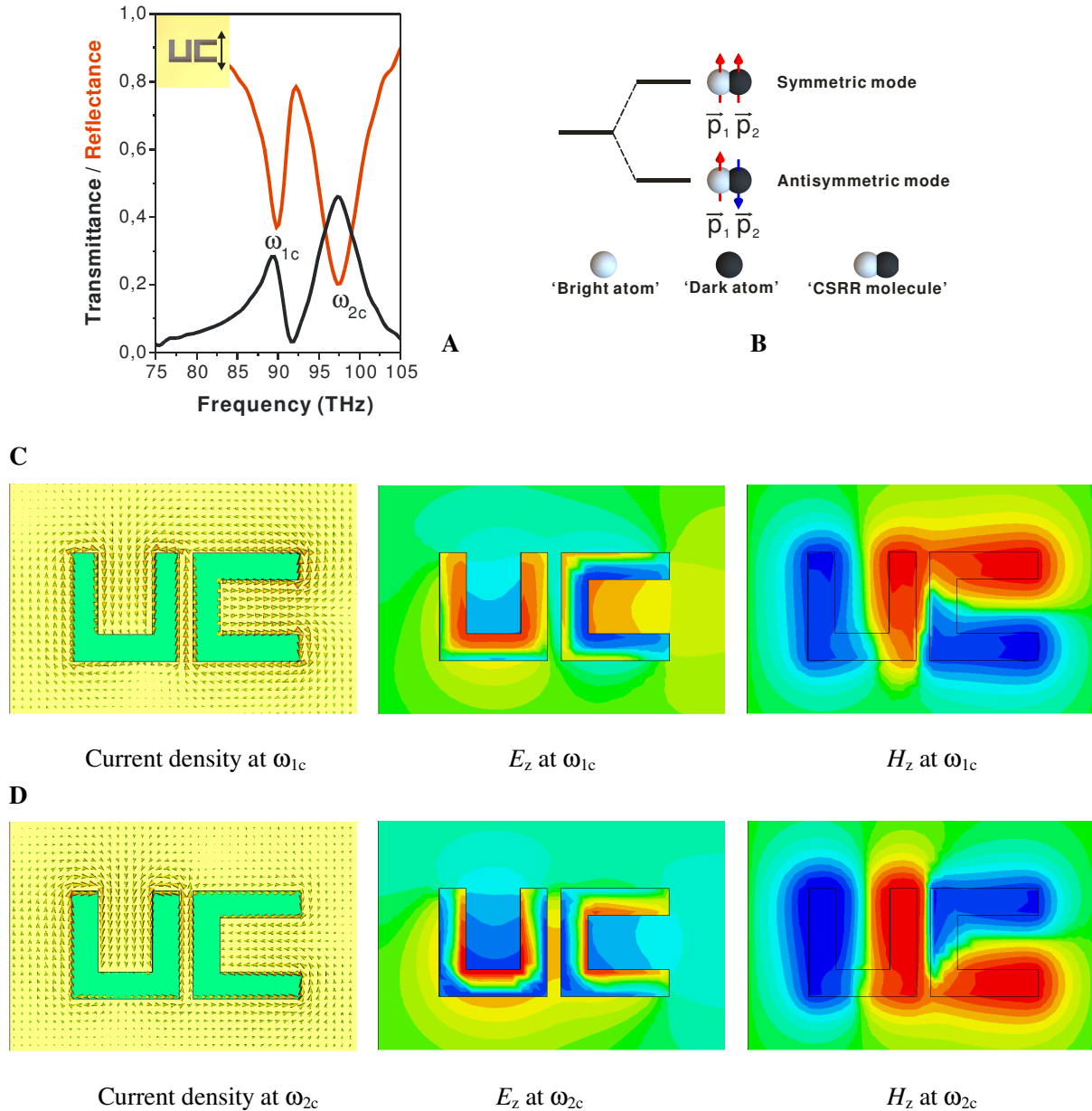


Figure 5.3: (A) Simulated transmittance and reflectance spectra of the 90° rotated CSRR pair. The polarization of the electric field is vertical as indicated in the inset. (B) Schematic illustration of the formation of a ‘CSRR molecule’. Current and electric/magnetic field distributions at resonances ω_{1c} (C) and ω_{2c} (D) of the 90° rotated CSRR pair.

replotted with dashed curves in Figs. 5.4C and 5.4D, respectively. For the connected structures, the spectral splittings that are directly correlated with the electromagnetic coupling strength are substantially enhanced. In particular, for both cases the antisymmetric modes (lower frequency resonances) show redshifts, which are stronger than the blueshifts of the symmetric modes (higher frequency resonances). To highlight the underlying physics of the

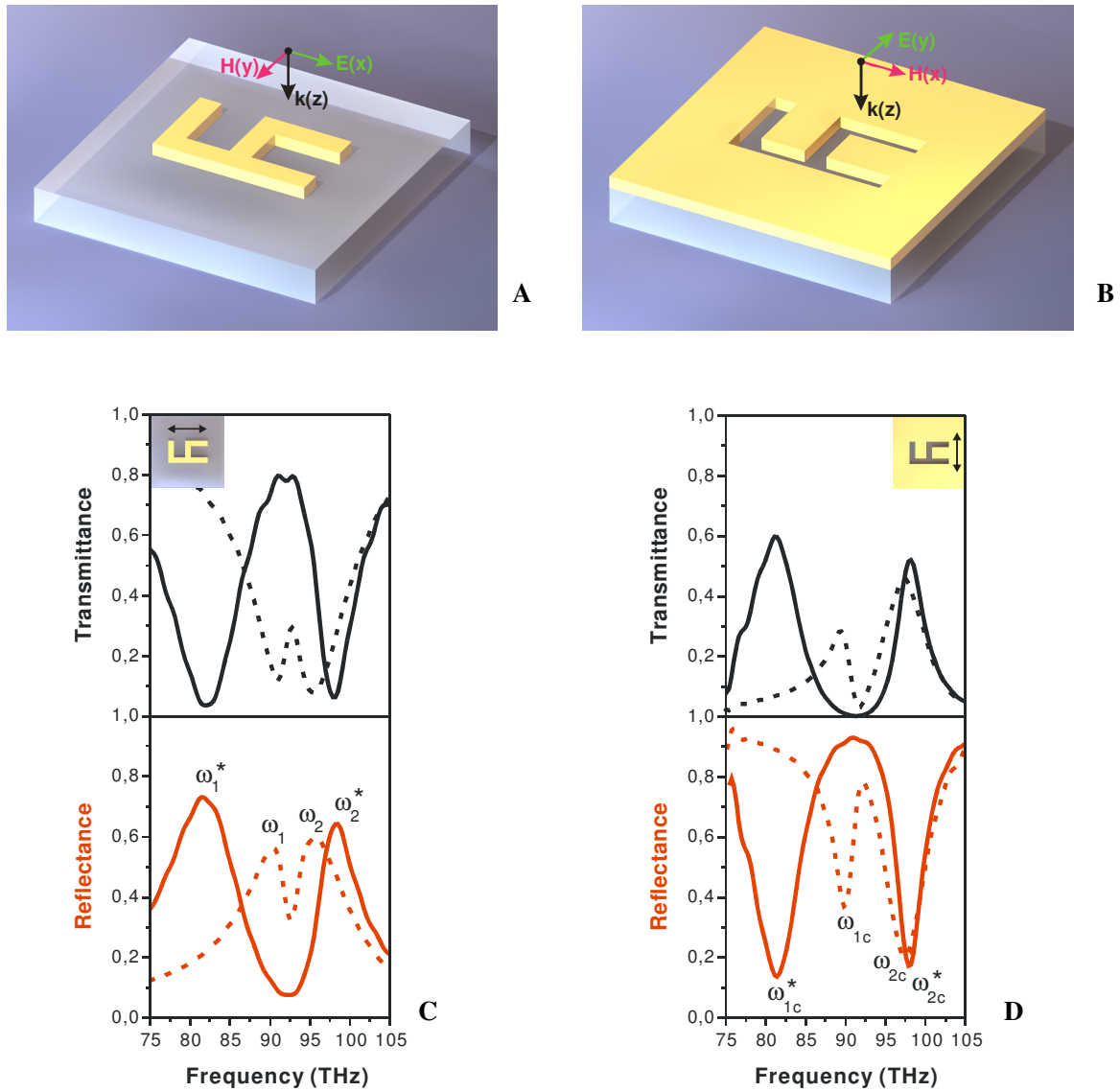


Figure 5.4: Schematic of the polarization configurations and the structure designs for a connected SRR pair (A) and a connected CSRR pair (B). Simulated transmittance and reflectance spectra for the connected SRR pair (solid curve) (C) and the connected CSRR pair (solid curve) (D). The spectra in Figs. 5.2A and 5.3A are replotted by dashed curves in (C) and (D), respectively. The polarizations of the electric field are indicated in the insets for each case.

asymmetric shifts, current distributions at corresponding resonances are given in Figs. 5.5A and 5.5B. In the cases of the antisymmetric modes, the connecting part acts as a link between two resonators. This allows the currents to contribute positively for both constituents. Consequently, in addition to enhanced inductive coupling due to the reduced distance, conductive coupling from the common conduction currents aids to further increase the coupling strength between the two SRR (CSRR) elements. On the other hand, in the cases of the symmetric modes, the currents from the connecting part contribute oppositely for both constituents. As a result, the interaction between the two SRR (CSRR) elements predominantly remains due to inductive coupling. Hence, the symmetric modes do not show prominent shifts when compared with those of the separated 90° rotated SRRs and CSRRs. Schematic illustrations of the asymmetric shifts for the two cases are depicted in Fig. 5.5C.

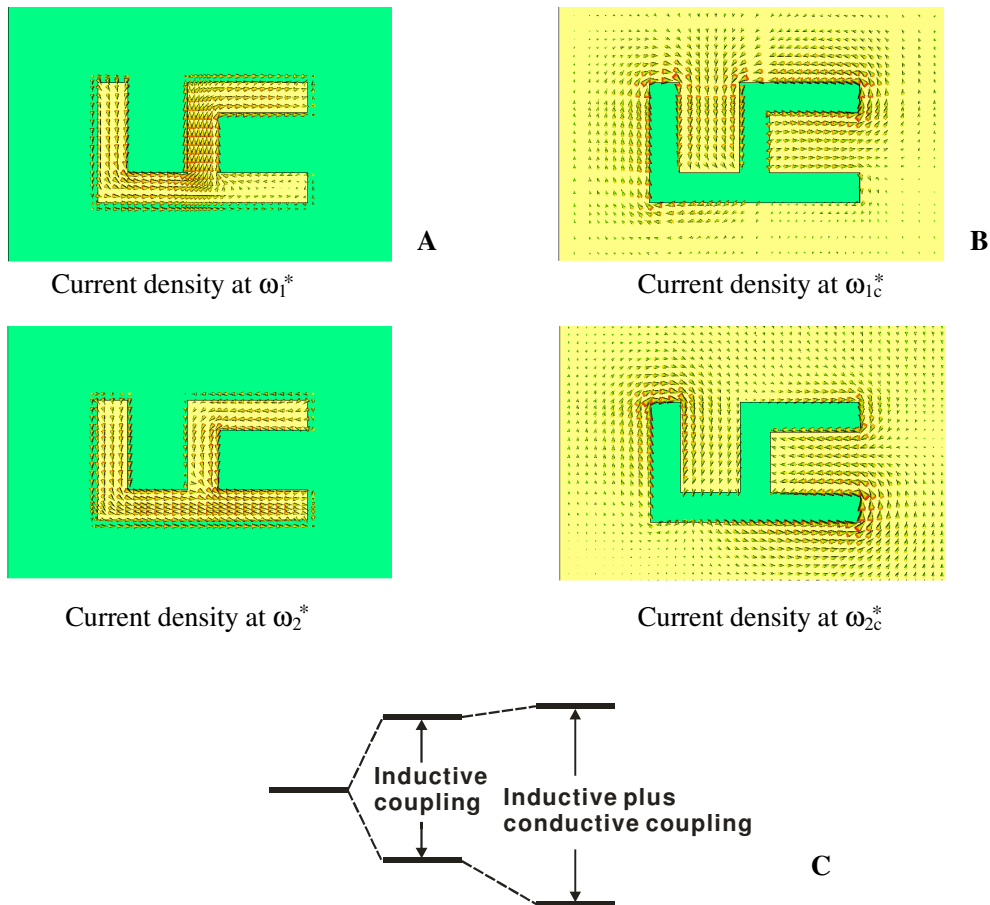


Figure 5.5: Current distributions at resonances, ω_1^* (A) and ω_2^* (B) of the connected SRR pair and ω_{1c}^* and ω_{2c}^* of the connected CSRR pair. C) Schematic illustration of the asymmetric shifts.

The designs of connected SRR and CSRR pairs are compatible with standard nanofabrication techniques. Figs. 5.6A and 5.6B show the structure images obtained by a scanning electron microscope. Both structures were fabricated on top of glass substrates with structural geometries as illustrated in Figs. 5.4A and 5.4B. Electron beam lithography was

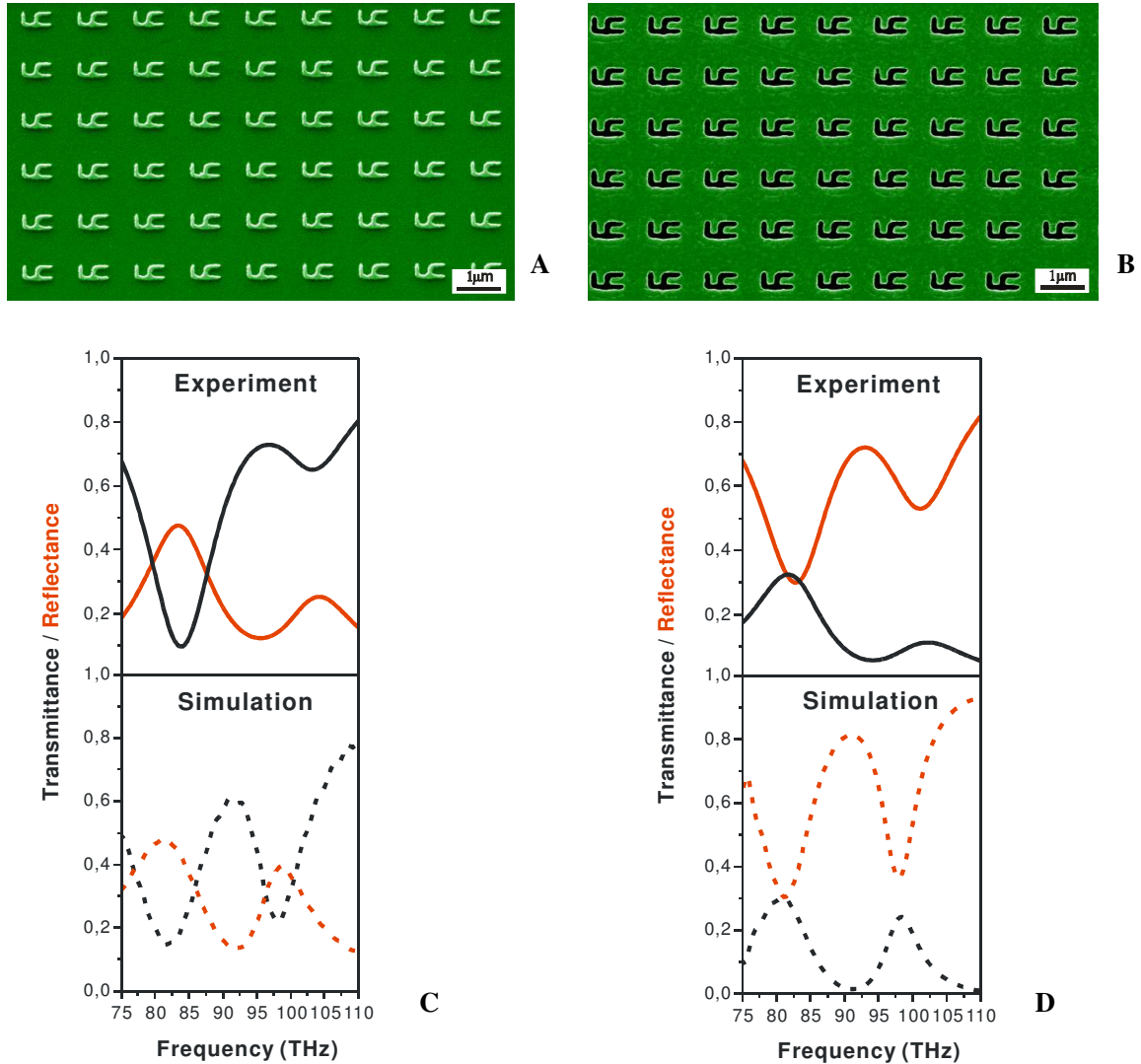


Figure 5.6: Scanning electron microscopy images of the fabricated samples. (A) Top-view of the connected SRR pair. (B) Top-view of the connected CSRR pair. Experimental (solid curves) and simulated (dashed curves) spectra for the connected SRR pair (C) and the connected CSRR pair (D). The polarization of the electric field is horizontal in the SRR case and vertical in the CSRR case. Simulated spectra are obtained by using gold with a higher damping constant which is three times as large as that used in Figs. 5.4C and 5.4D.

followed by Ar^+ ion plasma etching. The infrared transmittance and reflectance spectra of the samples at normal incidence were measured by a Fourier-transform infrared spectrometer

with the polarizations as indicated in Figs. 5.4A and 5.4B. Measured spectra are characterized by solid curves in Figs. 5.6C and 5.6D for the connected SRR and CSRR pairs, respectively. The corresponding simulated spectra are represented by dashed curves in the same figures. For a reasonable comparison with the experiment, in these simulations, gold with a three times higher damping constant [47] as that used in Figs. 5.4C and 5.4D is employed to account for the surface scattering and grain boundary effects in the thin film in real systems. The overall qualitative agreement between experiment and simulated results is good. The remaining discrepancies are likely due to fabrication tolerances in the experiment.

5.1.3 Summary

In conclusion, we investigated a new type of planar ‘metamaterial molecules’ working at optical frequencies, which consists of paired asymmetric resonators in each unit cell [48]. We demonstrated that inductive coupling enables the formation of ‘molecular states’ from two ‘metamaterial atoms’, one of which couples to the incident light whereas the other does not. Intriguingly, the ‘metamaterial molecules’ here also seem to be a classical analog of electromagnetically induced transparency [23]. As in atomic physics, a bright and a dark state can be introduced, and the polarization sensitive coherent coupling of two nearby resonances that can interfere provides the general recipe for electromagnetically induced transparency. We also showed that the coupling strength between the two molecular constituents can be improved by connecting the two elements in order to achieve conductive coupling. Our numerical simulations reveal good agreement with the experiment.

5.2 Three-dimensional split-ring resonator metamaterials

5.2.1 Introduction

While the physical properties of metamaterials can already be demonstrated in two-dimensional structures, the practical applications require 3D bulk-like structures [1, 10, 12]. This prerequisite has been achieved in the GHz range for microwave applications due to

the ease of fabrication by simply stacking printed circuit boards [1, 12]. In the optical domain, such an elegant method has been the missing building block towards the realization of 3D metamaterials. Here, we present a general recipe to manufacture 3D optical (infrared) metamaterials using a layer-by-layer technique [17-19]. Specifically, we introduce a fabrication process by means of planarization, lateral alignment, and stacking. We demonstrate stacked metamaterials, investigate the interaction between adjacent stacked layers, and analyze the optical properties of stacked metamaterials with respect to an increasing number of layers.

5.2.2 Experimental results

Fig. 5.7A schematically shows a four-layer SRR structure with its designed geometrical parameters. The nonplanar surface of the SRR metamaterial layers prevents stacking by simple serial exposure, development, and metal evaporation. Therefore, in our experiment, the surfaces of the SRR layers were flattened by applying a planarization procedure with dielectric spacers. The processing flow scheme is illustrated in Fig. 5.7B. First, an SRR layer is fabricated using a standard nanolithography procedure. A solidifiable photopolymer (PC403) was the choice for the subsequent planarization layer. To elucidate the effectiveness of the planarization, atomic force microscopy images and cross-section profiles of the gold SRRs before and after planarization by a 70 nm PC403 spacer layer are presented in Fig. 5.7C and 5.7D, respectively. As demonstrated by the cross-section profile in Fig. 5.7D, the roughness of the planarized surface was controlled within 5 nm, which represents a good platform for subsequent layer stacking. Improved planarized surfaces can be further obtained by applying multiple spin coatings of PC403 spacer layers (not shown here). Proper lateral alignment of different SRR layers is also crucial for successful stacking. This was achieved by adjusting the positions of the electron-beam exposure utilizing robust gold alignment marks with 250 nm thickness as illustrated in Fig. 5.7B. These gold marks were still clearly observable in the alignment steps after a series of anisotropic etching and planarization processes. The lateral

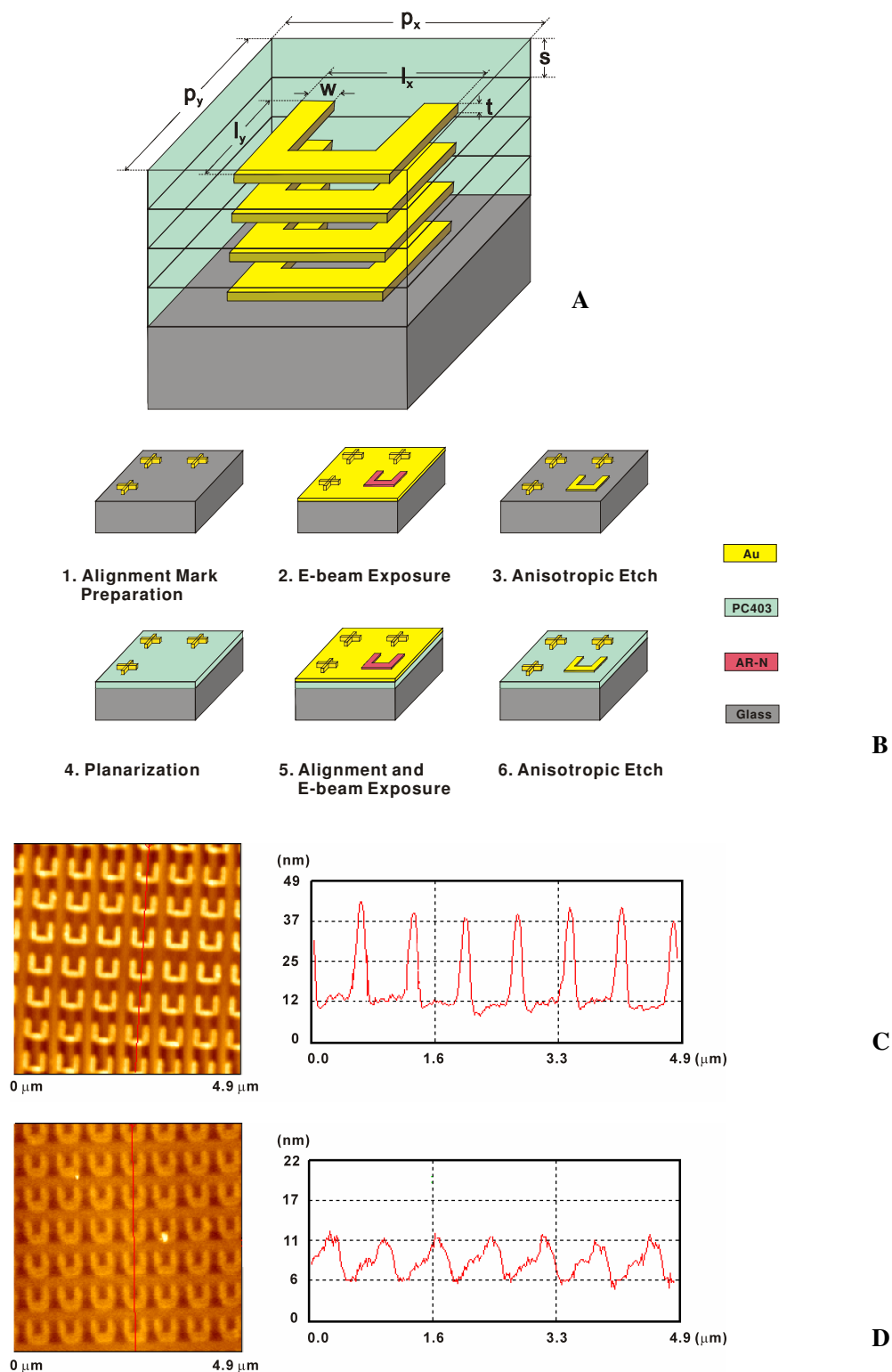


Figure 5.7: (A) Sketch of the structure with a definition of the geometrical parameters: $l_x = 430$ nm, $l_y = 380$ nm, $w = 80$ nm, $t = 20$ nm, $s = 70$ nm, $p_x = 700$ nm, and $p_y = 700$ nm. (B) Processing flow scheme. (C)-(D) Atomic force microscopy images and cross-section profiles of gold SRRs: (C) before planarization. The peak to valley height is approximately 27 nm. It is slightly larger than the original gold thickness of the SRRs, 20 nm, due to the presence of a thin layer of AR-N resist after etching. (D) after planarization with a 70 nm PC403. The peak to valley height is reduced to ~ 5 nm.

misalignment between the adjacent layers can be controlled within 10 nm in our electron-beam lithography system. The single-layer fabrication, planarization, and alignment procedures can then be repeated several times. Electron micrographs of the fabricated four-layer SRR sample were obtained by field-emission scanning electron microscopy. Fig. 5.8A presents an oblique incidence overview, which indicates the high quality of the sample over a large area. Fig. 5.8B shows the normal view, demonstrating excellent lateral alignment accuracy between different SRR layers. An enlarged oblique view is presented in Fig. 5.8C, in which the underlying SRRs are clearly visible, giving evidence that a well aligned four-layer SRR structure has been successfully fabricated.

In order to investigate the optical properties of the four-layer SRR structure, the spectral reflectance response of the sample at normal light incidence was evaluated using a Fourier-transform infrared spectrometer. The results are given by the black solid curves in Fig. 5.9A and 5.9B for parallel and perpendicular polarizations, respectively. The tiny reflectance dip around 50 THz for both polarizations is resulting from the material absorption of PC403, which does not affect the main resonant features. To clarify the origin of other spectral characteristics which are analyzed in detail below, numerical simulations were performed based on a commercial finite integration time domain algorithm. All geometrical parameters are indicated in Fig. 5.7A. The simulated spectra for the two polarizations are plotted using red dashed curves in Fig. 5.9A and 5.9B, respectively, which can be directly compared with the experiment. The overall qualitative agreement between experimental and simulated results is good, and the remaining discrepancies are due to fabrication tolerances in the experiment. As a complementary analysis to the numerical simulations, effective metamaterial parameters (i.e., ϵ_{eff} and μ_{eff}) were retrieved from numerical data for relevant linear polarizations [38]. In addition, to further reveal the underlying physics, characteristic snapshots of the simulated current distributions at resonant frequencies were also included.

Fig. 5.9C depicts the spectral behavior of ϵ_{eff} and μ_{eff} for the case of parallel polarization. At lower frequencies, two resonances around 60 and 80 THz are observed, respectively. As given in Fig. 5.9C, ϵ_{eff} shows a distinct dispersive behavior at the resonance around 80 THz with the real part of ϵ_{eff} dramatically changing from 14.5 to -7.5. The current distribution at

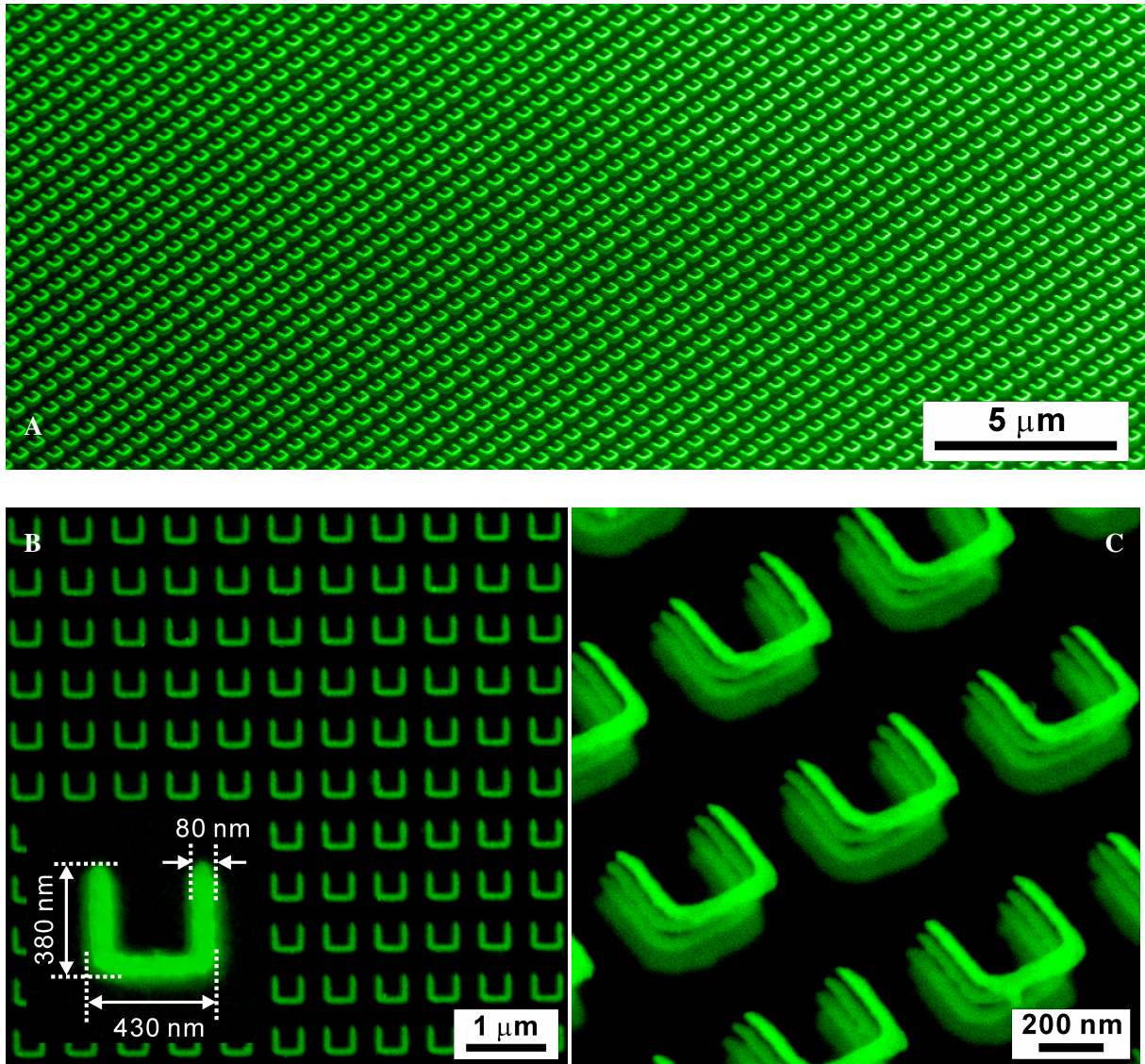


Figure 5.8: Field-emission scanning electron microscopy images of the four-layer SRR structure. (A) Oblique incidence overview. (B) Normal view. Inset, magnified view. (C) Enlarged oblique view. The lateral alignment is excellent.

this resonance is presented in Fig. 5.9C, where the electric coupling to the resonance induces the currents inside four SRRs circulating all in phase, i.e., the electric dipoles excited in each SRR oscillate in phase. The current distribution for the resonance around 60 THz is also depicted in Fig. 5.9C. Interestingly, at this resonance, the electric field drives currents inside the two top SRRs flowing at the opposite phase when compared to those inside the two bottom SRRs. The anti-phase electric dipoles counteract each other and thus contribute little to ϵ_{eff} . The above phenomena can be well interpreted using the method of plasmon hybridization [20]. The incident light field induces dipole-like plasmon excitations inside the

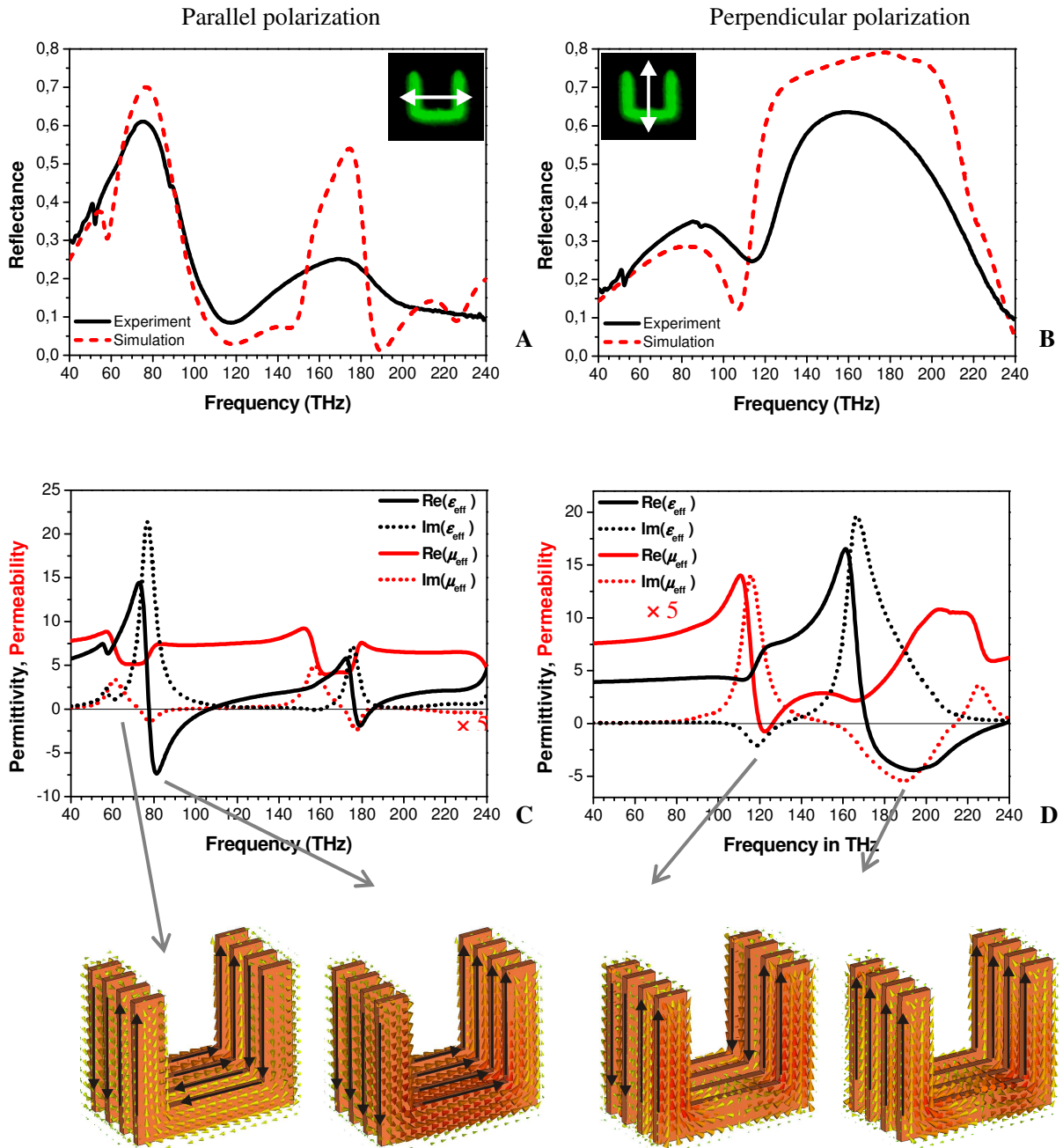


Figure 5.9: Experimental measurement and numerical simulation for the four-layer structure. Reflectance spectra, retrieved effective parameters, and current distributions at resonances of the four-layer SRR structure for parallel polarization (A,C) and perpendicular polarization (B,D).

SRRs, which are associated with charge density oscillations along the individual SRRs. The close proximity of the neighboring layers leads to electromagnetic coupling between the plasmons inside the adjacent SRRs. This vertical coupling results in the formation of two new hybridized modes: the symmetric plasmon mode and the antisymmetric plasmon mode. The

symmetric and antisymmetric configurations correspond to charge density oscillations inside the two top and the two bottom SRRs, moving in phase and out of phase, respectively. In general, the resonant frequencies of the plasmon modes are determined by the strength of the linear restoring forces. These forces appear as a result of electron displacement along SRRs induced by the incident electromagnetic field. For the case of the symmetric plasmon mode, the in-phase excitation of the charge density oscillations leads to increased restoring forces in the four SRRs due to repulsive forces between the arising identical charges, thus increasing the resonant frequency. In contrast, the antisymmetric charge oscillations lead to a lowering of the resonant frequency due to attractive forces between the opposite charges. The antisymmetric plasmon mode is not easily excited by light because the net dipole moment of the plasmons is zero for identical SRRs. The resonances located at higher frequencies in Fig. 5.9A are associated with the excitation of higher order plasmon modes, which will not be discussed here.

For light polarization with the electric field vector perpendicular to the SRR gaps, circular currents inside the SRRs cannot be excited due to the structural symmetry with respect to the direction of the electric field [3]. Negative values for ϵ_{eff} and μ_{eff} are observed, centered around 120 and 200 THz, respectively, as shown by the spectral curves in Fig. 5.9D. The illustrations of the current distributions in the same figure demonstrate that these two resonances are dominantly associated with plasmon excitations in the two arms of the ‘U’ structure, with currents flowing up and down in the two arms. More specifically, for the resonance at 200 THz, the currents in the arms of the four SRRs move all in phase. This results in the plasmons of the structure to be essentially a symmetric combination of individual SRR plasmons, giving rise to negative ϵ_{eff} in a wide frequency range from 170 THz to 235 THz. This interpretation is further supported when we analyze the resonant behavior at 120 THz. The current distribution at this resonance shows an antisymmetric combination of individual SRR plasmons, with the currents in the arms of two top SRRs oscillating out of phase when compared to those in the two bottom SRRs. The antiparallel currents result in a magnetic response to the incident electromagnetic field and influence the behavior of μ_{eff} . In particular, this antisymmetric plasmon mode can be interpreted in terms of a magnetic resonance in which the induced magnetic moment counteracts the external magnetic field and

leads to a negative response in the μ_{eff} spectral curve as manifested in Fig. 5.9D. In fact, the whole picture discussed above is very similar to that of stacked cut-wires [15, 32] because both structures exhibit qualitatively the same behavior: new plasmon modes are established originating from the vertical coupling of adjacent unit cells. The resulting symmetric and antisymmetric plasmon modes exhibit electric and magnetic responses, respectively, and can lead to negative ϵ_{eff} and μ_{eff} in certain frequency regions. It is worth mentioning that the existence of the antisymmetric plasmon modes for both polarizations is a specific result of vertical metamaterial stacking. In the quasistatic limit, the antisymmetric modes would be optically inactive and do not couple to the incident light. Nevertheless, they can be excited in

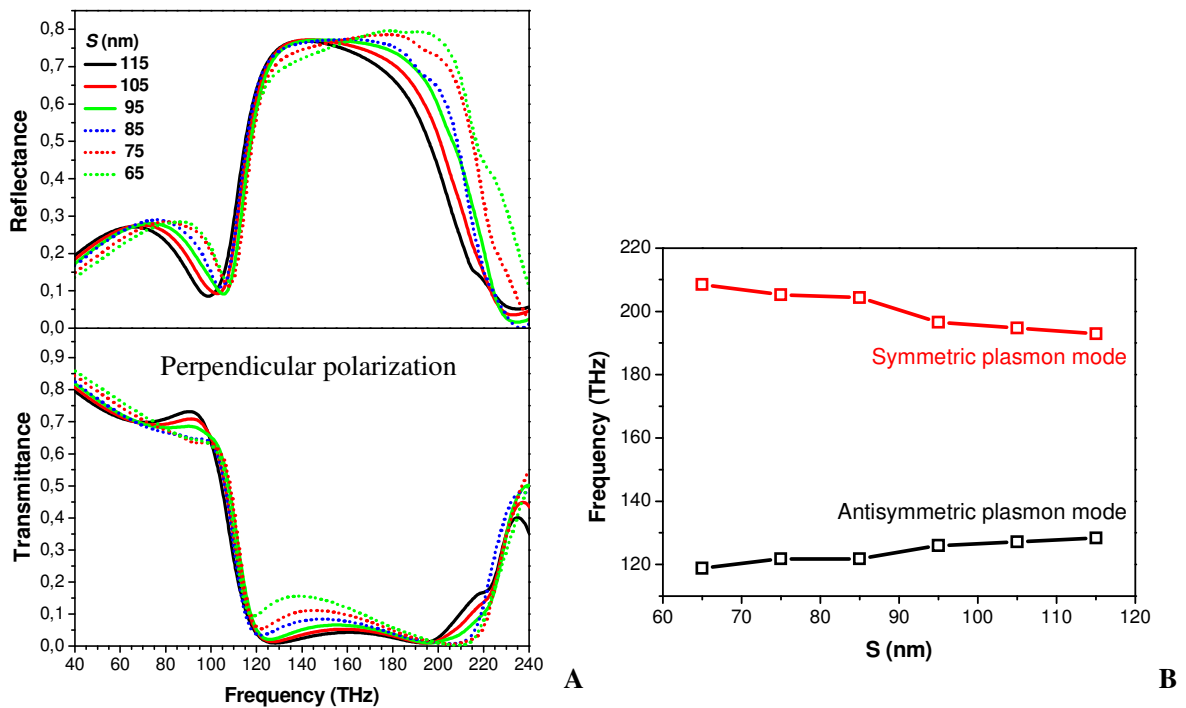


Figure 5.10: (A) Simulated reflectance and transmittance spectra as a function of spacer layer thickness for perpendicular polarization (see the inset of Fig. 5.9(B)). (B) Extracted resonant frequencies from (A).

a real system because of phase-retardation effects. In addition, due to the presence of the substrate and structural imperfections, the induced dipole moments in the four SRRs are not exactly equal. The antisymmetric plasmon mode in perpendicular polarization is more pronounced than that in parallel polarization due to stronger phase retardation, resulting from

a shorter resonant wavelength in comparison to the vertical spatial extension of the structure. In fact, the electromagnetic coupling between neighboring SRRs can be altered by changing the spacer layer thickness, the surrounding medium, or the sizes of SRRs. We restrict ourselves here to the influence of the spacer layer thickness for the four-layer SRR structure in the case of perpendicular polarization. The simulated reflectance and transmittance spectra are displayed in Fig. 5.10A in dependence of the spacer layer thickness s . To highlight the main phenomena, the spectral positions of the transmittance minima are extracted and presented in Fig. 5.10B.

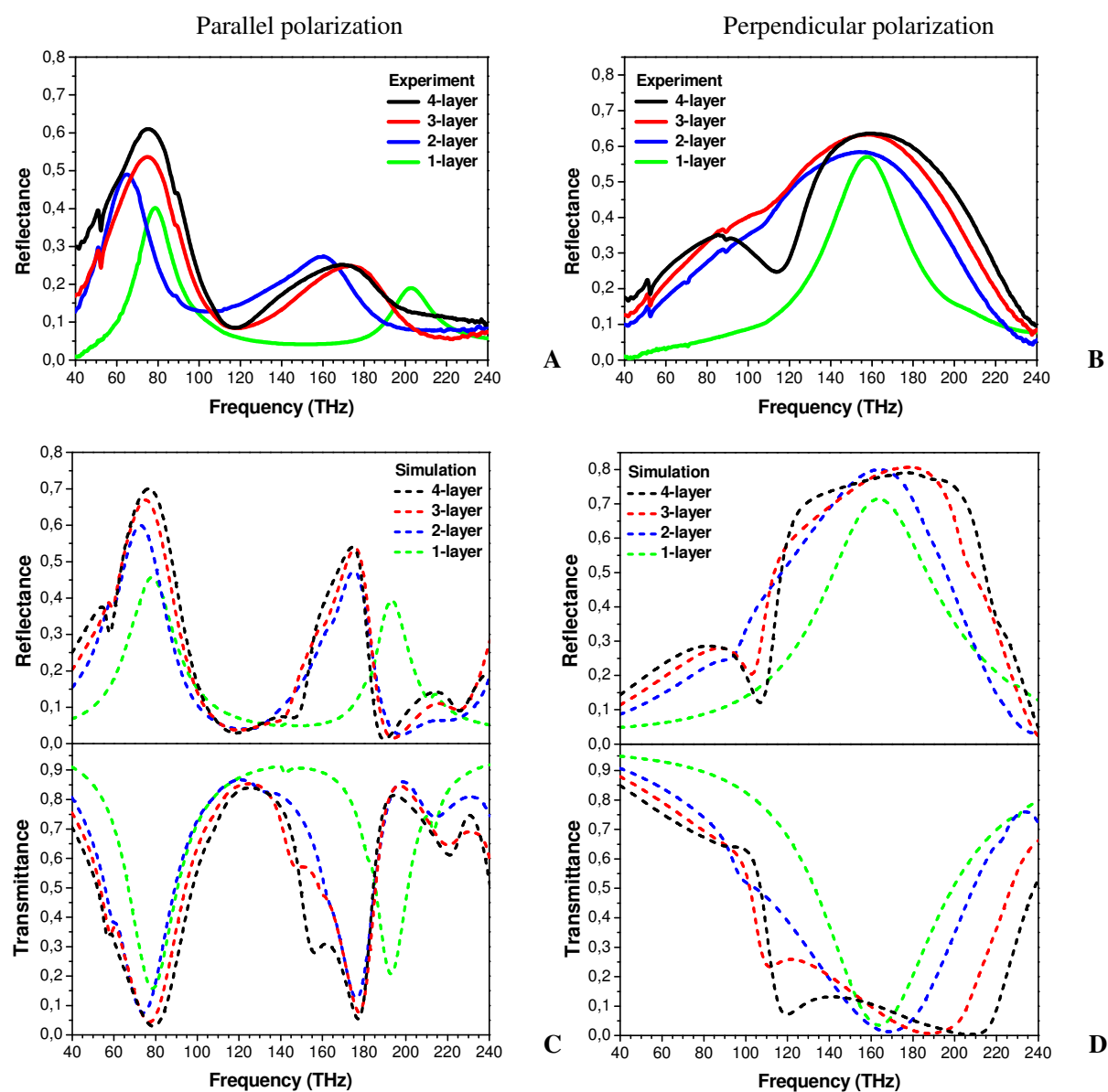


Figure 5.11: Experimental and simulated reflectance and transmittance spectra for parallel polarization (A,C) and perpendicular polarization (B,D).

The red and black curves correspond to the symmetric and antisymmetric plasmon modes, respectively. It is apparent that the two plasmon modes show an opposite spectral behavior, i.e., the symmetric (antisymmetric) plasmon mode is shifting to lower (higher) frequencies when increasing the vertical SRR separation. Consequently, the spectral splitting of the symmetric and antisymmetric modes decreases as the spacer layer thickness increases, which implies a weaker electromagnetic coupling between neighboring SRRs. In the limit of large vertical distances, the response of stacked SRRs will strongly resemble the combination of isolated SRRs due to the non-interaction between the SRR layers. In other words, the electromagnetic coupling strength between neighboring SRRs, which is related to the spectral splitting of the plasmon modes, can be directly controlled by adjusting the vertical distance between the SRRs.

Finally, it is quite instructive to study the evolution of the resonant behavior in dependence of the number of stacked layers. Fig. 5.11 presents the experimental and simulated spectra for the structures from one- to four-layer SRRs for two orthogonal polarizations at normal incidence of light. The discrepancy between experimental and simulated results is due to the fabrication imperfections in the experiments. As shown in the parallel polarization column (Fig. 5.11A and 5.11C), the strength of the resonances at around 80 THz becomes larger with increasing layer number. Simultaneously, the broadening of the linewidths implies larger oscillator strengths of the stacked units and therefore a stronger coupling of the microscopic resonators to the light field. This can be attributed to the cooperative vertical interaction between adjacent SRR layers. Moreover, the resonance positions of the stacked structures show red-shifts in comparison to that of the one-layer structure due to the presence of surrounding PC403 dielectric spacers. The experimental and simulated spectra for the perpendicular polarization are presented on the right column in Fig. 5.11B and 5.11D, respectively. It is evident that the reflectance peak and transmittance dip around 160 THz in the spectra of the one-layer structure gradually evolves into broad reflectance and transmittance bands, respectively in the case of multilayer structures. This is caused by the superposition of new plasmon resonances due to the energy splitting originating from the strong vertical coupling between adjacent layers.

5.2.3 Summary

The vertical interaction between metamaterial slabs can substantially change the optical properties of metamaterials and lead to new characteristic spectral features with increasing number of stacked layers [26]. The effect of stacking is thus a key issue that needs to be carefully considered, especially when taking into account specific applications. In particular, the resulting vertical coupling might be utilized in the design of broadband metamaterials. Stronger coupling will lead to increased bandwidth. Additionally, the occurrence of a negative μ_{eff} further suggests that 3D optical negative index materials in the future may be created by combining two sets of SRR structures [48], exhibiting negative ϵ_{eff} and μ_{eff} , respectively, at a common frequency range. The evolution of the optical response with increasing stacked layer numbers also provides general design principles as well as further insight into the optimization of 3D metamaterials at optical frequencies. Future tasks include the realization of low-loss negative *refractive index* materials as well as 3D chiral metamaterials [49, 50] in the optical frequency range using the presented stacking technique together with the investigation of coupling effects in these more complex systems. Balancing the number of stacked layers versus intrinsic losses will be the key to real world applications.

5.3 Optical magnetism

5.3.1 Introduction

Metamaterials offer the possibility to achieve artificial magnetism [2, 51] at optical frequencies without using inherently magnetic materials. By applying plasmonic metallic nanostructures with specifically tailored geometries, metamaterial dipoles can be excited and arranged in three dimensions [26, 32]. Such metamaterial nanostructures include split-ring resonators (SRRs) and cut-wire pairs [52-54]. The incident light field can excite circulating or displacement currents in these structures, in analogy to atomic orbital currents, giving rise to local magnetic dipole moments, namely, artificial “spins”. In this section, we demonstrate

longitudinal and transverse magnetic coupling in three-dimensional metamaterials at optical frequencies. In particular, by proper arrangement, magnetic dipole-dipole interaction can be isolated. More specifically, we show longitudinal magnetic interaction in a 90° twisted 4-layer SRR metamaterial and transverse magnetic interaction in a 5-layer fishnet metamaterial. Our concept of arranging magnetic dipoles in three dimensions according to a designer's plan and controlling magnetic coupling with multiple degrees of flexibility will allow the experimental study of classical magnetism in different varieties [55].

5.3.2 Design and characterization of metamaterial structures

Fig. 5.12A shows the schematic of a 4-layer twisted SRR metamaterial. Each gold SRR is twisted by 90° with respect to its vertical neighbor(s). In order to theoretically explore the resonant behavior of the structure, numerical simulations were carried out using a Finite Integration Time Domain algorithm. In simulation, the structure is surrounded by air with permittivity $\varepsilon = 1$. For excitation of the twisted SRR metamaterial, we utilize normally incident light with its polarization along the x -direction. The simulated transmission spectrum is presented in Fig. 5.13A, in which four resonances (ω_{L1} , ω_{L2} , ω_{L3} , and ω_{L4}) are clearly observable.

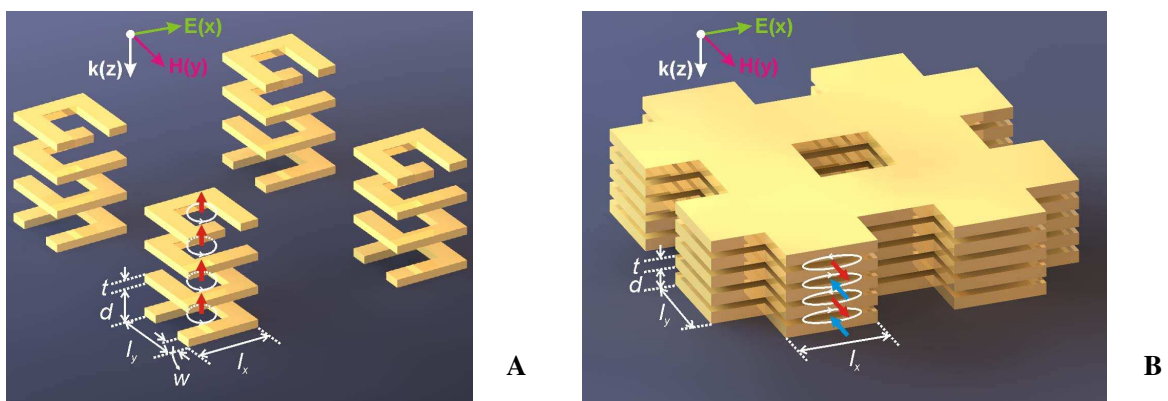


Figure 5.12: Structure geometry and polarization configuration. (A) 4-layer twisted SRR metamaterial. $l_x = l_y = 400$ nm, $w = 100$ nm, $t = 60$ nm, $d = 120$ nm, and the lattice constants in both x and y directions are 1200 nm. (B) 5-layer fishnet metamaterial. $l_x = l_y = 350$ nm, $t = 40$ nm, $d = 60$ nm, and the lattice constants in both x and y directions are 600 nm.

In order to clarify the origin of the spectral characteristics and to understand the physics of the magnetic response, the magnetic field intensity in dependence of the incident frequency is detected by a H_z probe, which is positioned at the center of the uppermost SRR. As shown in Fig. 5.13A, large enhancement of the localized magnetic field is achieved at the four resonances. To gain insight into the coupling mechanism, the magnetic field distributions of H_z at the corresponding resonances are shown in Fig. 5.14A. Each resonance is associated with the excitation of circular currents, thus giving rise to magnetic dipole moments in the individual SRRs. This elucidates that each SRR carries a magnetic moment, i.e., a classical “spin” in this analogy. Interestingly, because the electric fields in the slit gaps of neighboring SRRs are perpendicular to one another, the electric dipole-dipole interaction equals zero. In addition to

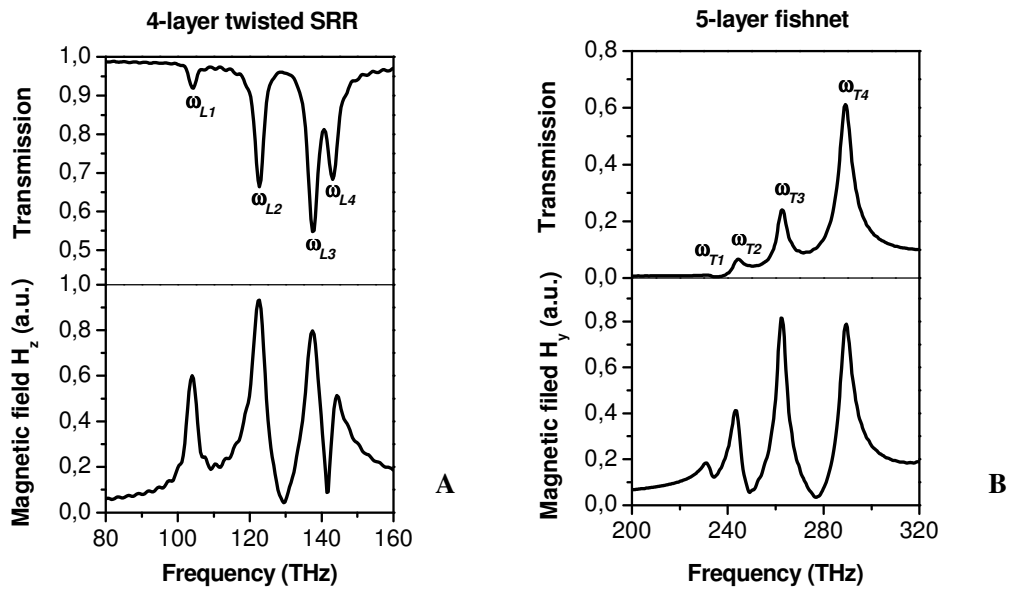


Figure 5.13: Optical spectra and magnetic field intensities. (A) Simulated transmission spectrum and detected H_z intensities for the 4-layer twisted SRR metamaterial (longitudinal coupling). (B) Simulated transmission spectrum and detected H_y intensities for the 5-layer fishnet metamaterial (transverse coupling).

the fact that the higher-order multipolar interaction is negligible in a first approximation, the electric coupling in the twisted SRR structure can thus be ignored. Therefore, we need to consider only magnetic interaction. For the twisted SRR structure, the excited four magnetic dipoles are *longitudinally* coupled. The close proximity of these neighboring magnetic dipoles results in strong interaction between them, giving rise to the hybridization of the magnetic response and the formation of new hybridized modes. The four magnetic dipoles tend to align

parallel. As a result, the fully parallel arrangement of these magnetic dipoles corresponds to the lowest frequency resonance (ω_{L1}). The intermediate resonances ω_{L2} and ω_{L3} are in terms of incomplete antiparallel arrangements of these magnetic dipoles, whereas at resonance ω_{L4} the four magnetic dipoles are aligned fully antiparallel. In fact, the resonance positions in the spectrum can be easily determined by counting the increasing number of nodes of the magnetic field as shown in Fig. 5.14A. A diagram depicting the interaction between these longitudinally coupled magnetic dipoles and the resulting hybridized modes is shown in Fig. 5.14A.

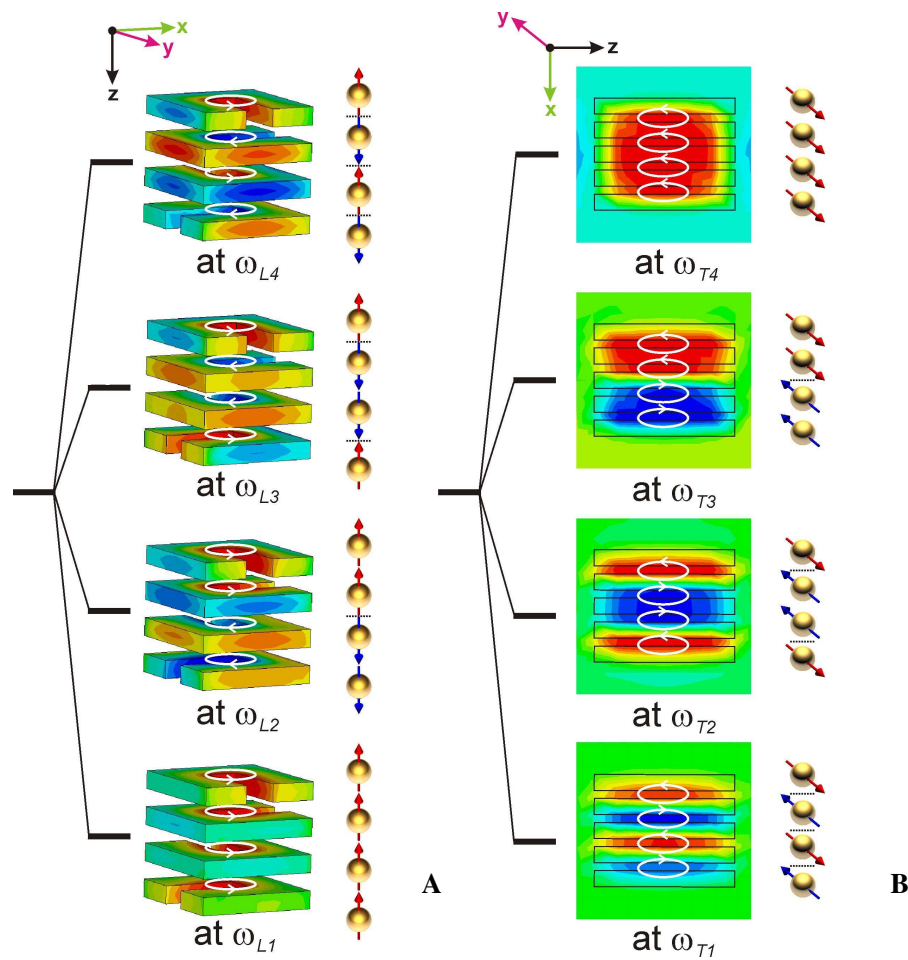


Figure 5.14: (A) Resonance diagram depicting the hybridization of the modes for the 4-layer twisted SRR metamaterial and the simulated magnetic field distributions of H_z at the corresponding resonance frequencies. (B) Resonance diagram depicting the hybridization of the modes for the 5-layer fishnet metamaterial and the simulated magnetic field distributions of H_y at the corresponding resonance frequencies. Red color denotes a positive H-field, and blue denotes a negative H-field. The “spin” symbols represent the magnetic dipole moments for the respective modes. The fully parallel and antiparallel alignments of “spins” correspond to the lowest frequency resonance in (A) and (B), respectively. The number of magnetic field nodes (dotted lines) is rising and declining in (A) and (B), respectively, for increasing resonance frequencies.

Through side-by-side arrangement, these magnetic dipoles can also be coupled transversely. Fig. 5.12B presents the schematic of a 5-layer fishnet metamaterial. The gold fishnet layers are surrounded by air, and the wire widths in both directions are designed to be equal for polarization independence. As has been intensively studied for the 2-layer fishnet structures, the incident light field can induce a magnetic resonance, which is correlated with the excitation of a magnetic dipole moment arising from the anti-phase current oscillation in the two metal layers [4, 56]. Intuitively, with increasing number of fishnet layers, the resonant behavior of the stacked systems would become rather complex due to the interaction between neighboring layers. To substantiate this expectation, numerical simulations were performed for the stacked fishnet metamaterial. The simulated transmission spectrum is shown in Fig. 5.13B, in which four resonances are clearly evident (ω_{T1} , ω_{T2} , ω_{T3} , and ω_{T4}). Additionally, large enhancement of the localized magnetic field at the corresponding resonances is observed by detecting the amplitudes of the magnetic field H_y via a probe placed inside the gap between the top two gold wires. In order to highlight the physical mechanism of the magnetic responses, the magnetic field distributions at the respective resonances are illustrated in Fig. 5.14B. Each resonance is associated with the excitation of magnetic dipole moments inside the four gaps

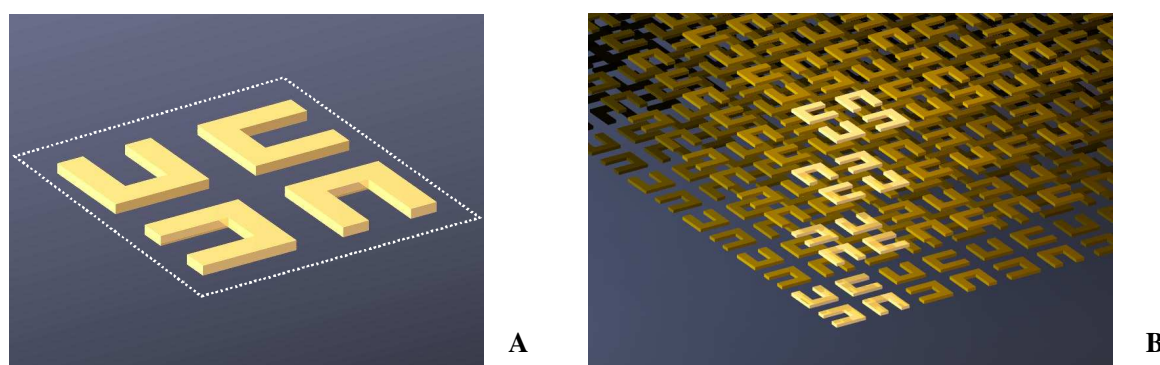


Figure 5.15: (A) A unit cell of a two-dimensional magnetic metamaterial. (B) A hypothetical three-dimensional magnetic (“spin”) metamaterial. Each layer consists of SRRs that are twisted by 90° compared to its vertical neighbor layers.

between each gold wire pair. The resonant behavior of the stacked fishnet system can be understood by the hybridization of magnetic response as well. The incident light excites a current loop in each wire pair and thus results in a magnetic dipole moment. These magnetic

dipoles are *transversely* coupled and leads to the formation of four new hybridized modes, which are associated with different symmetries. More specifically, at the lowest frequency resonance ω_{T1} , the four magnetic dipoles tend to align fully antiparallel. The intermediate resonances ω_{T2} and ω_{T3} are incomplete antiparallel arrangements of the magnetic dipoles, whereas at resonance ω_{T4} the four magnetic dipoles are aligned fully parallel. A diagram depicting the interaction between these transversely coupled magnetic dipoles and the resulting hybridized modes is shown in Fig. 5.14B.

Consequently, we are going to combine the concepts of longitudinal and transverse coupling, arranging metamaterial magnetic dipoles in three dimensions. In our design, the combination of longitudinal and transverse coupling is unique in the sense that it allows for the study of purely magnetic dipole-dipole interaction in a metasolid in the lateral as well as in the vertical direction (as far as solely nearest neighbor interaction is considered). Fig. 5.15A shows a planar unit cell of such an element, consisting of four SRRs with 90° rotation angle relative to their neighbors. Longitudinal coupling as complication to the two-dimensional prototype can be introduced by stacking the planar building blocks subsequently with each layer twisted by 90° compared to its former layer. The coupling strengths of the longitudinal as well as the transverse coupling can be controlled by altering the lateral and vertical separations of constituent SRRs. Fig. 5.15B illustrates the three-dimensional arrangement of these SRRs, which constitutes a magnetic metasolid. We might term it as “photonic spin crystal”.

5.3.3 Summary

In conclusion, we have investigated longitudinal and transverse magnetic coupling in three-dimensional optical metamaterials [57]. Depending on end-to-end or side-by-side arrangement, the metamaterial magnetic dipoles can be longitudinally or transversely coupled, giving rise to fully parallel or fully antiparallel alignment of these artificial “spins” at the lowest frequency resonance. This would constitute superparamagnetism at optical frequencies. We should remark that by using Babinet’s principle [44, 45], our concepts can be applied to complimentary metamaterial structures with the polarization of the incident light rotated by 90° . Furthermore, our concepts can also be extended to more complex metamaterial systems, in

which both longitudinal and transverse magnetic interactions are involved. In the future, the challenge lies ahead to understand the rather complicated spectra of such magnetic systems and to examine the applicability of solid-state physics concepts to these novel materials.

6. Novel three-dimensional metamaterials

6.1 Stereometamaterials

6.1.1 Introduction

The subdiscipline of chemistry that studies molecular structures in three dimensions is called stereochemistry [58]. One important aspect of stereochemistry is stereoisomers: same chemical formula but different spatial arrangements of atoms within molecules. The relative positions of atoms have great influence on the properties of chemical substances. Here, in analogy to stereoisomers in chemistry, we propose a new concept in nanophotonics, namely *stereometamaterials*, which refer to metamaterials with same constituents but different ways these constituents are arranged in space. As model system of stereometamaterials, we theoretically and experimentally study meta-dimers, which consist of a stack of two identical split-ring resonators in each unit cell with various twist angles. The interplay of electric and magnetic interactions plays a crucial role for the optical properties. Specifically, the influence of higher-order electric multipoles becomes clearly evident. The twisting of stereometamaterials offers a way to engineer complex plasmonic nanostructures with a tailored electromagnetic response.

6.1.2 Experimental results

Fig. 6.1A illustrates the geometry of the stereo-SRR dimer metamaterials together with their design parameters. Each unit cell consists of two spatially separated SRRs, which are twisted at angle φ with respect to one another. The SRRs are embedded in a homogeneous dielectric with $\varepsilon = 1$, i.e., air. For excitation of these SRR dimer metamaterials, we utilize normally incident light with its polarization along the x -direction as shown in Fig. 6.1A. In order to

gain insight into the resonant behavior as well as coupling mechanisms for various stereo-SRR dimer metamaterials, we first study three specific dimer systems with twist angles: $\varphi = 0^\circ$, 90° , and 180° . The insets of Fig. 6.1, B to D present the schematics of the three

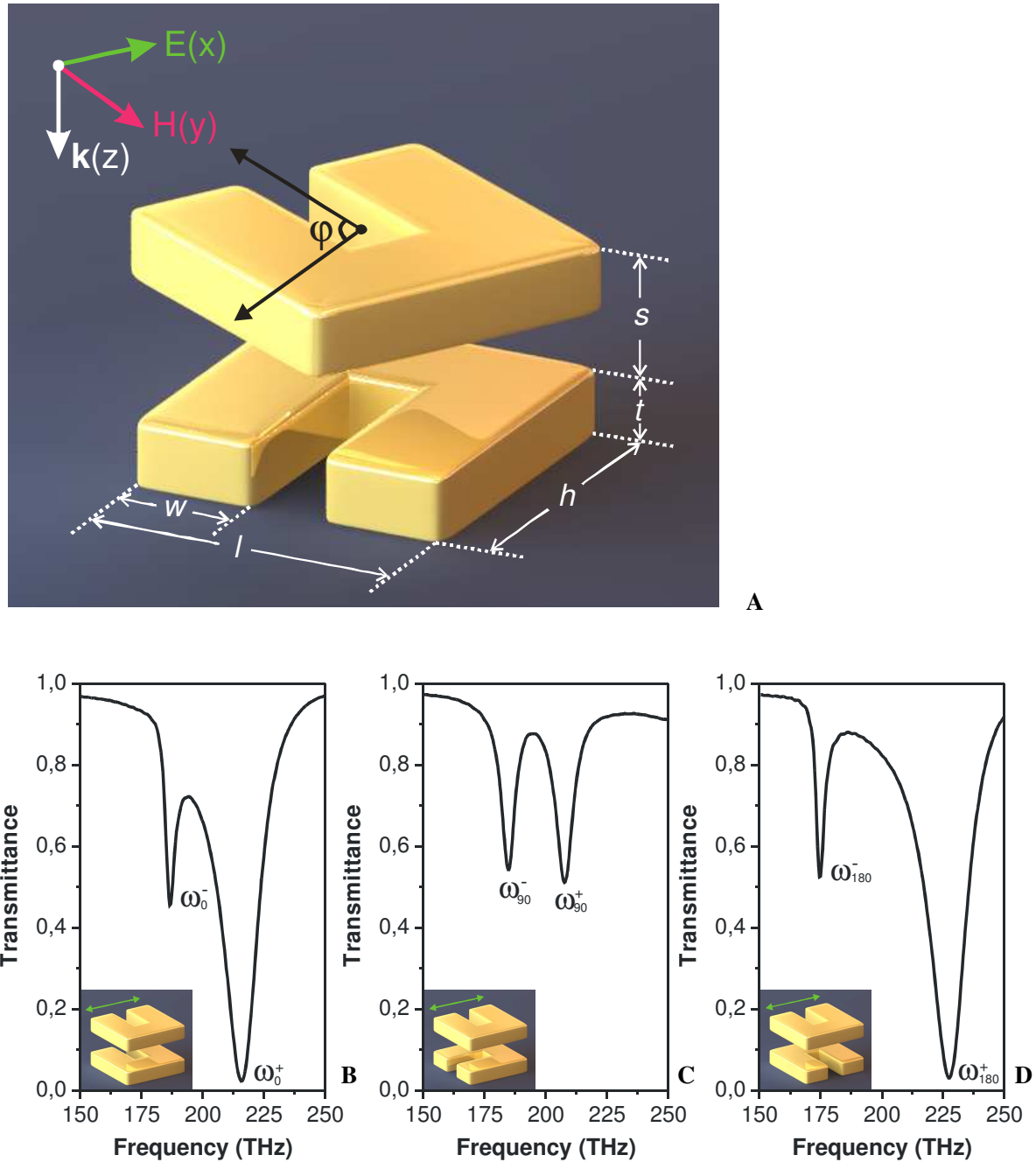
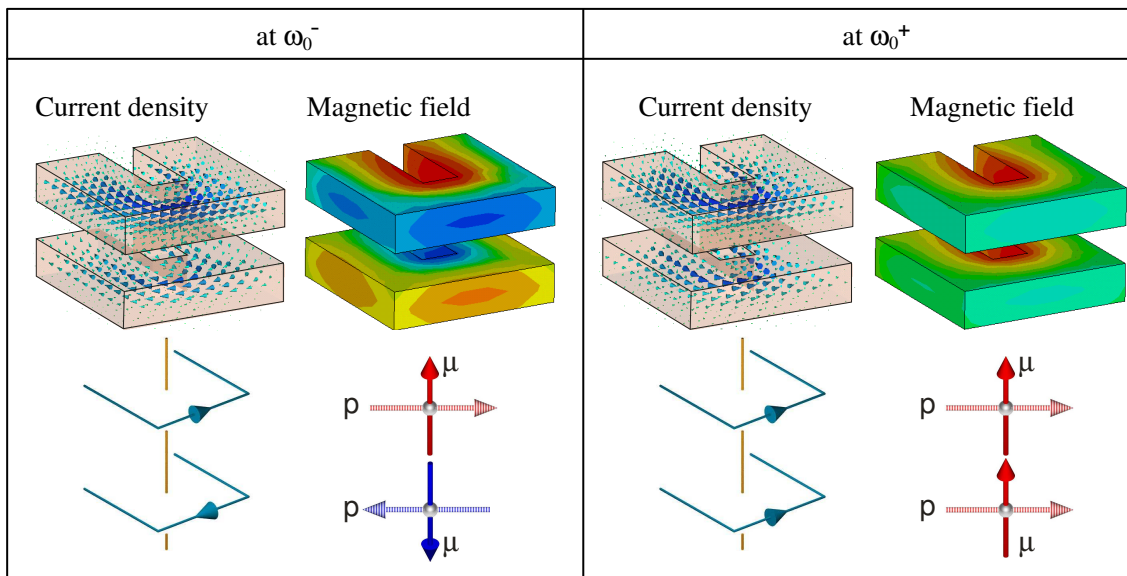


Figure 6.1: (A) Schematic diagram of the stereo-SRR dimer metamaterials with definitions of the geometrical parameters: $l = 230$ nm, $h = 230$ nm, $w = 90$ nm, $t = 50$ nm, and $s = 100$ nm. The periods in both x and y directions are 700 nm. Simulated transmittance spectra for the 0° (B), 90° (C), and 180° (D) twisted SRR dimer metamaterials. All the structures are embedded in air.

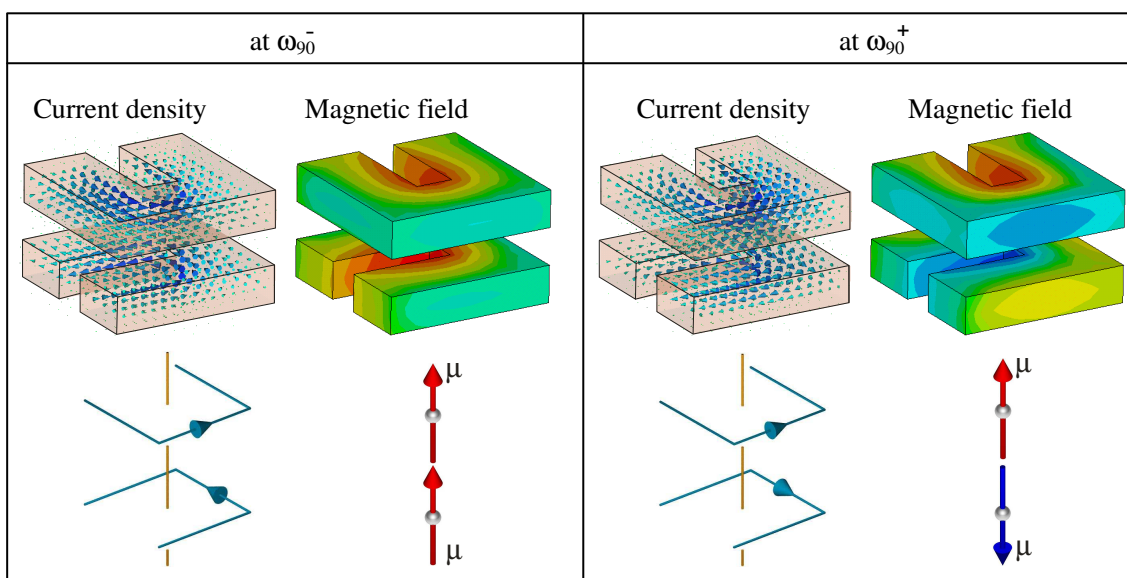
structures, in which the vertical distance between two SRRs is set at $s = 100$ nm. Numerical simulations were performed based on a commercial finite-integration time-domain algorithm, and the simulated transmittance spectra are shown in Fig. 6.1, B to D. Apparently, for each system there are two resonances (ω^- and ω^+) observable. In order to understand these spectral characteristics, current and magnetic field distributions at the relevant resonances are calculated. For the 0° twisted SRR dimer metamaterial, the electric component of the incident light can excite circulating currents along the two SRRs, giving rise to induced magnetic dipole moments in the individual SRRs. As shown in Fig. 6.2A, the electric dipoles excited in the two SRRs oscillate anti-phase and in-phase at resonances ω_0^- and ω_0^+ , respectively. The resulting magnetic dipoles are aligned antiparallel at resonance ω_0^- , whereas they are parallel at resonances ω_0^+ . The above phenomenon can be interpreted as the plasmon hybridization between the two SRRs due to their close proximity. In the hybridization scheme, each SRR can be regarded as an artificial ‘atom’. The two SRR ‘atoms’ are bonded into an SRR dimer or SRR ‘molecule’ due to the strong interaction between them. Such interaction leads to the formation of new plasmonic modes, arising from the hybridization of the original state of an individual SRR. For the configuration of the 0° twisted SRR dimer system, the two excited electric dipoles are transversely coupled, while the two magnetic dipoles are longitudinally coupled. In the case of transverse dipole-dipole interaction, the antisymmetric and symmetric modes are at the lower and higher resonance frequencies, respectively. In contrast, in the case of longitudinal dipole-dipole interaction, the two magnetic dipoles should align parallel at the lower resonance frequency and antiparallel at the higher resonance frequency [59]. It is evident that for the 0° twisted SRR dimer system (see Fig. 6.2A), the resonance levels are determined according to the picture of transverse electric dipole-dipole interaction, with the antisymmetric (symmetric) mode having the lower (higher) resonance frequency. In essence, the two coupling mechanisms, i.e., the electric and magnetic dipolar interactions, counteract one another and the electric interaction dominates in this system.

For the 90° twisted SRR dimer metamaterial, circular currents in the underlying SRR cannot be directly excited by the incident light owing to its orientation with respect to the external electric field. In a sense, the underlying SRR can be regarded as a ‘dark atom’ at the resonant frequency of the ring¹³. Nevertheless, for the coupled dimer system, on resonance,

A



B



C

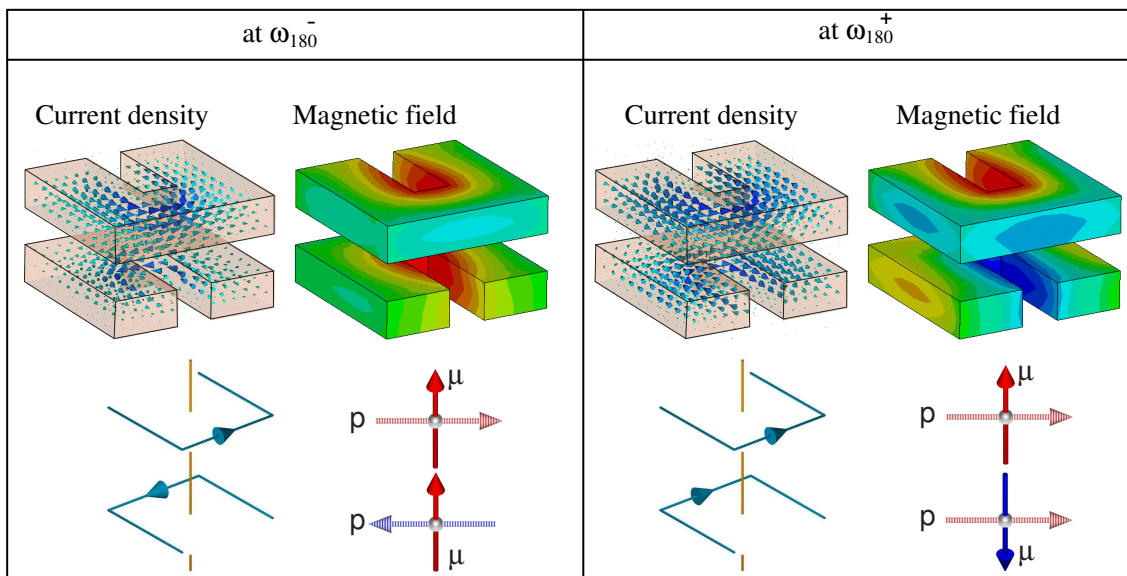


Figure 6.2: Current and magnetic field distributions at respective resonances for the 0° (A), 90° (B), and 180° (C) twisted SRR dimer metamaterials. Lower left side: schematic diagrams of current flows in two SRRs. Lower right side: schematic diagrams of the alignments of the magnetic and electric dipoles. Solid and dashed arrows represent magnetic and electric dipole moments, respectively. At 0° , transverse electric and longitudinal magnetic interactions work against one another, whereas at 180° they add together. At 90° , only longitudinal magnetic interaction is present.

excitation from the upper SRR can be transferred to the underlying one by the interaction between the two SRRs, which can lead to the formation of new plasmonic modes as well (ω_{90}^- and ω_{90}^+). Interestingly, because the electric fields in the slit gaps of the two SRRs are perpendicular to one another, the electric dipole-dipole interaction equals zero. In addition to the fact that the higher-order multipolar interaction is negligible in a first approximation, the electric coupling in the 90° twisted SRR dimer system can thus be ignored. As a consequence, the resonance levels are determined in line with the picture of longitudinal magnetic dipole-dipole coupling. As shown in Fig. 6.2B, at resonances ω_{90}^- and ω_{90}^+ , the resulting magnetic dipoles in the two SRRs are aligned parallel and antiparallel, respectively.

For the 180° twisted SRR dimer metamaterial, the interaction between the two SRRs results in new plasmonic modes, ω_{180}^- and ω_{180}^+ . Notably from the current and magnetic field distributions as shown in Fig. 6.2C, resonances ω_{180}^- and ω_{180}^+ are associated with the excitation of the electric dipoles in the two SRRs oscillating anti-phase and in-phase, respectively. The two resulting magnetic dipoles are aligned parallel and antiparallel, accordingly. In essence, the transverse electric and longitudinal magnetic interactions contribute positively in the 180° twisted SRR dimer system. This leads to the largest spectral splitting, which is a direct indication of the coupling strength. Based on the above discussions, we infer that the optical properties of stereometamaterials depend dramatically on the spatial arrangement of metamaterial constituents. Specifically, the possibility of tuning the resonant behavior by simply varying the relative twist angles makes stereometamaterials particularly interesting as model systems for exploring and comprehending different coupling mechanisms in complex 3D plasmonic structures.

In order to provide deeper insight, the optical properties of the stereo-SRR dimer metamaterials in dependence of twist angles are investigated. Fig. 6.3 presents the simulated twisting dispersion curves (in black squares) of these stereometamaterials, in which the

resonance positions are extracted from the transmittance spectra of different structures. It is apparent that by increasing the twist angle φ , the two resonance branches first tend to converge, with the ω^+ branch shifting to lower frequencies, while the ω^- branch shifts to higher frequencies. An avoided crossing is observed at φ_t , which is around 60° . Subsequently, the two branches shift away from one another. In order to clarify the underlying physics of the twisting dispersion curves, we introduce a Lagrangian formalism [36]. We start from the analysis of a single SRR and then expand it to coupled stereo-SRR dimer systems. One SRR can be modelled by an equivalent LC circuit with a resonance frequency $\omega_f = 1/(LC)^{1/2}$. It consists of a magnetic coil (the metal ring) with inductance L and a capacitor (the slit of the ring) with capacitance C . If we define the total charge Q accumulated in the slit as a generalized coordinate, the Lagrangian of an SRR can be written as $\Gamma = L\dot{Q}^2/2 - Q^2/2C$. Here $L\dot{Q}^2/2$ refers to the kinetic energy of the oscillations, and $Q^2/2C$ is the electrostatic energy stored in the slit. Consequently, the Lagrangian of the coupled SRR dimer systems is a combination of two individual SRRs with the additional electric and magnetic interaction terms:

$$\Gamma = \frac{L}{2}(\dot{Q}_1^2 - \omega_f^2 Q_1^2) + \frac{L}{2}(\dot{Q}_2^2 - \omega_f^2 Q_2^2) + M_H \dot{Q}_1 \dot{Q}_2 - M_E \omega_f^2 Q_1 Q_2 \cdot (\cos \varphi - \alpha \cdot (\cos \varphi)^2 + \beta \cdot (\cos \varphi)^3) \quad (6.1)$$

Here, Q_1 and Q_2 are oscillating charges in the respective SRRs, and M_H and M_E are the mutual inductances for magnetic and electric interactions, respectively. Apart from the electric dipole-dipole interaction, the contributions from the higher-order electric multipolar interactions are also included. α and β are the coefficients of the quadrupolar and octupolar plamon interactions [60], respectively. They serve as correction terms to the electric dipolar interaction. It is straightforward to derive from equation (6.1) that the major interaction items for 0° and 180° cases are $M_H \dot{Q}_1 \dot{Q}_2 - M_E \omega_f^2 Q_1 Q_2$ and $M_H \dot{Q}_1 \dot{Q}_2 + M_E \omega_f^2 Q_1 Q_2$, respectively. It is in accord with the above simulation results that the magnetic and electric interactions contribute oppositely and positively for 0° and 180° twisted SRR dimer metamaterials, respectively. For the 90° twisted SRR dimer metamaterial, only the magnetic

interaction plays a key role, as represented by the interaction term $M_H \dot{Q}_1 \dot{Q}_2$. Subsequently, by solving the Euler-Lagrange equations

$$\frac{d}{dt} \left(\frac{\partial \Gamma}{\partial \dot{Q}_i} \right) - \frac{\partial \Gamma}{\partial Q_i} = 0, \quad (i=1,2), \quad (6.2)$$

the eigenfrequencies of these stereo-SRR dimer systems can be obtained as

$$\omega_{\pm} = \omega_0 \cdot \sqrt{\frac{1 \mp \kappa_E \cdot (\cos \varphi - \alpha \cdot (\cos \varphi)^2 + \beta \cdot (\cos \varphi)^3)}{1 \mp \kappa_H}}, \quad (6.3)$$

where $\kappa_E = M_E / L$ and $\kappa_H = M_H / L$ are the coefficients of the overall electric and magnetic interactions, respectively. By fitting the twisting dispersion curves, the corresponding coefficients are estimated to be $\kappa_E = 0.14$, $\kappa_H = 0.09$, $\alpha = 0.8$, and $\beta = -0.4$. Notably from Fig. 6.3, the fitting curves (in red lines) reproduce the numerical data quite well and the avoided crossing is clearly observable at around 60° . This elucidates that the Lagrangian model can quantitatively corroborate the results from the numerical simulations. It is of crucial importance that the higher-order electric multipolar interactions account for the existence of the avoided crossing. Due to the finite length of the SRR ring, discrete electric plasmon modes characterized by different spatial symmetries can be excited by the incident light. The surface charges in the SRR ring are a superposition of such fundamental plasmon modes of the ring [60]. To reveal the significant role of the higher-order electric multipolar interactions, the grey lines in Fig. 6.3 display the twisting dispersion curves, in which only the dipolar coupling effect is taken into account, i.e., $\alpha = 0$ and $\beta = 0$. The best fit is achieved with $\kappa_E = 0.2$ and $\kappa_H = 0.09$. Obviously, despite the fact that the grey curves can fit most parts of the numerical data, no avoided crossing is predicted. Instead, the ω^+ and ω^- branches converge at φ_i . Therefore, it has to be emphasized that although the electric and magnetic dipolar interactions are the essential mechanisms, the higher-order electric multipolar interactions should also be carefully considered for fully understanding the origin of the spectral characteristics of the stereometamaterial systems.

The angle where the avoided crossing occurs in the twisting dispersion spectrum is

correlated with the geometry of the SRRs as well as the vertical distance between the two SRRs. For the specific stereo-SRR dimer metamaterials we investigated here, the avoided crossing appears at around 60° . Based on detailed simulated field distribution studies, we found that this angle is also a transition angle where the higher and lower frequency modes

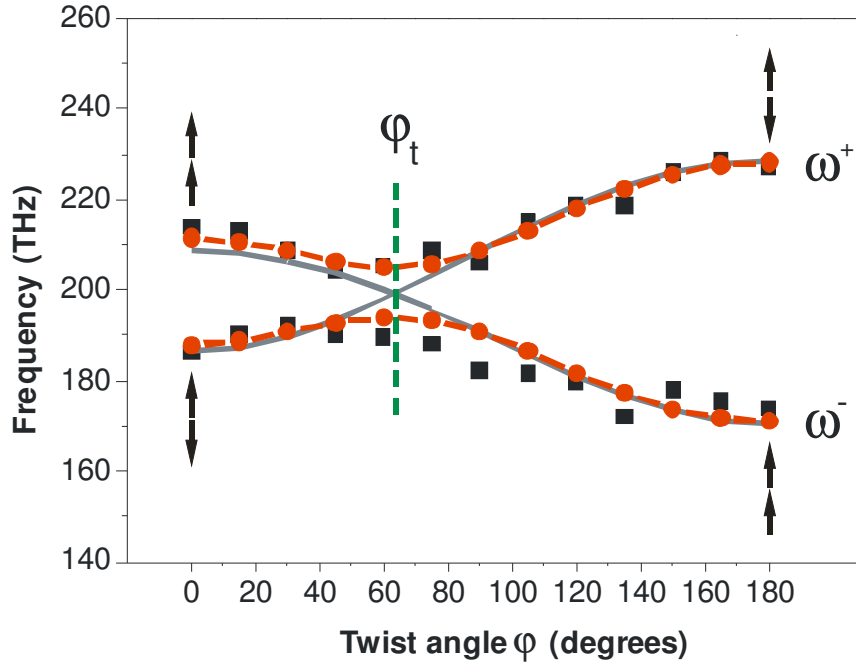


Figure 6.3: Twisting dispersion of the stereo-SRR dimer metamaterials. Black dots represent the numerical data. Red lines represent the fitting curves calculated from the Lagrangian model, in which the avoided crossing is clearly visible at φ . The black arrows represent the alignment of the magnetic dipoles at lower and higher resonance frequencies at twist angle $\varphi = 0^\circ$ and 180° . The grey lines represent the fitting curves calculated from the Lagrangian model *without* considering the higher-order electric multipolar interactions. No avoided crossing is observable in this case.

exchange their magnetic dipole alignments from parallel to antiparallel. More concretely, at angles smaller than angle φ_t , the two magnetic dipoles are aligned parallel (antiparallel) at resonance ω^+ (ω^-). The electric coupling effect dominates in this regime. With continuous increase of the twist angle, due to the displacement of the two SRRs, the electric coupling contributes less effectively. Consequently, the splitting of the two resonance branches start to decrease. This situation remains until the transition angle is reached, where the electric and magnetic dipole-dipole interactions cancel one another. The higher-order electric multipolar interactions account for the avoided crossing of the two resonance branches. After angle φ_t , the electric coupling continues to decrease. As a result, the resonance levels are determined

according to the scheme of magnetic dipole-dipole coupling, i.e., the parallel and antiparallel alignments of the magnetic dipoles in the two SRRs correspond to the lower and higher frequency resonances, respectively. When the twist angle reaches 90° , the electric coupling quenches and is negligible. This represents a purely magnetic dipole-dipole coupling situation. Subsequently, with further increase of the twist angle, the displacement of the two SRRs is reduced and the electric coupling comes into play again. Due to the orientation of the two SRRs, the electric and magnetic coupling can contribute positively, giving rise to a larger splitting of the two resonance branches with increasing twist angle. Finally, the splitting reaches its maximum at $\varphi = 180^\circ$.

The structures of stereometamaterials are compatible with nanofabrication stacking techniques [26]. We fabricated three stereo-SRR dimer metamaterials with specific twist angles $\varphi = 0^\circ$, 90° , and 180° , as illustrated in the insets of Fig. 6.1, B to D. In experiment, the structures were fabricated on a glass substrate. The SRRs were embedded in a photopolymer (PC403), which serves as the dielectric spacer. A spacer of $s = 120$ nm was applied in order to achieve surface planarization for stacking the second SRR layer. The electron micrographs of the fabricated SRR dimer metamaterials were obtained by field emission scanning electron microscopy. Figs. 6.4A, B, and C present oblique views of the 0° , 90° , and 180° twisted SRR dimer metamaterials, in which the underlying SRRs are clearly visible. The insets of Figs. 6.4A, B, and C show the normal views, demonstrating the good lateral alignment accuracy between different SRR layers. To experimentally investigate the optical properties of these SRR dimer metamaterials, the near-infrared transmittance spectra of the samples at normal incidence were measured by a Fourier-transform infrared spectrometer with electric field polarization as illustrated in Fig. 6.1. The measured transmittance spectra are presented by black curves in Figs. 6.4D, E, and F. The simulated spectra are plotted as red dashed curves in the same figures. The resonance positions are red-shifted compared to those of the corresponding resonances in Fig. 6.1 B to D due to the presence of glass substrate and dielectric spacers. For a reasonable comparison with the experiment, in the simulations in Fig. 6.4, D to F, gold with a three times higher damping constant as that used in Fig. 6.1, B to D, is employed to account for the surface scattering and grain boundary effects in the thin film of the real systems [47]. The overall qualitative agreement between experimental and simulated

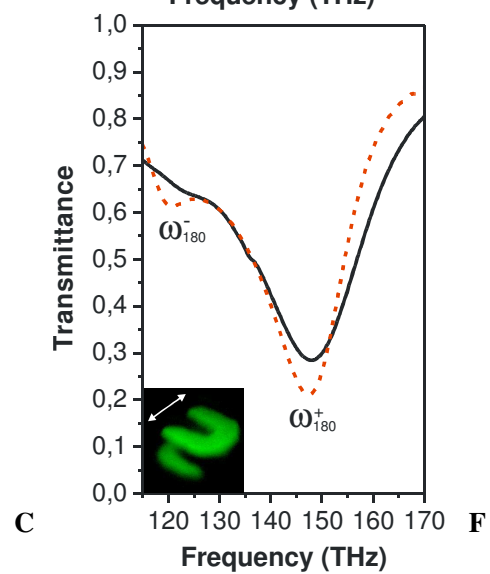
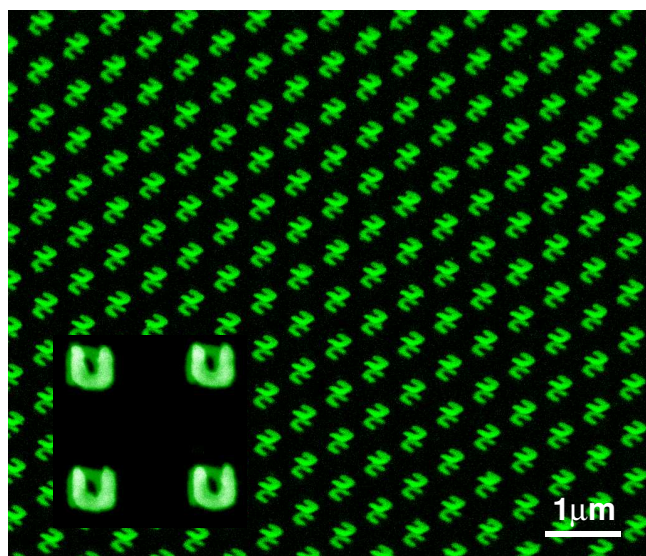
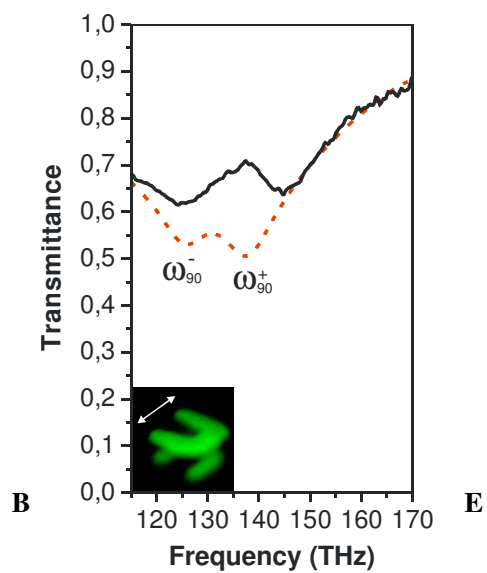
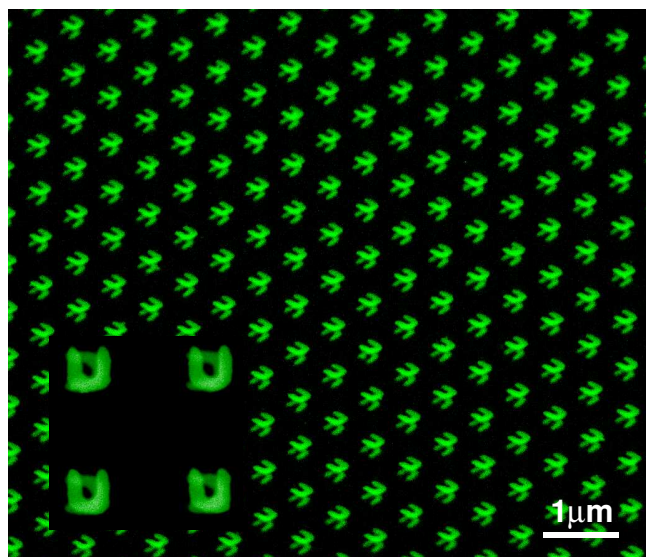
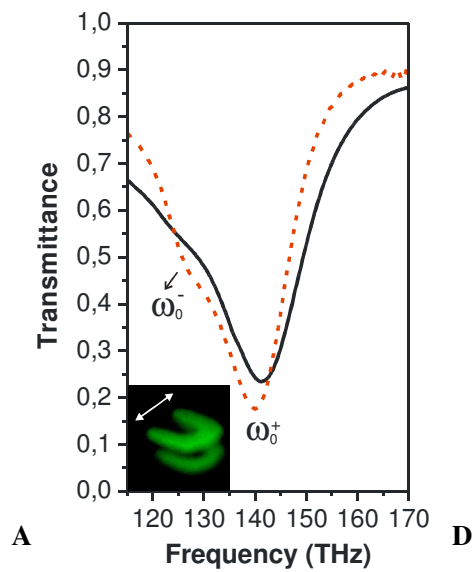
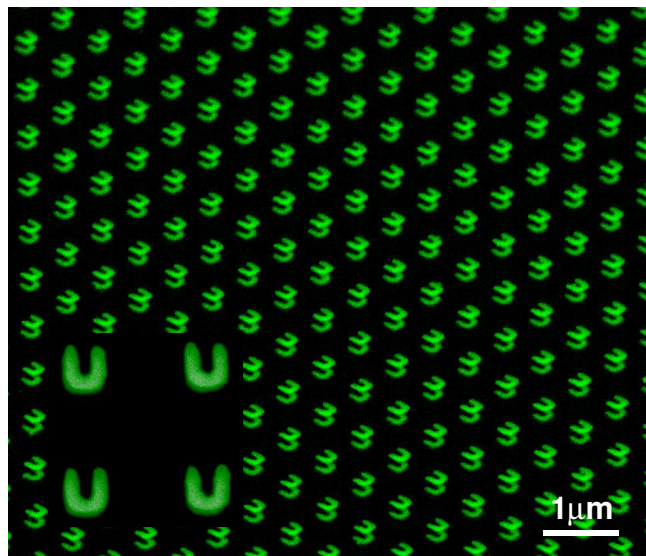


Figure 6.4: Field-emission electron microscopy images and experimental measurement. Oblique views of the 0° (A), 90° (B), and 180° (C) twisted SRR dimer metamaterials. Insets: Normal views. The structures were fabricated on a glass substrate. The SRRs were embedded in a photopolymer (PC403), which serves as the dielectric spacer. Experimental transmittance spectra for the 0° (D), 90° (E), and 180° (F) twisted SRR dimer metamaterials. The black and red curves represent the experimental and simulated results, respectively. For the 90° twisted SRR dimer structure, an analyzer is applied behind the sample, which is rotated by 75° with respect to the polarization of the incident light.

results is quite good. The discrepancies are most likely due to tolerances in the fabrication and assembly, as well as the significant broadening in the experiment. For 0° and 180° twisted SRR dimer structures, the lower resonances ω_0^- and ω_{180}^- are less distinctly visible than the higher resonances ω_0^+ and ω_{180}^+ , respectively, in the spectra as shown in Fig. 6.4D and 4F. This is due to the fact that for both dimer structures, the electric coupling plays a key role. At the lower resonance frequencies (ω_0^- and ω_{180}^-), the electric dipoles in the two SRRs oscillate anti-phase. Such resonances are not easily excited by light. On the other hand, at the higher resonance frequencies (ω_0^+ and ω_{180}^+), the electric dipoles in the two SRRs oscillate in-phase. Such resonances can strongly couple to light. For the 90° twisted SRR dimer structure, the splitting of the resonances is clearly observable when an analyzer is applied behind the sample, which is rotated by 75° with respect to the polarization of the incident light. This is due to the polarization rotation effect arising from the chirality [61] of the 90° twisted structure.

6.1.3 Summary

The new concept of stereometamaterials [62] adds a significant degree of freedom through the interplay of electric and magnetic interactions, and tremendously enhances the versatility of nanophotonic structures. Stereometamaterials allow us to utilize higher-order electric multipolar as well as magnetic interaction, which can be nearly as large as the electric dipolar interaction. This is completely different from molecules, where electric dipolar interaction is the essential contribution for the optical properties. It will also be interesting to study the geometry and distance dependence of the different coupling effects. Our concept can be

extended to more complex artificial molecules, such as stereo-trimers, stereo-quadrimers, and so on. The tunability of the resonant behavior of these new artificial materials by altering the spatial arrangement of their constituents offers great flexibility for exploring useful metamaterial applications, such as chiral structures with negative refraction [40], invisibility cloaks [12], and magneto-optically active materials [63]. Stereometamaterials open the avenue towards optical polarization control, which so far has been dominated by stereoisomers and liquid crystals [64]. More information on optical stereoisomers as well as left- and right-handed enantiomers can be found in the Supplementary Information. Stereometamaterials might also serve as artificial nano-systems to emulate the optical properties of complex biomolecules, such as double helix DNA chiral proteins and drug enzymes, which have profound application potentials in biophotonics, pharmacology, as well as diagnostics.

6.2 Plasmonic electromagnetically induced transparency in metamaterials

6.2.1 Introduction

In atomic physics, the coherent coupling of a broad and a narrow resonance leads to quantum interference and provides the general recipe for electromagnetically induced transparency (EIT) [23, 65, 66]. A sharp resonance of nearly perfect transmission can arise within a broad absorption profile. These features show remarkable potential for slow light [67-69], novel sensors, and low-loss metamaterials. In nanophotonics, plasmonic structures enable large field strengths within small mode volumes. Therefore, combining EIT with nanoplasmonics would pave the way towards ultracompact sensors with extremely high sensitivity. Here we experimentally demonstrate a nanoplasmonic analog of EIT utilizing a stacked optical metamaterial. A dipole antenna with a large radiatively broadened linewidth is coupled to an underlying quadrupole antenna, whose narrow linewidth is solely limited by the fundamental nonradiative Drude damping. In accordance with EIT theory we achieve a very narrow transparency window with high modulation depth due to nearly complete suppression of radiative losses.

6.2.2 Experimental results

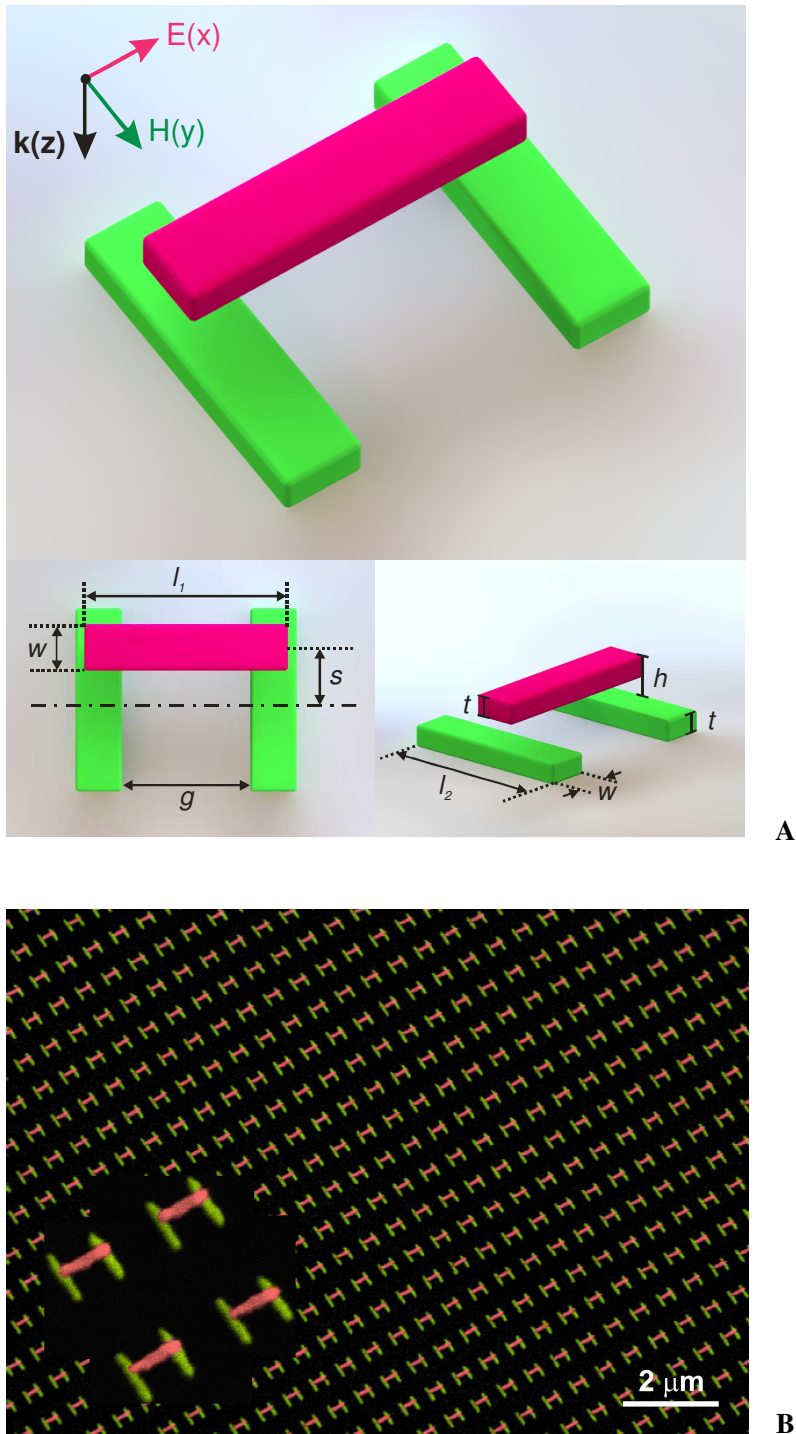


Figure 6.5: (A) Schematic diagram of the stacked plasmonic EIT structure with definitions of the geometrical parameters: $l_1 = 355 \text{ nm}$, $l_2 = 315 \text{ nm}$, $w = 80 \text{ nm}$, $g = 220 \text{ nm}$, $t = 40 \text{ nm}$, and $h = 70 \text{ nm}$. The periods in both x and y directions are 700 nm . Red color represents the gold bar in the top layer and green color represents the gold wire pair in the bottom layer. (B) Oblique view of the sample with lateral displacement $s = 10 \text{ nm}$. Inset: Enlarged view. All the structures were fabricated on a glass substrate. The gold wires were embedded in a photopolymer (PC403), which serves as dielectric spacer.

Fig. 6.5A schematically shows the metamaterial structure. The upper gold bar (in red) is stacked above the underlying gold wire pair (in green) with a vertical distance $h = 70$ nm. The lateral displacement of the bar with respect to the symmetry axis of the wire pair is defined as s . Electron micrographs of the samples fabricated by nanofabrication stacking techniques were obtained by field-emission scanning electron microscopy. Fig. 6.5B shows an oblique incidence overview of a typical sample with a lateral displacement $s = 10$ nm. An enlarged oblique view is given in the inset of Fig. 6.5B, demonstrating excellent alignment accuracy between the two functional layers. The optical properties of the samples at normal incidence were measured with a Fourier-transform infrared spectrometer with electric field polarization along the dipole antenna. In the following, we are going to show systematic tuning of the EIT-like spectra in these stacked samples by introducing structural asymmetry. The experimental transmittance (green circles), reflectance (pink circles), and absorbance spectra (black circles) in dependence on the lateral displacement s are presented in Fig. 6.6. The absorbance spectra were calculated using $A = 1 - T - R$. In the absence of structural asymmetry, i.e., for $s = 0$, there is only a single resonance ($\omega_0 = 170$ THz) observable in the absorbance spectrum (see Fig. 6.6B). The origin of this resonance is attributed to the excitation of dipole-like plasmons inside the upper gold bar. This gold bar works as a dipole antenna and radiates strongly to free space, giving rise to a broad resonance in the spectrum. The lower wires do not contribute, as the elements in the two layers are not coupled to each other in the absence of symmetry breaking.

The coupling between the two layers starts once the structural asymmetry is introduced. As visible in the case of $s = 10$ nm, a transmittance peak in Fig. 6.6A (an absorbance dip in Fig. 6.6B) at around 173 THz emerges near the center of the broad resonance. A detuning parameter δ is introduced to define the frequency difference between the quadrupole and dipole resonances. In our case, δ is approximately 3 THz, resulting from slightly too short bottom wires due to the fabrication process. By further enlarging the lateral displacement s , the coupling strength between the dipole and quadrupole antennas is successively increased. As a result, the transparency window at 173 THz grows in strength and becomes more and more prominent as shown in Fig. 6.6A. We interpret the above phenomena in terms of plasmonic EIT. Particularly, the narrow linewidths and high modulation depths of these

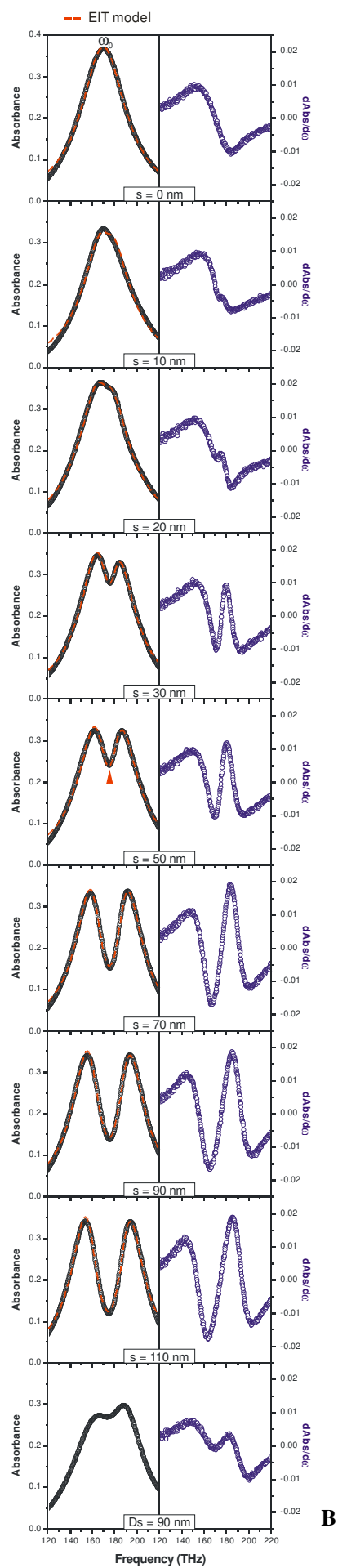
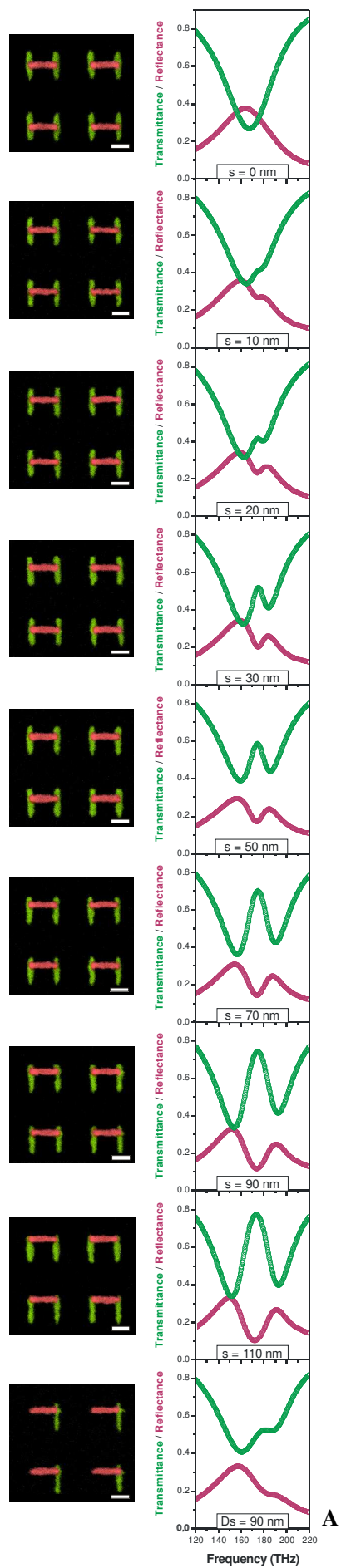


Figure 6.6: (A) SEM images of the corresponding structures are shown in the left column. The scale bar is 200 nm. Green and pink-circled curves represent the experimental transmittance and reflectance spectra, respectively. (B) Black-circled curves represent the experimental absorbance spectra ($A = 1 - T - R$). Red-dashed lines represent the fitting curves calculated from the two-oscillator model. The blue-circled curves represent the derivatives $dAbs/d\omega$ of the experimental absorbance spectra. The evolution of the EIT-like features in the absorbance spectra and their slopes show a strong dependence on the lateral displacement. The lowest spectrum shows the situation for two stacked dipole antennas, which are associated with normal-mode splitting rather than EIT. The remarkable difference between EIT-like behavior and normal-mode splitting can be nicely distinguished when comparing the two cases of $s = 90$ nm (third lowest spectrum, dipole-quadrupole coupling) and $Ds = 90$ nm (lowest spectrum, dipole-dipole coupling) in the figure. The normal-mode splitting case shows only a slight dip in the absorbance spectrum.

EIT-like features indicate the drastically low loss in the quadrupole antenna. The physics of the plasmonic EIT can be better understood if we examine the analogy between our system and atomic EIT systems [70]. Fig. 6.7A depicts a prototype three-level system for EIT, in which $|0\rangle$ is the ground state and $|1\rangle$ and $|2\rangle$ are the two upper states. $|0\rangle$ - $|1\rangle$ defines a dipole-allowed transition, which is in analogy to the mode excited in the dipole antenna in our system. It is related to a photon frequency ω_0 and a dissipation rate γ_1 . This rate includes two contributions, namely, radiative damping due to the transformation of particle plasmons into photons and nonradiative damping due to the intrinsic metal loss. $|0\rangle$ - $|2\rangle$ defines a dipole-forbidden transition, which is in analogy to the mode that can be excited in the quadrupole antenna when structural asymmetry is present. It is characterized by a dissipation rate γ_2 , which is mainly limited by the intrinsic metal loss. δ denotes the detuning from the transition line center with the condition $\delta \ll \gamma_1$. The two damping factors satisfy $\gamma_2 \ll \gamma_1 \ll \omega_0$. κ is the transition rate between states $|1\rangle$ and $|2\rangle$, correlated with the coupling between the dipole and quadrupole antennas. Consequently, the two possible pathways, namely, $|0\rangle$ - $|1\rangle$ and $|0\rangle$ - $|1\rangle$ - $|2\rangle$ - $|1\rangle$ interfere destructively, therefore dramatically reducing losses and enhancing transmittance.

In order to further explore the EIT-like spectral characteristics, optical spectra and the electric field distribution are calculated based on a scattering matrix algorithm and on commercial finite-integration time-domain software. For bulk gold, the permittivity in the infrared spectral regime is described by the Drude model [28, 71] with the plasmon frequency $\omega_{pl} = 2\pi \times 2.175 \times 10^{15} \text{ s}^{-1}$ and the damping constant $\omega_c = 2\pi \times 6.5 \times 10^{12} \text{ s}^{-1}$. Owing to the

surface scattering and grain boundary effects in the thin film, in the calculations we use a damping constant which is three times [47] as large as that in bulk gold, i.e., about 20 THz. The overall agreement between experimental and calculated spectra is very good (see Supporting Information). The electric field distribution at the absorbance dip as indicated by the red triangle in the case of $s = 50$ nm (see Fig. 6.6B) is shown in Fig. 6.7B. At resonance the two underlying wires are characterized by antisymmetric charge oscillations, which correspond to the excitation of the quadrupole mode. The destructive interference leads to a nearly zero electric field in the top bar. In other words, due to nearly complete suppression of radiative damping, the linewidth of these EIT-like features is solely limited by nonradiative damping, i.e., intrinsic Drude loss of the metal. This makes our plasmonic EIT structures particularly promising for biomedical and chemical sensing.

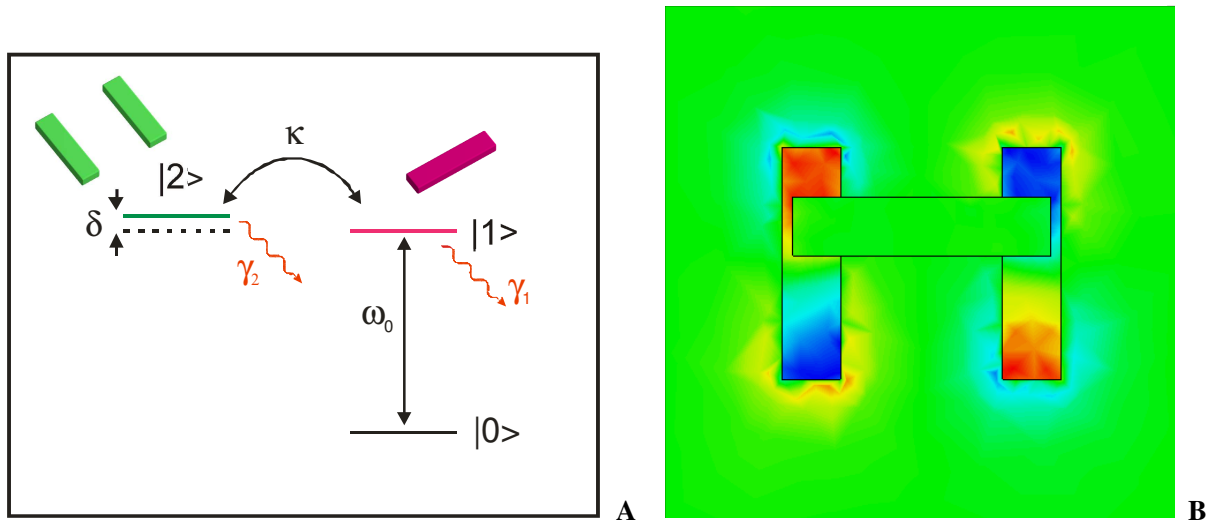


Figure 6.7: Prototype system for plasmonic EIT and numerical electric field distribution. (A) Level scheme for EIT in a prototype three-level system. δ denotes the detuning from the transition line center. κ defines the transition rate between states $|1\rangle$ and $|2\rangle$. γ_1 includes nonradiative damping due to the intrinsic metal loss, and radiative damping due to the strong dipole characteristics. γ_2 contains only nonradiative (Drude) damping. The two possible pathways, namely, $|0\rangle \rightarrow |1\rangle$ and $|0\rangle \rightarrow |1\rangle \rightarrow |2\rangle \rightarrow |1\rangle$ interfere destructively and lead to the EIT-like phenomena. (B) Electric field distribution at resonance as indicated by the red triangle for $s = 50$ nm in Fig. 6.6. Antisymmetric charge oscillations are excited in the bottom wire pair while the top bar contains nearly no field.

As a control experiment, we also fabricated a stacked sample with only a single wire, i.e., another dipole antenna, in the bottom layer. We define the lateral displacement of the top wire with respect to the symmetry axis of the bottom wire as D_s . Similarly, in the absence of

structural asymmetry, i.e., $Ds = 0$, the top and bottom wires are uncoupled, giving rise to a single absorbance peak in the spectrum (not shown). When structural asymmetry is introduced, i.e., $Ds = 90$ nm, the two dipole antennas can be coupled. Such dipole-dipole coupling between the two wires results in a spectral splitting due to the hybridization of the resonances of the two individual wires. It is worth mentioning that 90 nm was selected because lateral displacements below this value do not lead to observable spectral splitting in experiments. The difference between the EIT-like spectrum and the spectrum arising from hybridization of plasmonic modes is remarkable. This becomes evident when comparing the two corresponding spectra associated with the same lateral displacement, i.e., $s = 90$ nm and $Ds = 90$ nm in Fig. 6.6B. More concretely, the EIT-like spectrum exhibits a prominently narrow and pronounced absorbance dip resulting from destructive interference. On the contrary, in the case of the normal mode coupling, destructive interference is not expected due to the fact that the two dipole antennas have similar dampings. The occurrence of the tiny absorbance dip in the spectrum is due to the overlap of the two hybridized resonance envelopes.

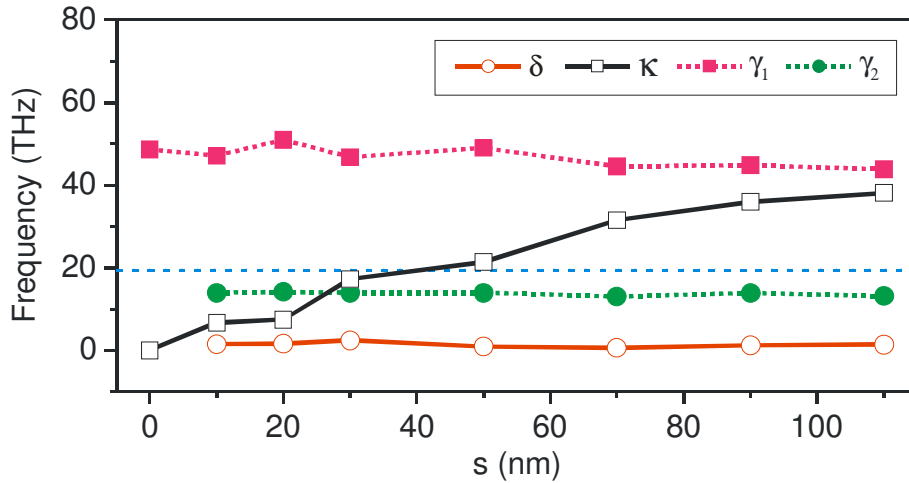


Figure 6.8: Extracted experimental damping and coupling parameters as a function of lateral displacement s . Values of γ_1 , γ_2 , δ , and κ extracted by fitting the experimental absorbance curves in Fig. 2b according to equation (3). The dashed-blue line represents the Drude damping limit of experimental thin gold films (~ 20 THz). Evidently, our extracted damping value of γ_2 is below this limit.

To evaluate our EIT-like spectra quantitatively, the derivatives $dAbs/d\omega$ of the experimental absorbance spectra are plotted in Fig. 6.6B, which are characterized by blue-circled curves. The evolution of the slopes of the EIT-like features in dependence on the lateral displacement

is apparently visible. Notably, the slopes of the EIT-like features are already steeper than those of the single plasmonic resonance ($s = 0$ nm) at $s = 50$ nm. Furthermore, as a maximum at $s = 90$ nm, a steepness ratio of 1.5 is achieved between the slopes of the EIT feature and plasmonic resonance. In contrast, for the dipole-dipole coupling case, the slopes of the absorbance dip are still flatter when compared to those of the single plasmonic resonance even at $s = 90$ nm.

In order to provide a quantitative description of our plasmonic EIT system, we employ a simple two-oscillator EIT model [66, 70]. The dipole antenna in our structure is represented by oscillator 1, which is driven by an applied source $E(t)$. The quadrupole antenna is represented by oscillator 2, which can only be excited through coupling between the two oscillators. The charges $q_1(t)$ and $q_2(t)$ in oscillators 1 and 2 satisfy the coupled differential equations:

$$\ddot{q}_1(t) + \gamma_1 \dot{q}_1(t) + \omega_0^2 q_1(t) + \kappa \dot{q}_2 = E(t) \quad (1)$$

$$\ddot{q}_2(t) + \gamma_2 \dot{q}_2(t) + (\omega_0 + \delta)^2 q_2(t) - \kappa \dot{q}_1 = 0 \quad (2)$$

Here ω_0 is the resonance frequency of oscillator 1 when it is isolated from oscillator 2. δ denotes the detuning of the resonance frequency of oscillator 2 from oscillator 1 ($\delta \ll \gamma_1$). γ_1 and γ_2 are the losses in oscillators 1 and 2, respectively ($\gamma_2 \ll \gamma_1 \ll \omega_0$). κ is the coefficient of the coupling between the two oscillators. After solving the equations with the approximation $\omega - \omega_0 \ll \omega_0$ and therefore $\omega_0^2 - \omega^2 \approx -2\omega_0(\omega - \omega_0)$, the energy dissipation as a function of frequency is obtained as follows:

$$P(\omega) = \frac{i}{2} \frac{(\omega - \omega_0 - \delta) + i \frac{\gamma_2}{2}}{(\omega - \omega_0 + i \frac{\gamma_1}{2})(\omega - \omega_0 - \delta + i \frac{\gamma_2}{2}) - \frac{\kappa^2}{4}} \quad (3)$$

Subsequently, we fit the experimental absorbance spectra in Fig. 6.6B according to equation (3) and present the results by red-dashed curves in the same figure for a direct comparison. It is evident that the experimental curves are reproduced nearly perfectly by the fitted results. In order to examine the damping mechanism, Fig. 6.8 shows the fitting values for γ_1 , γ_2 , δ , and κ

as a function of lateral displacement s in frequency unit. The detuning parameter δ is approximately 3 THz. The coupling coefficient κ is proportional to s and it increases successively with more structural asymmetry. γ_2 is roughly constant at 13 THz, which is nearly 4 times smaller than γ_1 (~ 50 THz). Such quantitative results substantiate our expectation on drastic reduction of losses in the quadrupole antenna due to nearly complete suppression of radiative coupling. It is noteworthy that the damping frequency correlated with the intrinsic loss in thin gold films in the near infrared is about 20 THz [4, 47] (see blue-dashed line in Fig. 6.8). Astonishingly, in our case γ_2 amounts to only 13 THz. This implies that the nonradiative damping in our system is also substantially reduced. The origin of this suppression of nonradiative damping becomes immediately apparent from the electric field distribution as shown in Fig. 6.7B. We found that at resonance a significant amount of the electric field is outside the gold wires and dissipates in the dielectric environment [72], which is the photopolymer PC403 (see Methods). Its dielectric losses are indeed negligible at optical frequencies. In essence, the damping in our plasmonic EIT system is below the Drude damping of thin gold films (20 THz) and even approaches the Drude damping limit of *bulk* gold (6.5 THz) [28, 71]. Such drastic reduction of damping leads to the extremely narrow linewidth of the quadrupole mode and hence greatly facilitates the plasmonic EIT effects.

6.2.3 Summary

The concept of plasmonic EIT provides deep insight into achieving low-loss optical metamaterials for future applications [73]. This arises from the fact that reducing losses is one of the major challenges in this field. In particular, the nonradiative damping could be further reduced by careful tailoring of the electric field inside and outside of the quadrupole antenna. Another benefit afforded by our plasmonic EIT analog is the ability to construct light-slowing devices [74, 75]. The realization of dipole-quadrupole coupling holds great promise for designing and understanding complex plasmonic structures associated with higher-order multipolar interaction mechanisms [62]. Additionally, the narrow and fully modulated EIT-like features due to the extraordinary reduction of damping are exciting news for novel devices in the field of chemical and biomedical sensing.

7. Conclusions

In this thesis, the coupling effects of stacked optical metamaterials have been investigated both experimentally and theoretically. Before fabricating metamaterials, we have always optimized the structures by different simulation techniques for efficiency and comparison. We have introduced standard fabrication procedures for manufacturing multilayer optical metamaterials, which provides a general recipe for the implementation of thicker or even bulk metamaterials at optical frequencies in the future. All our metamaterial samples were measured by a Fourier-transformed infrared spectrometer.

The main part of this thesis deals with detailed investigations of the optical properties of stacked metamaterials with different geometries. We have demonstrated that the plasmon hybridization method, which is generally applied to describe electric interactions in complex metallic nanostructures, can also be used for understanding the magnetic interactions in stacked fishnet metamaterials. We have shown that the vertical interaction between metamaterial slabs can substantially change the optical properties of metamaterials and lead to new characteristic spectral features with increasing number of stacked layers. The effect of stacking is thus a key issue that needs to be carefully considered, especially when taking into account specific applications.

Moreover, we have proposed a new concept in plasmonics, namely stereometamaterials. Stereometamaterials allow us to utilize higher-order electric multipolar as well as magnetic interaction, which can be nearly as large as the electric dipolar interaction. This is completely different from molecules, where electric dipolar interaction is the essential contribution for the optical properties. Stereometamaterials might serve as artificial nano-systems to emulate the optical properties of complex biomolecules, such as double helix DNA chiral proteins and drug enzymes, which have profound application potentials in biophotonics, pharmacology, as well as diagnostics. We have also experimentally realized for the first time the plasmonic

analog of EIT effects in metamaterials. The possibility of accurately tuning plasmonic response by utilizing structural asymmetry makes our metamaterial structures particularly interesting as a model system for comprehending light-matter interaction phenomena.

Photonic metamaterials offer the possibility to obtain optical properties which do not occur in natural substances. Stacked optical metamaterials further enables novel resonant behavior that does not exist in 2D metamaterials. Future interesting tasks include the realization of low-loss negative refractive index materials as well as 3D chiral metamaterials in the optical frequency range using the presented stacking technique together with the investigation of coupling effects in these more complex systems. Additionally, optimization of EIT-like features is highly desirable for novel devices in the field of chemical and biomedical sensing.

Bibliography

- [1] R. A. Shelby, D. R. Smith, S. Schultz, *Science* **292**, 77 (2001).
- [2] D. R. Smith, J. B. Pendry, M. C. K. Wiltshire, *Science* **305**, 788 (2004).
- [3] S. Linden, C. Enkrich, M. Wegener, J. F. Zhou, T. Koschny, C. M. Soukoulis, *Science* **306**, 1351 (2004).
- [4] G. Dolling, C. Enkrich, M. Wegener, C. M. Soukoulis, S. Linden, *Science* **312**, 892 (2006).
- [5] V. G. Veselago, *Sov. Phys. Usp.* **10**, 509 (1968).
- [6] J. B. Pendry, A. J. Holden, D. J. Robbins, W. J. Stewart, *IEEE Trans. Microwave Theory Tech.* **47**, 2075 (1999).
- [7] J. B. Pendry, A. J. Holden, W. J. Stewart, I. Youngs, *Phys. Rev. Lett.* **76**, 4773 (1996).
- [8] D. R. Smith, W. J. Padilla, D. C. Vier, S. C. Nemat-Nasser, S. Schultz, *Phys. Rev. Lett.* **84**, 4184 (2000).
- [9] J. B. Pendry, *Phys. Rev. Lett.* **85**, 3966 (2000).
- [10] M. C. K. Wiltshire, J. B. Pendry, J. V. Hajnal, *J. Phys.: Condens. Matter* **18**, L315 (2006).
- [11] J. B. Pendry, D. Schurig, D. R. Smith, *Science* **312**, 1780 (2006).
- [12] D. Schurig, J. J. Mock, B. J. Justice, S. A. Cummer, J. B. Pendry, A. F. Starr, D. R. Smith, *Science* **314**, 977 (2006).
- [13] C. Enkrich, F. P. Willard, D. Gerthsen, J. F. Zhou, T. Koschny, C. M. Soukoulis, M. Wegener, S. Linden, *Adv. Mater.* **17**, 2547 (2005).
- [14] V. A. Podolskiy, A. K. Sarychev, V. M. Shalaev, *Opt. Express* **11**, 735 (2003).
- [15] G. Dolling, C. Enkrich, M. Wegener, J. F. Zhou, C. M. Soukoulis, S. Linden, *Opt. Lett.* **30**, 3198 (2005).
- [16] S. Zhang, W. J. Fan, K. J. Malloy, S. R. J. Brueck, N. C. Panoiu, R. M. Osgood, *Opt. Express* **13**, 4922 (2005).

- [17] M. H. Qi, *et al. Nature* **429**, 538 (2004).
- [18] G. Subramania, S. Y. Lin, *Appl. Phy. Lett.* **85**, 5037 (2004).
- [19] A. S. P. Chang, *et al. Opt. Express* **15**, 8428 (2007).
- [20] E. Prodan, C. Radloff, N. J. Halas, P. Nordlander, *Science* **302**, 419 (2003).
- [21] H. Wang, D. W. Brandl, F. Le, P. Nordlander, N. J. Halas, *Nano Lett.* **6**, 827 (2006).
- [22] E. Shamonina, V. A. Kalinin, K. H. Ringhofer, L. Solymar, *J. Appl. Phys.* **92**, 6252 (2002).
- [23] K. J. Boller, A. Imamoglu, S. E. Harris, *Phys. Rev. Lett.* **66**, 2593 (1991).
- [24] J. D. Jackson, in *Classical Electrodynamics*, John Wiley & Sons, 1975, Ch. 4, 9.
- [25] W. Demtroeder, in *Experimtnalphysik 2*, Springer-Lehrbuch, 1995, Ch.1.
- [26] N. Liu, *et al. Nature Mater.* **7**, 31 (2008).
- [27] CST GmbH, Germany. www.cst.de
- [28] M. A. Ordal, *et al. Appl. Opt.* **22**, 1099 (1983).
- [29] A. Christ, T. Zentgraf, S. G. Tikhodeev, N. A. Gippius, J. Kuhl, H. Giessen, *Phys. Rev. B* **74**, 155435 (2006).
- [30] S. Zhang, W. J. Fan, B. K. Minhas, A. Frauenglass, K. J. Malloy, S. R. J. Brueck, *Phys. Rev. Lett.* **94**, 037402 (2005).
- [31] P. Nordlander, E. Prodan, *Nano Lett.* **4**, 2209 (2004).
- [32] N. Liu, *et al. Adv. Mater.* **19**, 3528 (2007).
- [33] P. Atkins, R. Friedman, in *Molecular Quantum Mechanics*, 4th. ed., Oxford Univ. Press, 2005, Ch. 8.9.
- [34] G. Dolling, C. Enkrich, M. Wegener, C. M. Soukoulis, S. Linden, *Opt. Lett.* **31**, 1800 (2006).
- [35] T. Li, H. Liu, F. M. Wang, Z. G. Dong, S. N. Zhu, *Opt. Express* **14**, 11155 (2006).
- [36] H. Liu, D. A. Genov, D. M. Wu, Y. M. Liu, Z. W. Liu, C. Sun, S. N. Zhu, X. Zhang, *Phys. Rev. B.* **76**, 073101 (2007).
- [37] P. Atkins, J. D. Paula, in *Physical Chemistry*, 8th. ed., Oxford University Press, Oxford 2006, Ch.20.
- [38] D. R. Smith, S. Schultz, P. Markos, C. M. Soukoulis, *Phys. Rev. B.* **65**, 195104 (2002).

- [39] C. Rockstuhl, T. Paul, F. Lederer, T. Pertsch, T. Zentgraf, T. P. Meyrath, H. Giessen, *Phys. Rev. B* **77**, 035126 (2008).
- [40] N. Liu, L. Fu, S. Kaiser, H. Schweizer, H. Giessen, *Adv. Mater.* **20**, 358 (2008).
- [41] E. Shamonina, L. Solymar, *J. Phys. D: Appl. Phys.* **37**, 362 (2004).
- [42] O. Sydoruk, O. Zhuromskyy, E. Shamonina, L. Solymar, *Appl. Phys. Lett.* **87**, 072501 (2005).
- [43] M. Beruete, F. Falcone, M. J. Freire, R. Marques, J. D. Baena, *Appl. Phys. Lett.* **88**, 083503 (2006).
- [44] F. Falcone, T. Lopetegi, M. A. G. Laso, J. D. Baena, J. Bonache, M. Beruete, R. Marques, F. Martin, M. Sorolla, *Phys. Rev. Lett.* **93**, 197401 (2004).
- [45] T. Zentgraf, T. P. Meyrath, A. Seidel, S. Kaiser, H. Giessen, *Phys. Rev. B* **76**, 033407 (2007).
- [46] H. Liu, D. A. Genov, D. M. Wu, Y. M. Liu, J. M. Steele, C. Sun, S. N. Zhu, X. Zhang, *Phys. Rev. Lett.* **97**, 243902 (2006).
- [47] S. Zhang, W. J. Fan, K. J. Malloy, S. R. J. Brueck, N. C. Panoiu, R. M. Osgood, *J. Opt. Soc. Am. B*, **23**, 434 (2006).
- [48] D. Schurig, J. J. Mock, D. R. Smith, *Appl. Phys. Lett.* **88**, 041109 (2006).
- [49] J.B. Pendry, *Science* **306**, 1353 (2004).
- [50] M. Decker, M. Klein, M. Wegener, S. Linden, *Opt. Lett.* **32**, 856 (2007).
- [51] S. Linden, C. Enkrich, G. Dolling, M. W. Klein, J. Zhou, T. Koschny, C. M. Soukoulis, S. Burger, F. Schmidt, M. Wegener, *IEEE J. Sel. Top. Quantum Electron.* **12**, 1097 (2006).
- [52] W. J. Padilla, D. R. Smith, D. N. Basov, *J. Opt. Soc. Am. B* **23**, 404 (2006).
- [53] C. M. Soukoulis, S. Linden, M. Wegener, *Science* **315**, 47 (2007).
- [54] V. M. Shalaev, *Nature Photon.* **1**, 41 (2007).
- [55] S. Blundell, in *Magnetism in condensed matter*, Oxford University Press, 2004.
- [56] S. Zhang, W. J. Fan, N. C. Panoiu, K. J. Malloy, R. M. Osgood, S. R. J. Brueck, *Phys. Rev. Lett.* **95**, 137404 (2005).
- [57] N. Liu, H. Giessen, *Opt. Express* **16**, 21233 (2008).
- [58] M. J. T. Robinson, in *Organic Stereochemistry*, Oxford, Oxford Univ. Press, 2000.

- [59] P. Nordlander, C. Oubre, E. Prodan, K. Li, M. I. Stockman, *Nano Lett.* **4**, 899 (2004).
- [60] F. Hao, *et al.* *Chem. Rev. Lett.* **458**, 262 (2008).
- [61] A. V. Rogacheva, V. A. Fedotov, A. S. Schwanecke, N. I. Zheludev, *Phys. Rev. Lett.* **97**, 177401 (2006).
- [62] N. Liu, H. Liu, S. Zhu, H. Giessen, *Nature Photon.* **3**, 157 (2009).
- [63] Y. P. Svirko, N. I. Zheludev, in *Polarization of Light in Nonlinear Optics*, Chichester, Wiley, 1998.
- [64] T. Scharf, in *Polarized Light in Liquid Crystals and Polymers*, Wiley, 2007.
- [65] S. E. Harris, *Phys. Today* **50**, No. 7, 36 (1997).
- [66] M. Fleischhauer, A. Imamoglu, J. P. Marangos, *Rev. Mod. Phys.* **77**, 633 (2005).
- [67] L. V. Hau, S. E. Harris, Z. Dutton, C. H. Behroozi, *Nature* **397**, 594 (1999).
- [68] G. Shvets, J. S. Wurtele, *Phys. Rev. Lett.* **89**, 115003 (2002).
- [69] C. Liu, Z. Dutton, C. H. Behroozi, L. V. Hau, *Nature* **409**, 490 (2001).
- [70] S. Zhang, D. A. Genov, Y. Wang, M. Liu, X. Zhang, *Phys. Rev. Lett.* **101**, 047401 (2008).
- [71] P. B. Johnson, R. W. Christy, *Phys. Rev. B.* **6**, 4370 (1972).
- [72] C. Ropers, *et al.* *Phys. Rev. Lett.* **94**, 113901 (2005).
- [73] N. Liu, L. Langguth, T. Weiss, J. Kästel, M. Fleischhauer, T. Pfau, and H. Giessen submitted to *Nature Mater.* (2009).
- [74] P. Tassin, L. Zhang, T. Koschny, E. N. Economou, C. M. Soukoulis, *Phys. Rev. Lett.* **102**, 053901 (2009).
- [75] P. Tassin, L. Zhang, T. Koschny, E. N. Economou, C. M. Soukoulis, *Opt. Express* **17**, 5595 (2009).

Acknowledgements

I would like to thank all the people who helped me and who have also contributed to this thesis. Many thanks go to:

- Prof. Harald Giessen for giving me the opportunity to work in the exciting field of 3D optical metamaterials, for his mentorship, and for many stimulating discussions.
- Prof. Martin Dressel for kindly agreeing to co-referee this thesis.
- Prof. Tilman Pfau, Dr. Stefan Linden, Dr. Hui Liu, Dr. Jürgen Kästel, Dr. Michael Fleischhauer for stimulating discussions.
- Dr. Liwei Fu, Hongcang Guo, and Thomas Zentgraf, and Prof. Heinz Schweizer for many discussions and comments. Stefan Kaiser from the 1st Physics Institute for helping with FTIR measurements.
- Mawuli Ametowobla and Frau Renate Zapf-Gottwick from Institute of Physical Electronics and Dr. Michael Hirscher and Frau Ulrike Eigenthaler for helping with SEM measurements.
- Frau Hedi Graebeldinger, Frau Monika Ubl, Herr Emmerich Frank, Herr Erich Kohler, and Sven Hein for technical support.
- Dr. Christine von Rekowski, Dr. Wolf Woelfel, Frau Gabi Feurle, and Frau Christa Nagel for their support in administrative arrangement.
- All my colleagues in the 4th Physics Institute for warm working atmosphere and their kind helps.
- Last, but not least, I would like to thank my parents and all of my friends. A special thank goes to my husband Zhaolu Diao for his everlasting encouragement, support, and standing by me all the time.

Resume

04/04/1979 Born in Shenyang, Liaoning, China

09/1985-08/1991 Primary school in Nanshierlu, Liaoning, China

09/1991-08/1992 Middle school in No. 159, Liaoning, China

09/1992-08/1994 Middle school in No. 103, Liaoning, China

09/1994-08/1997 High school in No. 31, Liaoning, China

09/1997-08/2001 Bachelor in Science, Physics Department.
Jilin University, Jilin, China

09/2001-08/2003 Master student, Physics Department
Peking University, Peking, China

09/2003-08/2005 Master in Science, Physics Department
The Hongkong University of Science & Technology,
Hongkong, China

10/2005-07/2009 Ph. D student, 4th Physics Institute,
University of Stuttgart, Germany

